The multivalency of the glucocorticoid receptor ligand-binding domain explains its manifold physiological activities

Alba Jiménez-Panizo,[1,2] Andrea Alegre-Martí,[1,2] Gregory Fettweis,[3] Montserrat Abella,[1,2] Rosa Antón,[4] Theophilus Tettey,[3] R. Louis Schiltz,[3] Thomas A Johnson,[3] Israel Nuñez-Barrios,[5] Joan Font-Díaz,[2,6] Carme Caelles,[2,7] Annabel F. Valledor,[2,6] Paloma Pérez,[8] Ana M. Rojas,[5] Juan Fernández-Recio,[9] Diego M. Presman,[10] Gordon L. Hager,[3] Pablo Fuentes-Prior,[4,*] and Eva Estébanez-Perpiñá[1,2,*]

[1]Structural Biology of Nuclear Receptors, Department of Biochemistry and Molecular Biomedicine, Faculty of Biology, University of Barcelona (UB), 08028 Barcelona, Spain.

[2]Institute of Biomedicine of the University of Barcelona (IBUB), University of Barcelona (UB), 08028 Barcelona, Spain.

[3]Receptor Biology and Gene Expression, National Cancer Institute, National Institutes of Health, Bethesda, Maryland 20892-5055, USA.

[4]Molecular Bases of Disease, Biomedical Research Institute Sant Pau (IIB Sant Pau), 08041 Barcelona, Spain.

[5]Computational Biology and Bioinformatics. Andalusian Center for Developmental Biology (CABD-CSIC). Campus Universitario Pablo de Olavide, 41013 Sevilla, Spain.

[6]Department of Cell Biology, Physiology and Immunology, Faculty of Biology, University of Barcelona, 08028 Barcelona, Spain.

[7]Department of Biochemistry and Physiology, Faculty of Pharmacy and Food Sciences, University of Barcelona, Barcelona 08028, Spain.

[8]Instituto de Biomedicina de Valencia (IBV)-CSIC, 46010, Valencia, Spain.

[9]Instituto de Ciencias de la Vid y del Vino (ICVV), CSIC - Universidad de La Rioja - Gobierno de La Rioja, 26007 Logroño, Spain.

[10]IFIBYNE, UBA-CONICET, Universidad de Buenos Aires, Facultad de Ciencias Exactas y Naturales, Buenos Aires, C1428EGA, Argentina.

*__Corresponding authors:__ These authors jointly supervised this work.

Correspondence and requests for materials should be addressed to:

Eva Estébanez-Perpiñá. E-mail: evaestebanez@ub.edu

Pablo Fuentes-Prior. E-mail: pfuentes@santpau.cat

Keywords: glucocorticoid receptor / ligand-binding domain / homodimerization / quaternary structure / X-ray crystallography / fluorescence microscopy

Accession numbers: The atomic coordinates and structure factors reported here have been deposited in the Protein Data Bank (PDB) with the accession codes xxxx (C2), wwww ($P3_1$), yyyy ($P6_1$), zzzz ($I4_122$) and vvvv ($I4_132$).

Abbreviations

AF	Activation function
AR	Androgen receptor
ASA	Accessible surface area
ASU	Asymmetric unit
BF-3	Binding function-3
BSA	Buried surface area
CHAPS	3-[(3-cholamidopropyl) dimethylammonio]-1-propanesulfonate
DBD	DNA binding domain
DEX	Dexamethasone
EDC	1-ethyl-3-(3-dimethylaminopropyl)carbodiimide
EM	Electron microscopy
ER	Estrogen receptor
FL	Full-length
GC	Glucocorticoid
GR	Glucocorticoid receptor
GRE	Glucocorticoid response elements
LBD	Ligand-binding domain
LBP	Ligand-binding pocket
MS	Mass spectrometry
MR	Mineralocorticoid receptor
N&B	Number and brightness
NIP	Normalized interface propensity
NTD	N-terminal domain
ODA	Optimal docking area
PDB	Protein Data Bank
PR	Progesterone receptor
RMSD	Root-mean-square deviation
SHP	Small heterodimer partner
SPR	Surface plasmon resonance
WT	Wild type

Abstract

The glucocorticoid receptor (GR) is a ubiquitously expressed transcription factor that controls metabolic and homeostatic processes essential for life. Although numerous crystal structures of the GR ligand-binding domain (GR-LBD) have been reported, the functional oligomeric state of the full-length receptor, which is essential for its transcriptional activity, remains disputed. Here we present five new crystal structures of agonist-bound GR-LBD, along with a thorough analysis of previous structural work. Biologically relevant homodimers were identified by studying a battery of GR point mutants including crosslinking assays in solution and quantitative fluorescence microscopy in living cells. Our results highlight the relevance of non-canonical dimerization modes for GR, especially of contacts made by loop L1-3 residues such as Tyr545. Our work unveils likely pathophysiologically relevant quaternary assemblies of the nuclear receptor with important implications for glucocorticoid action and drug design.

Introduction

Nuclear receptors (NRs) are a superfamily of transcription factors that control central physiological processes ranging from reproduction and development to metabolism, homeostasis, and ultradian rhythms (Conway-Campbell *et al*, 2012; Busada & Cidlowski, 2017). Steroid receptors form an important subclass of ligand-activated NRs comprising the glucocorticoid receptor (GR/NR3C1) (Fig. 1A), the androgen receptor (AR/NR3C4), the progesterone receptor (PR/NR3C3), the mineralocorticoid receptor (MR/NR3C2), as well as estrogen receptors α and β (ERα/NR3A1 and ERβ/NR3A2, respectively) (Bledsoe et al, 2002; Evans & Mangelsdorf, 2014; Jiménez-Panizo et al, 2019). These proteins share a common modular architecture of a long and unstructured N-terminal domain (NTD) followed by a 'core' comprised of a highly conserved DNA-binding domain (DBD), a poorly conserved interdomain linker or hinge, and a moderately conserved C-terminal ligand-binding domain (LBD) (Fig. 1A; see Supplementary Fig. 1 for an alignment of LBD sequences from different species) (Housley *et al*, 1990; Ortlund *et al*, 2007; Meijsing *et al*, 2009). GR binds cholesterol-derived compounds termed glucocorticoids (GCs; either natural compounds such as the main stress hormone, cortisol, or synthetic, e.g., dexamethasone (DEX)) in an internal cavity of the LBD. This ligand-binding pocket (LBP) is allosterically coupled to a solvent-exposed surface responsible for the interaction with coregulators, activation function 2 (AF-2) (Pfaff & Fletterick, 2010; Rogatsky *et al*, 2003). A nearby surface area, topologically equivalent to AR binding function-3 (BF-3) interacts with cochaperones (Estebanez-Perpina *et al*, 2007; Jehle *et al*, 2014). Finally, the LBDs of GR and other related receptors (AR, PR, and MR; referred to as the oxosteroid subfamily) feature a unique C-terminal extension after the last LBD helix (H12), termed F-domain (Jiménez-Panizo *et al*, 2019; Fuentes-Prior *et al*, 2019) (Fig.1B).

NR3C1 is constitutively expressed in nearly all vertebrate cells. Upon ligand binding, the receptor is trafficked to the nucleus (Vandevyver *et al*, 2012) where a complex

DNA-protein interplay modulates its quaternary structure and determines highly dynamic binding to specific chromatin sites (Weikum *et al*, 2017a). Thus, GR integrates signals ranging from available ligands to chromatin remodeling complexes (Clark & Belvisi, 2012) to control a unique set of target genes (up to 17% of the human transcriptome (Franco *et al*, 2019)) to regulate inflammatory responses, cellular proliferation, and differentiation in a highly tissue-specific manner (Oh *et al*, 2017; Cain & Cidlowski, 2017; Sevilla *et al*, 2010). GR also antagonizes the activity of other transcription factors such as activator protein 1 (AP-1) and nuclear factor kB (NF-kB) (De Bosscher *et al*, 2020). Even though monomeric GR is believed to play an important DNA-independent role in the modulation of these major players of the inflammatory response (Louw, 2019), more recent work suggests that both direct DNA binding and GR dimers / tetramers are important for this activity (Presman *et al*, 2014, 2016; Paakinaho *et al*, 2019; Garcia *et al*, 2021; Escoter-Torres *et al*, 2020; Weikum *et al*, 2017c). In line with these manifold functions, alterations in the complex GR signaling pathways due to polymorphisms or mutations in *NR3C1* lead to impaired tissue-specific sensitivity to GCs, which may manifest as either GC resistance (Chrousos syndrome (Chrousos *et al*, 1986)) or hypersensitivity (Nicolaides & Charmandari, 2019). GR is therefore an important pharmacological target to treat several inflammatory pathologies. However, prolonged use or high doses of GCs in patients results in drug resistance and adverse effects (Clark & Belvisi, 2012). Knowledge of GR tertiary and quaternary structures is critical to understand its pivotal functions. Structures of the DBD dimer, both free and DNA-bound have been presented (Frank *et al*, 2018; Hudson *et al*, 2013; Luisi *et al*, 1991; Härd *et al*, 1990), and the LBD has been extensively studied in complex with either agonists or antagonists (Hurt *et al,* 2016; Weikum *et al,* 2017a; Liu *et al*, 2019; Schäcke *et al,* 2007; Biggadike *et al*, 2009; Carson *et al,* 2014; Bledsoe *et al,* 2002).

To date, however, neither full-length (FL) GR nor its core has been structurally characterized. Thus, several important issues regarding the structure-function of GR and related oxosteroid receptors remain unresolved: what is the conformation adopted by dimeric receptors and DNA-bound tetramers *in vivo*, and how do LBD moieties associate in these multimers? Are topologically distinct receptor conformations possible, and are they associated with specific biological functions (e.g., activation vs. repression of transcription)? The answers to these questions have not only an obvious basic science interest, but knowledge of the dimeric/tetrameric conformations of oxosteroid receptors and the detailed mechanism(s) of multimerization would contribute to the design of selective, potent GR modulators that minimize the serious side effects of current drugs.

Here we present a comprehensive structure-and-function investigation of GR multimerization using X-ray crystallography, state-of-the-art bioinformatics tools, surface plasmon resonance (SPR) and crosslinking experiments in solution, and quantitative fluorescence microscopy in live cells. We report five new crystal structures of DEX-bound GR-LBD and integrate this information into the wealth of previous structural data to generate a complete catalog of possible homodimeric arrangements. Four distinct interfaces have been observed to participate in 20 topologically different GR-LBD homodimers. We have identified most favored homodimeric arrangements and suggest how they can combine into pathophysiologically relevant oligomeric assemblies in cells.

Results

GR-LBD self-associates in solution. To characterize the ability of GR-LBD to oligomerize in solution, we performed SPR experiments with the ancient variant of the human GR (ancGR2; Fig. 1C). This construct recapitulates the characteristics of wild-type (WT) human GR-LBD and has been repeatedly employed in recent GR structure-function studies because of its higher solubility and stability *in vitro* (Ortlund *et al*, 2007; Weikum *et al*, 2017b). For simplicity, we will refer to all variants of the LBD used for different studies as GR-LBD, unless specific differences are discussed. Briefly, GR-LBD was expressed and purified in the presence of DEX. Agonist-bound GR-LBD was immobilized on CM5 chips using standard amine coupling and increasing concentrations of the same agonist-bound protein (between 0.2 and 25 μM) were run over as analyte.

Although GR-LBD immobilization to the CM5 chip might occlude some protein-protein interaction surfaces, the results of these SPR experiments clearly demonstrate interactions between soluble and immobilized molecules. Several kinetics models were used to interpret the obtained SPR data (Figs. 1D and 1E; representative sensorgrams are shown in Supplementary Fig. 2). GR-LBD self-association behavior could be fitted to a non-covalent, 1:1 Langmuir model with an affinity constant (kD) of 15.3 ± 0.9 μM (Fig. 1D). Interestingly, a significant better fit of the data was achieved using a model of non-covalent multisite interaction, with two independent binding sites (kD1 = 2.2 ± 0.4 μM and kD2 = 27.9 ± 1.9 μM, respectively; Fig. 1E). These results are consistent with GR-LBD tetramer formation, as previously reported with FL-GR in live cells (Presman *et al*, 2016).

Novel crystal structures of agonist-bound GR-LBD highlight its versatility for self-association. Next, we performed crystallization trials with DEX-bound GR-LBD in the presence of the AF-2 targeting peptide Gln12-Lys30 from the small heterodimer partner (SHP/NR0B2), which contains the canonical LXXLL motif. We conducted

solubility screens using all commercially available kits (over 4,800 conditions), which allowed us to identify several new crystallization conditions. Diffraction data from flash-frozen crystals that belong to five different space groups (C2, $P3_1$, $P6_1$, $I4_122$ and $I4_132$, from lower to higher symmetry) were collected using synchrotron radiation. Major features of the inter-monomer contacts observed in these new GR-LBD structures are briefly summarized below (Fig. 2; see Supplementary Table 1 for a summary of diffraction data, refinement statistics, and model quality).

Crystals of the C2 space group contain a single molecule of GR-LBD·DEX complexed with the SHP peptide, which is well defined by electron density occupying the AF-2 cleft. Two different inter-monomer contacts were identified: the larger, symmetric interaction surface is centered on the L1-3 loops of both monomers and is stabilized by aromatic π-stacking interactions between opposite Tyr545/Tyr545' residues (Fig. 2A; residues from the second monomer are primed). Further stability is provided by a network of hydrogen bonds (H-bonds) involving several charged residues from both moieties, most notably Asp549 (L1-3), Arg569 (H3), and Asp626 (β-strand S1). A significantly smaller, asymmetric interface features Glu688 (H9), whose carboxylate engages in strong H-bonds with the main chain N atom and the hydroxyl of Ser556' (L1-3). Additional interactions involve H1 (Leu532) and H9 residues (Lys695, Lys699) from one LBD molecule facing H6 (Glu632') from the neighbor. Residue Pro637' (L5-6) is part of this interface, making strong Van der Waals (VdW) interactions with the aliphatic part of Glu688.

Two additional, related crystal structures were solved in the enantiomorphic trigonal and hexagonal space groups, $P3_1$ and $P6_1$ (Fig. 2B; Supplementary Table 1). In the GR-LBD·DEX homodimer with the larger interface, the cleft between H9 and H10-11 is filled with side chains from neighboring L1-3' and L5-6' loops. In particular, the aromatic side chains of Trp712 and Phe715 dock into a shallow groove formed by residues at the C-terminal end of H5 and the following loop. This arrangement is thus

topologically unrelated to the canonical dimerization mode, in which H10-11 helices from two monomers run parallel to each other, resulting in much higher interaction areas of ~1,000 Å^2. Noteworthy, the side chain of Tyr545' engages also in important contacts at this protein-protein interface, docking on H9 from a neighboring monomer. This larger interface is strengthened by salt bridges between residues Arg690 and Asp549' and by several H-bonds (e.g., between the carbonyl oxygen of Phe774 and the hydroxyl of Ser550'). A second, symmetric homodimer is centered on the aromatic side chains of Tyr638 (L6-7) and Phe735/Tyr738 (C-terminal end of H11) facing each other. However, since positions 638 and 738 are occupied by smaller polar residues in WT GR (Cys and Gln, respectively; Fig. 1C), this arrangement is unlikely to be significant *in vivo*.

Finally, two related, medium-resolution structures of GR-LBD·DEX bound to SHP were obtained in the tetragonal and cubic space groups (I4122 and I4132, respectively; Figs. 2C, D). Also in this case, a symmetric homodimer is observed in which the Tyr545/Tyr545' aromatic rings are stacked, although the overall arrangement of LBD modules differs strongly from the Tyr545-directed dimer found in C2 crystals. Additional H1-H3' contacts result in a more compact conformation, which is stabilized by H-bonds between both main- and side-chain atoms of the two monomers, including a Glu542-Arg569' salt bridge. The largest interaction interface in these crystals features a trimeric arrangement in which loops L1-3'/H3', S2-L6' and L11-12' dock perpendicularly onto H10-11. The large, buried surface area in this trimer appears to compensate the electrostatic repulsion of abutting Asp641 carboxylates from the three monomers around a pseudo (in the tetragonal form) or exact 3-fold axis (in the cubic cell).

A complete catalogue of homodimeric arrangements illustrates the multivalent potential of the GR-LBD. The fact that even minor changes in protein complexes and crystallization conditions result in different GR-LBD arrangements, as demonstrated by

the variety of crystal contacts described above (Figs. 2A-D), prompted us to systematically analyze protein-protein contacts in all crystal structures of the domain previously deposited in the PDB. The results of this analysis are summarized in Figs. 3A, B and Supplementary Tables 2 and 3. GR-LBD residues involved in homodimer formation cluster in four areas on the protein surface, the “front”, “back”, “top” and “base” of the domain (Figs. 3B-D), in the standard view of NRs shown in the center of Fig. 1B.

Next, we analyzed which combinations of these four homodimerization interfaces have been encountered in crystal structures. This analysis revealed 20 topologically distinct homodimers, numbered #1-20 throughout the manuscript (see Supplementary Table 3 for interacting residues in all monomer pairs). These homodimeric arrangements appear to cover the whole GR-LBD self-association landscape. Along with 11 symmetric (isologous) dimeric arrangements (i.e., between the same secondary structure elements / residues, such as in the Tyr545-mediated dimers described above), asymmetric or heterotypic homodimers (i.e., where the contacting GR-LBDs engage in interactions using different elements) are also common (9 arrangements).

We further explored the homodimerization potential of GR-LBD with a state-of-the-art protein-protein docking procedure. A total of 12,000 docking dimers were generated using the coordinates from PDB entry 5UFS. This analysis revealed the existence of at least one docking orientation close to 16 of the 20 representatives “crystal homodimers” (with a root-mean-square deviation (RMSD) ≤ 10 Å). Interestingly, the 2nd best-scoring docking orientation was close (7.3 Å RMSD) to one of the dimers (#20). In two further cases (#8, #10), there were docking orientations within 5 Å from the crystal structures, although with no optimal docking scoring.

For an unbiased estimate of the similarity between different homodimeric conformations we first considered the overlapping of shared contact residues. To this

end, we mapped these sets of residues into a multiple sequence alignment and calculated distances between the resulting vectors using different metrics (see Fig. 4A for the clustering obtained using Jaccard's similarity index). This analysis confirmed e.g., the topological similarity between two front-to-front homodimers: the first described non-canonical conformation (#1, PDB 1M2Z (Bledsoe et al, 2002)) and #2, an arrangement observed in PDB 4P6W (He *et al*, 2014) (Supplementary Tables 2 and 3). On the other hand, front-to-front homodimer pairs #6 and #11, although sharing interface residues, differ strongly in that the two monomers are arranged parallel and antiparallel to each other, respectively. Similarly, homodimer pairs #9 and #10 share the important residue Ile628 at the center of their intermonomer interfaces, but the two modules are quite differently oriented relative to each other.

Alternatively, GR-LBD homodimers were superimposed on a common origin and classified by mapping the centers of coordinates of their interaction surfaces (Supplementary Fig. 3A). Supplementary Fig. 3B shows the orientations of these surfaces, represented by vectors between the common center of coordinates and each interaction surface. A hierarchical clustering analysis based on the Euclidean distance between these vectors grouped all homodimers into six clusters (Supplementary Fig. 3C). From the spherical coordinates of the vectors representing the orientations of the interaction surfaces (sinusoidal equal-area projection in Supplementary Fig. 3E), we found that these clusters can be associated with combinations of the previously defined surfaces: cluster 1 (top-front), cluster 2 (top-back), cluster 3 (base-back), cluster 4 (base-front), cluster 5 (front), and cluster 6 (base). While each cluster may contain surfaces with different binding energy values (Supplementary Fig. 3D), arrangements corresponding to top and back interaction surfaces have in general more favorable binding energy. The distribution of interfaces in the top 1,000 docking models also shows significant clustering around regions with favorable binding energy

(Supplementary Fig. 3F). However, docking solutions also clustered in other regions with less optimal energy, such as front and base surfaces.

Two sectors define the internal circuits linking major interaction sites in the GR-LBD.

To identify residues responsible for the functional specificity of GR we first run multiple correspondence analysis (MCA), which did not replicate the previously reported family classification (Weikum *et al*, 2017b), and only identified three residues that divide the NR superfamily into two clusters. This prompted us to use more sophisticated statistical tools to search for evolutionary conserved units in GR-LBD. To analyze if self-association surfaces may be allosterically coupled to other functional regions, we performed a statistical coupling analysis (SCA), which entirely relies on correlated amino acid variations across the domain without considering its 3D structure (Halabi *et al*, 2009; Lockless & Ranganathan, 1999). Indeed, this analysis identified 40 residues that decompose the GR-LBD sequence into two quasi-independent groups of correlated residues or “sectors” (Fig. 3E).

Sector 1 comprises 17 residues in and around H1 and H10, most notably LBP residues Met601 and Arg611 along with the nearby Phe606, whereas sector 2 features 20 residues mostly from H3 and H5 (e.g., Met604 in the LBP, Lys579, Phe584, Gln597 of AF-2, and Trp577 in an internal path connecting AF-2 to the LBP). Finally, three residues (Gly583 of BF-3, Leu596 at the floor of the AF-2 groove, and the internal Tyr663) belong to both sectors. Interestingly, all these residues are clustered in the upper half of the domain, where both sectors are physically interconnected (Fig. 3E). Sector 1 residues cluster around the N-terminus of the domain and are thus likely candidates to interact with hinge residues and the preceding DBD. Perhaps more relevantly, sector 2 comprising residues profusely innervate the LBP and AF-2 regions while Arg611 from sector 1 is essential to position hormones in the LBP. The three residues that belong to both sectors are strategically located to cross-connect the LBP

with AF-2 and BF-3 pockets. Taken together, our results suggest that both sectors link functionally relevant regions thus coupling e.g., ligand binding to coregulator binding or chaperone docking/release.

***In vitro* crosslinking experiments corroborate non-canonical dimerization of GR-LBD.** The results presented above suggest that many surface-exposed residues of GR-LBD engage in a variety of crystal contacts. To clarify which structural elements/residues might be involved in homodimer formation in solution, we took advantage of the observation that some of the crystal interfaces are stabilized by intermolecular H-bonds between Glu/Asp carboxylates and Lys ammonium groups, or that such bonds could be easily formed upon side-chain rotations, and that these linkages can be "frozen" upon incubation with the zero-length crosslinker, EDC.

To verify whether some of these Asp/Glu-Lys H-bonds are formed in solution, we incubated GR-LBD in the presence of EDC. Indeed, we observed rapid formation of a covalent dimer, as well as a fainter band corresponding to a tetrameric arrangement(s) (Fig. 5A). To identify charged residues responsible for EDC crosslinking, bands corresponding to oligomeric GR-LBD forms were excised from the gels, subjected to enzymatic digestions with either trypsin or chymotrypsin, and analyzed by mass spectrometry (MS) (Supplementary Fig. 3A and Supplementary Tables 4 and 5). Most notably, we found that elements essential for top-to-top (#20) and front-to-front (#1, #2, #6, #9, #10 and #11), non-canonical dimerization are overrepresented among EDC-linked peptides, with the most common contacts involving (1) residues of H1 and L1-3, on the one side, and from H3, on the other, which would correspond to front-to-front interactions, as well as (2) H9 and the L9-10 linker from two monomers, which is compatible with homodimer #20 (Fig. 5B, Supplementary Fig. 3B and Supplementary Table 4). Similar results were obtained with the MS-cleavable, urea-based crosslinker, DSBU (Supplementary Table 6).

Cysteine point mutant Y545C demonstrates non-canonical homodimerization of GR-LBD in solution. Inspection of homodimer interfaces in GR-LBD revealed several symmetric arrangements in which the side chain of a solvent-exposed residue from one monomer is located within VdW distance of the same residue from a crystal neighbor (Figs. 2A and 5C). To verify whether some of these conformations are populated in solution, we have generated several cysteine point mutants of the GR-LBD. All studied mutants were properly folded, as indicated by only minor decreases in melting temperatures in differential scanning fluorimetry (DSF) analysis (not shown), in line with the results of a systematic bioinformatics analysis of mutant stability performed using Fold-X (not shown). Incubation of purified GR-LBD(Y545C) in low-reducing conditions resulted in the rapid formation of covalent dimers (Fig. 5D). By contrast, neither the WT protein nor other Cys mutants tested (e.g., D641C, S744C) dimerized under the same conditions. These findings strongly suggest that the side chains of Tyr545 from two monomers are close enough in solution, at least in a subset of GR-LBD molecules.

To directly proof that residues Cys545/Cys545' are responsible for disulfide bridge-mediated dimerization in solution, bands corresponding to the dimer were excised from the gel, treated with iodoacetamide to block free Cys residues, and subjected to enzymatic digestion with trypsin and GluC. MS analysis of these digests allowed indeed the identification of peaks corresponding to peptide V^{543}LCSGYD^{549} crosslinked to either $V^{543'}$LCSGYD$^{549'}$ or $V^{543'}$LCSGYDSTLPDTSTR$^{558'}$, thus confirming Cys545-mediated covalent bond formation (Supplementary Fig. 3C; see also Supplementary Table 7 for a list of a, b and y ions that allowed unambiguous identification of the crosslinked peptides).

To further assess the contribution of Tyr545 to GR homodimerization in solution, SPR assays essentially equivalent to those described above for WT GR-LBD were performed with its Y545C and Y545A mutants. Indeed, experiments conducted with the Cys mutant revealed significant increases in affinity. The increase was highest when

the mutant was used as both ligand (i.e., chip-immobilized) and analyte, and affects mainly the first binding site, with a 3-fold increase in affinity (kD1 = 0.8 vs. 2.2 μM for the WT-WT association; Supplementary Fig. 2B). By contrast, presence of a less bulky alanine at position 545 led to a slightly less tight association (Supplementary Fig. 2C). We also crystallized and solved the structure of the GR-LBD(Y545A) variant, thus confirming proper folding of the generated point mutants. Noteworthy, Y545A crystallized in the P61 space group, which does not involve symmetric contacts between the side chains of residues at position 545 (Fig. 2B). Altogether, our results confirm that residue Tyr545 plays an important role in GR-LBD homodimerization in solution.

Residues Tyr545 and Asp641 modulate multimerization of full-length GR. Quantitative fluorescence microscopy in living cells (the number and brightness method, N&B) allows to estimate the average oligomeric state of a fluorescent protein from its molecular brightness (ε; Digman et al, 2008). For N&B experiments we routinely use GR^{null} mouse adenocarcinoma cells, which possess a tandem array of DNA binding sites for GR, the MMTV array. Cells are transfected with GFP-labeled mouse GR (GFP-mGR) or variants thereof, and the oligomeric state of fluorescently tagged GR molecules is quantified by comparing to a constitutively monomeric GR variant (N525*). Further, presence of the MMTV array allows us to differentially assess oligomerization of the nuclear receptor in the entire nucleoplasm and in a region highly enriched in specific binding sites.

To prove the relevance for the full-length receptor of key surface-exposed residues identified in GR-LBD homodimer interfaces in vitro, we generated alanine mutants of mice GR at positions topologically equivalent to human residues Tyr545, Pro637, Asp641 and Trp712, all of which are conserved in ancGR2 (Fig. 1C). Further, all residues but Asp641 are strictly conserved from fish to humans, and Asp641 is conservatively replaced by a glutamate in non-mammals (Supplementary Fig. 1). To

study the impact of the Tyr545→Ala exchange in the background of two other variants previously shown to be important for GR homodimerization (Presman *et al*, 2016), we also generated the double mutant (Tyr545Ala, Ile628Ala) (in following termed $GR^{dim/Y545A}$) and the triple mutant (Ala458Thr, Tyr545Ala, Ile628Ala), or $GR^{mon/Y545A}$. Finally, we also generated double mutants in which a GR variant that tetramerizes both in the nucleus and at the array (Pro474Arg, Paakinaho et al, 2019) was combined with either P637A or D641V. (These variants, (Pro474Arg, Pro637Ala) and (Pro474Arg, Asp641Val), are in following termed $GR^{tetra/P637A}$ and $GR^{tetra/D641V}$, respectively. All mutated residues in the DBD or LBD moieties are highlighted in Fig. 6A.

Next, we transiently transfected GFP-mGR and the generated mutants into GR^{null} mouse adenocarcinoma cells and performed N&B experiments as previously described (Presman *et al*, 2017, 2016; Digman *et al*, 2008). All mutants translocate to the nucleus upon hormone stimulation (Fig. 6B), indicating proper folding and unaffected ligand binding. Further, all variants except those carrying the GR^{mon} double mutant (Ala458Thr, Ile628Ala) were visible at the MMTV array, suggesting that DNA binding was not impaired either (Fig. 6B, arrowheads). Severely reduced genome-wide chromatin binding for GR^{mon} has recently been shown (Johnson *et al*, 2021), and only a very small percentage of GR^{mon} cells form visible arrays (Presman *et al*, 2016, 2014). Interestingly, we did not detect any arrays in experiments with $GR^{mon/Y545A}$ (Fig. 6B), suggesting an even more drastic phenotype for this triple mutant.

While W712A oligomerizes as the WT receptor both in the nucleoplasm and at the array (Figs. 6C, D), Tyr545Ala substitution appears to slightly decrease dimerization in the nucleoplasm ($\varepsilon = 1.83$). By contrast, Pro637Ala produces a slight increase in oligomerization ($\varepsilon = 2.46$), even though neither difference achieves statistical significance. Since FL GR dimerizes at least through both DBD and LBD moieties (Fig. 6A), we tested the effect of the Tyr545Ala mutation in the GR^{dim} background, which has impaired DBD-DBD contacts yet mostly dimerizes in the nucleoplasm (Fig. 6C,

Presman *et al*, 2014). Indeed, the $GR^{dim/Y545A}$ double mutant shows significant tendency to remain monomeric in the nucleus (ε= 1.16), like the previously characterized GR^{mon} (Fig. 6C, Presman *et al,* 2014). Taken together, these results confirm the important role of Tyr545 in the dimerization of GR in live cells.

On the other hand, the Asp641Val mutation, linked to Chrousos syndrome (Hurley *et al*, 1991) and the Pro637Ala substitution promoted higher-order oligomerization at the array (Fig. 6D), possibly hexamers or a mixture of tetra- and octamers. These findings prompted us to analyze the impact of these two variants when combined with a DBD mutation that enforces GR tetramerization, Pro474Arg. Unexpectedly, instead of synergizing both mutants reversed GR^{tetra} oligomerization in the nucleus (Fig. 6C). By contrast, the GR^{tetra} mutation abrogated the ability of P637A and D641V variants to form higher-order oligomers at the array level (Fig. 6D). These observations highlight a complex relationship between the different structural domains of the NR.

Discussion

Although many structures of GR-LBD have been reported in a wide variety of crystal forms (Supplementary Table 2), the physiologically relevant conformation(s) of GR and other oxosteroid NRs remain disputed. The new structures presented here highlight the ability of different GR-LBD surfaces to engage in homophilic contacts, resulting in different quaternary arrangements depending on the bound agonists/antagonists, cofactors, and other biochemical parameters. For instance, a monoclinic structure of ancGR2-LBD bound to another synthetic GC, triamcinolone acetonide, and complexed to a shorter SHP peptide had been previously reported (PDB 5UFS; Weikum et al, 2017b). Interestingly, 5UFS features a Tyr545-centered parallel dimer almost identical to the topologically equivalent arrangement in our current C2 crystals (Fig. 2A and Fig. 5C). In the case of the hexagonal crystals, similar structures of ancGR2-LBD bound to either DEX or a different GC (mometasone furoate) and complexed to a TIF-2 peptide

had been previously reported (PDB entries 3GN8 and 4E2J, respectively). Although there are only relatively small differences in the cell constants compared to the current $P6_1$ structure (a and b axes are ~5% longer in our crystals, while the c axis is ~4% shorter), this results in a markedly different small intermonomer interface, which is asymmetric in 3GN8/4E2J.

These and other observations prompted us to dissect the oligomerization capability of GR-LBD. Careful inspection of intermonomer contacts in all available 3D structures allowed us to identify 20 topologically different homodimeric architectures (Fig. 4 and Supplementary Table 3). These experimental GR conformations could be grouped into six different clusters considering relationships between interacting residues (Fig. 4A), which correspond to three partially overlapping though topologically distinct front-to-front homodimers (#1, #2, #6, #9, #10 and #11), along with base-to-base (#12), top-to-top (#20), and back-to-back (#15, #16 and #17) arrangements. A similar pattern emerges when these homodimers are represented in spherical coordinates (Supplementary Fig. 4E) or using an unbiased graph analysis (Supplementary Fig. 4C).

Next, we analyzed the behavior of WT GR-LBD and several point mutants generated according to structural and functional evidence in solution, coupled with quantitative fluorescence microscopy of FL GR and several mutants in cells. The results of these investigations, under careful consideration of geometric and energetic parameters, as well as conservation of major interface residues, allow us to postulate the more likely quaternary arrangements of GR-LBD modules associated with its different pathophysiological roles.

GR does not dimerize in an AR-like conformation

It has long been accepted that the “canonical”, H10-mediated homodimeric conformation adopted by ERα-LBD (Supplementary Fig. 5B) is not possible in

oxosteroid receptors, due to both non-conservative replacements of essential interface residues and partial occlusion of the dimerization interface by the F-domain3–5,13,50. Several observations suggested that the non-canonical dimerization mode we have recently reported for AR (Supplementary Fig. 5A), centered on H5 and neighboring elements instead (Nadal *et al*, 2017; Jiménez-Panizo *et al*, 2019; Fuentes-Prior *et al*, 2019) could be adopted by other members of the subfamily. For instance, aromatic residues involved in maintaining the rigid, dimerization-competent structure of H5 such as Trp610 and Tyr613 (in human GR) are highly conserved in all oxosteroid receptors.

However, in contrast to expectations none of the 20 GR-LBD homodimers can be considered as topologically equivalent to the one observed in the crystal structure of AR-LBD, illustrating a more complex multimerization behavior than previously anticipated. Replacement of AR interface residues such as Thr656 by positively charged Lys/Arg residues and of the following Asn657 by bulkier Gln/His residues in all other members of the subfamily might preclude formation of AR-like homodimers in GR / MR / PR. This highlights the difficulty to extrapolate the quaternary structure of a given NR to other, even closely related family members, and the need for experimental evidence to identify physiologically relevant conformations (Fuentes-Prior *et al*, 2019). A related arrangement had been previously observed in some structures of agonist- or antagonist-bound GR-LBD (Bledsoe *et al,* 2002), but its biological relevance has been repeatedly questioned (Kauppi *et al*, 2003), and several unrelated multimeric assemblies could be postulated (discussed in detail below).

Possible quaternary arrangements of the GR-LBD and their functional relevance *in vivo.*

The largest homodimeric interfaces correspond to antagonistic conformations of GR. The symmetric back-to-back (#15) and base-to-base homodimers (#12) have much larger interface areas (~1470 and 1200 Å^2, respectively) and much lower energies (-

98.0 / -83.0 kcal/mol) than all other GR-LBD conformations (750 $Å^2$ and -50.0 kcal/mol for the next best configuration; Supplementary Fig. 4D). Interestingly, these dimers are only observed in GR-LBD bound to the antagonist, mifepristone/RU-486 (PDB entries 1NHZ and 5UC3, respectively, Kauppi *et al*, 2003), and share several important features. First, the bound antagonist enforces displacement of the C-terminal H12, which partially disrupts the LBP. More importantly, in both cases the AF-2 pocket of one monomer is partially covered by either H12 (#15) or H3 (#12) from a neighboring molecule, thus interfering with coregulator binding (Fig. 7A, B). Further, essentially the same arrangements are found in the crystal structure of the dominant negative GRβ, which is known to bind only antagonists53.

Interestingly, RU-486–bound GR-LBD forms a covalent homodimer through disulfide bridge Cys736/Cys736' (in conformation #15; Kauppi *et al,* 2003). The fact that we have not observed this covalent dimer of WT GR-LBD in the presence of dexamethasone suggests that this quaternary arrangement is exclusive of the antagonist-bound receptor. Further, tetrameric arrangements in 1NHZ/5UC3 and in a third structure of mifepristone-bound GR (3H52; Schoch *et al*, 2010) are not compatible with the results of our XL experiments with EDC (Fig. 5A and Supplementary Fig. 2B), or engage the Trp712 side chain, which has no effect on GR homodimerization (Fig. 6C, D), or involve important partial unfolding events that result in swapping of N- and/or C-terminal residues between two monomers (up to L1-3 or from H12 on, respectively). Of note, similar rearrangements have not been observed in the crystal structures of core NRs bound to agonists and their DNA response elements (Chandra *et al*, 2017; Fuentes-Prior *et al*, 2019). Altogether, these findings strongly suggest that the most stable, back-to-back (#15) and base-to-base conformations (#12) of GR-LBD are associated with inactive, (self-repressed receptor states, which are induced or stabilized by antagonist binding to the LBP. Preferential binding of corepressor peptides to these antagonist-bound conformations has been reported (Schoch *et al*,

2010; Min *et al*, 2018), but the significance of these findings in the context of full-length cofactors is not clear. Noteworthy, inactive RXRα adopts a disc-like tetrameric conformation, in which H12 from one molecule protrudes away and docks on the AF-2 pocket of an adjacent monomer (Fig. 7C; Gampe *et al,* 2000). Although the overall arrangement differs from the ones adopted by GR-LBD, the fact that this important surface pocket is occluded in both cases points to a general feature of self-repressed or inactive conformations in NRs. Interestingly, also in the inactive RXR tetramer two monomers are covalently linked through a disulfide bond, suggesting yet unexplored connections between redox state and NR biology.

Formation of non-physiological multimers appears to underlie the deleterious effect of Chrousos syndrome mutants

Unexpectedly, in our N&B experiments we observed that a GR mutant previously linked to Chrousos syndrome, p.Asp641Val49, preferentially formed higher-order oligomers when bound to DNA (Fig. 6D). This non-conservative mutation has a particularly strong stabilizing impact of 3.4 kcal/mol for each dimer pair on the GR-LBD trimer observed in our tetragonal and cubic crystals (#14; see Fig. 2D and Supplementary Table 3). The positive effect of the mutation results from the relief of strong electrostatic repulsion between the three abutting Asp641 residues, coupled with favorable VdW contacts made by the aliphatic Val641 side chains with each other and with Cys638 from a neighboring molecule. Notably, conformation #4 is fully compatible with this trimer and generates a closed hexamer by additional interactions between the N-terminal end of H10 and H12'' at a third interface (Fig. 7E). This conformation would occlude the AF-2 pockets of the "external" monomers and is thus incompatible with coregulator binding.

Interestingly, several additional residues associated with Chrousos disease are located at or close to one of the three monomer-monomer interfaces, and their mutations might promote local conformations that also stabilize this hexamer. For

instance, replacement of Thr556 by an aliphatic isoleucine would stabilize this arrangement through contacts with e.g., residues Met560 and Pro637 from its "own" monomer and/or His645'/Asn731' from a neighboring molecule. Similar considerations apply to mutations such as Arg714Gln, Phe737Leu, Ile747Met and Leu773Pro as well as to the variant of the central interface Pro637Ala, which also forms higher-order oligomers at the array (Fig. 6D). Thus, we conclude that not only p.Asp641Val but also other GR variants associated with Chrousos disease stabilize multimeric forms that are incompatible with active GR tetramers on DNA. This is, to the best of our knowledge, the first time in which non-productive multimers of a NR are postulated as the molecular basis of a human disease.

A three-fold reduced affinity of the Val641 mutant for DEX was previously proposed as the underlying molecular defect in the D641V variant (Hurley *et al*, 1991). However, since Asp641 is exposed on the surface of the protein and is located 8 Å away from the closest DEX atom, it is unlikely to play any relevant role in hormone recognition. Accordingly, nuclear translocation of FL GR(D641V) in live cells was comparable to WT GR, suggesting no major ligand affinity issues. Residue Asp641 was not predicted as part of a sector, which seems to exclude also indirect (allosteric) effects transmitted to the LBP.

The N-terminal end of H10 and surrounding residues are important for chaperone-binding to GR but are unlikely to play a major role in receptor multimerization

Because of their ability to engage in important protein-protein interactions, the bulky, aromatic Tyr/Trp residues are quite common at both homo- and heterodimeric interfaces57. GR-LBD features several exposed Tyr/Trp residues, two of which, Tyr545 and Trp712, are repeatedly found at monomer-monomer interfaces (Fig. 2 and Supplementary Table 3) and are strictly conserved from fish to humans (Supplementary Fig. 1). To explore the possible role of these residues in GR multimerization *in vivo*, we generated the Y545A and W712A mutants of FL GR and

studied their behavior using quantitative fluorescence microscopy. Against expectations, elimination of the bulky indole ring at position 712 had no effect on the oligomerization properties of GR, and the W712A variant behaved as WT both in the nucleoplasm and DNA-bound (Fig. 6C, D). These findings strongly suggest that Trp712 is not important for GR multimerization *in vivo*. This would exclude, among others, the symmetric homodimer in which the Trp712 indole rings of two monomers occupy a shallow pocket between H9 and the F domain from a neighboring molecule (homodimer #20), and which had been proposed as the most likely conformation of the GR-LBD homodimer (Bianchetti *et al*, 2018).

Nevertheless, the fact that Trp712 participates in six topologically different homodimeric arrangements suggests an enhanced propensity for protein-protein interactions. Indeed, the recently reported cryo-EM structure of GR-LBD bound to the "client-maturation complex" Hsp90-p23 has revealed that Trp712 occupies the central position in a major binding epitope for the p23 co-chaperone (Noddings *et al,* 2020). However, none of the six GR-LBD homodimers that engage Trp712 appear to mimic the p23-GR heterocomplex, and there are no FXXMMXXM sequences in GR-LBD that would correspond to the GR-interacting helix in p23.

Non-canonical GR homodimers centered on Tyr545 are critical for GR homodimerization

In contrast with the normal multimerization behavior of the W712A variant, alanine replacement of Tyr545 reduced receptor dimerization in the nucleoplasm. Moreover, when combined with an exchange that disrupts DBD-DBD contacts (Ala458Thr, GR^{dim}), it resulted in a mostly monomeric form (Fig. 6C). Further, an important fraction of GR-LBD Y545C molecules rapidly and spontaneously forms covalent homodimers *in vitro* mediated by the Cys545-Cys545' disulfide bond (Fig. 5C, D). Finally, alanine replacement of Try545 led to a reduced monomer-monomer affinity in SPR

experiments (Supplementary Fig. 2E). Altogether these observations strongly suggest that the Tyr545 phenol ring plays a critically important role in GR homodimerization.

Two of the five topologically different homodimeric arrangements that involve the Tyr545 side chain (#7 and #8) are asymmetric and include the Trp712 indole ring; they are thus unlikely to be relevant *in vivo*. On the other hand, formation of the Cys545-Cys545' disulfide bridge in the Y545C variant is compatible with two topologically different, roughly parallel and antiparallel symmetric homodimers (#6 and #11; Figs. 7F, G, respectively). Incomplete dimerization of GR-LBD(Y545C) suggests that other dimeric states are also populated in solution. Indeed, in a third, also antiparallel GR-LBD homodimer the Tyr545 side chains are located at the borders of the protein-protein interface (#9, Fig. 7H). Interestingly, this arrangement is centered on opposing residues Ile628/Ile628', which are important for receptor dimerization (Presman *et al*, 2014, 2016). Finally, a second Ile628-centered, parallel conformation is found in crystals of ancGR1 (homodimer #10; Fig. 7I; Carroll *et al*, 2011). Thus, both parallel and antiparallel arrangements of LBD modules with different involvement of the Tyr545 and Ile628 "valences" are compatible with current experimental evidence and are equally possible in principle, as the associated buried surface areas and energies are similar (between 530 and 740 $Å^2$ and between -8 and -26 kcal/mol). Some of these quaternary arrangements in solution could be verified in our XL-MS experiments, e.g., Glu542-Lys576' salt bridges detected with EDC are compatible with conformation #11, and DSBU linkage between residues Tyr545 and Tyr638 is only possible in homodimer #9 (Fig. 5A and Supplementary Table 6).

Our live-cell imaging studies have revealed that dimeric GR might be an intermediate state towards transcriptionally active tetramers bound to target DNA sequences (Presman *et al*, 2016; Paakinaho *et al*, 2019; Johnson *et al*, 2021), also in line with the current SPR results. Although more speculative, it is possible to generate tentative models of DNA-bound GR tetramers that satisfy the constraints derived from

current structure-function information. First, we reasoned that since tetramers but not higher order multimers are detected on chromatin, none of the known intermonomer "anchors", Tyr545 and Ile628, could be available for protein-protein interactions in active tetramers. In other words, all GR-LBD "valences" should be satisfied in *bona fide* GR tetramers. Since the Ile628 side chain is exposed in both conformations with opposing Tyr545 rings (#6 and #11), different combinations with homodimers #9 and #10 were tested first. Indeed, different trimeric and tetrameric arrangements could be envisioned, eventually upon replacing the "true" crystal monomer by a close docking solution to avoid intermonomer clashes (Supplementary Figs. 5E-J). These hypothetical multimeric arrangements reconcile the role of residues Tyr545 and Ile628 for receptor multimerization. The additional interactions predicted in these multimeric arrangements, in addition to DBD-DBD interactions (Presman *et al*, 2016) and condensation provided by the NTD (Frank *et al*, 2018; Stortz *et al*, 2020) would overcome the energy loss due to Tyr545→Ala or Ile628→Ala exchanges, explaining why variants Y545A and I628A are still tetrameric on chromatin (Fig. 6D). However, the triple mutant (A458T, Y545A, I628A) did not bind the array, indicating that simultaneous elimination of the Tyr545 and Ile628 valences would generate a well-folded, but fully inactive variant.

In summary, we have explored the multivalency of GR-LBD and have associated experimentally observed homodimers to specific pathophysiologically relevant states of this NR. Homodimers with significantly larger interface surfaces are uniquely linked to antagonist-bound conformations and are likely to be found only in inactive / self-repressed states of the GR. Further, we provide evidence indicating that a mutant associated with GC resistance, p.Asp641Val, might form homo-hexamers on chromatin, and we present a 3D model of these hexamers. Finally, we have identified a previously unappreciated role of the Tyr545 phenolic ring for receptor homodimerization. Current structure-function information suggests that four different

GR-LBD homodimers have roughly equal probabilities to be formed in vivo, which would in turn generate different tetrameric arrangements on chromatin. We are tempted to speculate that these individual conformations of tetrameric GR are associated with specific transcription programs. An inspection of predicted GR-LBD tetramers suggests mechanisms to select these different conformations. For instance, a peptide corresponding to the third LXXLL motif of SRC2/TIF2 would severely clash with a neighboring monomer in some arrangements. Thus, it is possible that different coregulators, or even different LXXLL motifs within a given coactivator select or induce specific NR quaternary arrangements. TNFα-induced modulation of the GR interactome, in particular weakened interactions with p300, and its implications for GR transcriptional output (Dendoncker *et al*, 2019) are in line with this suggestion. Future investigations should verify the validity of this hypothesis and establish whether specific GR conformations are associated with unique expression patterns. The ability to promote or stabilize these specific multimeric states might be an essential step towards the development of novel GCs with reduced side effects.

References

Bianchetti L, Wassmer B, Defosset A, Smertina A, Tiberti ML, Stote RH & Dejaegere A (2018) Alternative dimerization interfaces in the glucocorticoid receptor-α ligand binding domain. *Biochimica et Biophysica Acta - General Subjects* 1862: 1810–1825

Biggadike K, Bledsoe RK, Coe DM, Cooper TWJ, House D, Iannone MA, Macdonald SJF, Madauss KP, McLay IM, Shipley TJ, *et al* (2009) Design and x-ray crystal structures of high-potency nonsteroidal glucocorticoid agonists exploiting a novel binding site on the receptor. *Proceedings of the National Academy of Sciences of the United States of America* 106: 18114–18119

Bledsoe RK, Montana VG, Stanley TB, Delves CJ, Apolito CJ, McKee DD, Consler TG, Parks DJ, Stewart EL, Willson TM, *et al* (2002) Crystal structure of the glucocorticoid receptor ligand binding domain reveals a novel mode of receptor dimerization and coactivator recognition. *Cell* 110: 93–105

Bogan AA & Thorn KS (1998) Anatomy of hot spots in protein interfaces. *Journal of Molecular Biology* 280: 1–9

De Bosscher K, Desmet SJ, Clarisse D, Estébanez-Perpiña E & Brunsveld L (2020) Nuclear receptor crosstalk — defining the mechanisms for therapeutic innovation. *Nature Reviews Endocrinology* 16: 363–377 doi:10.1038/s41574-020-0349-5

Busada JT & Cidlowski JA (2017) Mechanisms of Glucocorticoid Action During Development. In *Current Topics in Developmental Biology* pp 147–170. Academic Press Inc.

Cain DW & Cidlowski JA (2017) Immune regulation by glucocorticoids. *Nature Reviews Immunology* 17: 233–247 doi:10.1038/nri.2017.1

Canutescu AA, Shelenkov AA & Dunbrack RL (2003) A graph-theory algorithm for rapid protein side-chain prediction. *Protein Science* 12: 2001–2014

Carroll SM, Ortlund EA & Thornton JW (2011) Mechanisms for the Evolution of a Derived Function in the Ancestral Glucocorticoid Receptor. *PLoS Genetics* 7: e1002117

Carson MW, Luz JG, Suen C, Montrose C, Zink R, Ruan X, Cheng C, Cole H, Adrian MD, Kohlman DT, *et al* (2014) Glucocorticoid receptor modulators informed by crystallography lead to a new rationale for receptor selectivity, function, and implications for structure-based design. *Journal of Medicinal Chemistry* 57: 849–860

Chandra V, Wu D, Li S, Potluri N, Kim Y & Rastinejad F (2017) The quaternary architecture of RARβ–RXRα heterodimer facilitates domain–domain signal transmission. *Nature Communications* 8: 868

Chen R, Li L & Weng Z (2003) ZDOCK: An initial-stage protein-docking algorithm. *Proteins: Structure, Function and Genetics* 52: 80–87

Cheng TMK, Blundell TL & Fernandez-Recio J (2007) PyDock: Electrostatics and desolvation for effective scoring of rigid-body protein-protein docking. *Proteins: Structure, Function and Genetics* 68: 503–515

Chrousos GP, Loriaux DL, Tomita M, Brandon DD, Renquist D, Albertson B & Lipsett MB (1986) The new world primates as animal models of

glucocorticoid resistance. *Advances in experimental medicine and biology* 196: 129–144 doi:10.1007/978-1-4684-5101-6_9

Clark AR & Belvisi MG (2012) Maps and legends: The quest for dissociated ligands of the glucocorticoid receptor. *Pharmacology and Therapeutics* 134: 54–67 doi:10.1016/j.pharmthera.2011.12.004

Conway-Campbell BL, Pooley JR, Hager GL & Lightman SL (2012) Molecular dynamics of ultradian glucocorticoid receptor action. *Molecular and Cellular Endocrinology* 348: 383–393 doi:10.1016/j.mce.2011.08.014

Dendoncker K, Timmermans S, Vandewalle J, Eggermont M, Lempiäinen J, Van Hamme E, Dewaele S, Vandevyver S, Ballegeer M, Souffriau J, *et al* (2019) TNF-α inhibits glucocorticoid receptor-induced gene expression by reshaping the GR nuclear cofactor profile. *Proceedings of the National Academy of Sciences of the United States of America* 116: 12942–12951

Digman MA, Dalal R, Horwitz AF & Gratton E (2008) Mapping the number of molecules and brightness in the laser scanning microscope. *Biophysical Journal* 94: 2320–2332

Escoter-Torres L, Greulich F, Quagliarini F, Wierer M & Uhlenhaut NH (2020) Anti-inflammatory functions of the glucocorticoid receptor require DNA binding. *Nucleic Acids Research* 48: 8393–8407

Estebanez-Perpina E, Arnold LA, Nguyen P, Rodrigues ED, Mar E, Bateman R, Pallai P, Shokat KM, Baxter JD, Guy RK, *et al* (2007) A surface on the androgen receptor that allosterically regulates coactivator binding. *Proceedings of the National Academy of Sciences* 104: 16074–16079

Evans RM & Mangelsdorf DJ (2014) Nuclear receptors, RXR, and the big bang. *Cell* 157: 255–266

Fernandez-Recio J, Totrov M, Skorodumov C & Abagyan R (2005) Optimal docking area: A new method for predicting protein-protein interaction sites. *Proteins: Structure, Function and Genetics* 58: 134–143

Franco LM, Gadkari M, Howe KN, Sun J, Kardava L, Kumar P, Kumari S, Hu Z, Fraser IDC, Moir S, *et al* (2019) Immune regulation by glucocorticoids can be linked to cell type–dependent transcriptional responses. *Journal of Experimental Medicine* 216: 384–406

Frank F, Okafor CD & Ortlund EA (2018) The first crystal structure of a DNA-free nuclear receptor DNA binding domain sheds light on DNA-driven allostery in the glucocorticoid receptor. *Scientific Reports* 8

Fuentes-Prior P, Rojas A, Hagler AT & Estébanez-Perpiñá E (2019) Diversity of Quaternary Structures Regulates Nuclear Receptor Activities. *Trends in Biochemical Sciences* 44: 2–6 doi:10.1016/j.tibs.2018.09.005

Gabb HA, Jackson RM & Sternberg MJE (1997) Modelling protein docking using shape complementarity, electrostatics and biochemical information. *Journal of Molecular Biology* 272: 106–120

Gallastegui N, Mackinnon JAG, Fletterick RJ & Estébanez-Perpiñá E (2015) Advances in our structural understanding of orphan nuclear receptors. *Trends in Biochemical Sciences* 40: 25–35

Gampe RT, Montana VG, Lambert MH, Wisely GB, Milburn M V & Xu HE (2000) Structural basis for autorepression of retinoid X receptor by tetramer formation and the AF-2 helix. *Genes & development* 14: 2229–41

Garcia DA, Johnson TA, Presman DM, Fettweis G, Wagh K, Rinaldi L, Stavreva DA, Paakinaho V, Jensen RAM, Mandrup S, *et al* (2021) An intrinsically disordered region-mediated confinement state contributes to the dynamics and function of transcription factors. *Molecular Cell* 81: 1484-1498.e6

Grosdidier S & Fernández-Recio J (2008) Identification of hot-spot residues in protein-protein interactions by computational docking. *BMC Bioinformatics* 9

Halabi N, Rivoire O, Leibler S & Ranganathan R (2009) Protein Sectors: Evolutionary Units of Three-Dimensional Structure. *Cell* 138: 774–786

Härd T, Kellenbach E, Boelens R, Maler BA, Dahlman K, Freedman LP, Carlstedt-Duke J, Yamamoto KR, Gustafsson JÅ & Kaptein R (1990) Solution structure of the glucocorticoid receptor DNA-binding domain. *Science* 249: 157–160

He Y, Yi W, Suino-Powell K, Zhou XE, Tolbert WD, Tang X, Yang J, Yang H, Shi J, Hou L, *et al* (2014) Structures and mechanism for the design of highly potent glucocorticoids. *Cell Research* 24: 713–726

Housley PR, Sanchez ER, Danielsen M, Ringold GM & Pratt WB (1990) Evidence that the conserved region in the steroid binding domain of the glucocorticoid receptor is required for both optimal binding of hsp90 and protection from proteolytic cleavage. A two-site model for hsp90 binding to the steroid binding domain. *The Journal of biological chemistry* 265: 12778–81

Hudson WH, Youn C & Ortlund EA (2013) The structural basis of direct glucocorticoid-mediated transrepression. *Nature Structural and Molecular Biology* 20: 53–58

Hurley DM, Accili D, Stratakis CA, Karl M, Vamvakopoulos N, Rorer E, Constantine K, Taylor SI & Chrousos GP (1991) Point mutation causing a single amino acid substitution in the hormone binding domain of the glucocorticoid receptor in familial glucocorticoid resistance. *Journal of Clinical Investigation* 87: 680–686

Hurt DE, Suzuki S, Mayama T, Charmandari E & Kino T (2016) Structural analysis on the pathologic mutant glucocorticoid receptor ligand-binding domains. *Molecular Endocrinology* 30: 173–188

Jehle K, Cato L, Neeb A, Muhle-Goll C, Jung N, Smith EW, Buzon V, Carbó LR, Estebanez-Perpiña E, Schmitz K, *et al* (2014) Coregulator control of androgen receptor action by a novel nuclear receptor-binding motif. *Journal of Biological Chemistry* 289: 8839–8851

Jiménez-Panizo A, Pérez P, Rojas AM, Fuentes-Prior P & Estébanez-Perpiñá E (2019) Non-canonical dimerization of the androgen receptor and other nuclear receptors: Implications for human disease. *Endocrine-Related Cancer* 26: R479–R497 doi:10.1530/ERC-19-0132

Johnson TA, Paakinaho V, Kim S, Hager GL & Presman DM (2021) Genome-wide binding potential and regulatory activity of the glucocorticoid receptor's monomeric and dimeric forms. *Nature Communications* 12

Kauppi B, Jakob C, Färnegårdh M, Yang J, Ahola H, Alarcon M, Calles K, Engström O, Harlan J, Muchmore S, *et al* (2003) The three-dimensional structures of antagonistic and agonistic forms of the glucocorticoid receptor

ligand-binding domain: RU-486 induces a transconformation that leads to active antagonism. *Journal of Biological Chemistry* 278: 22748–22754

Liu X, Wang Y & Ortlund EA (2019) First high-resolution crystal structures of the glucocorticoid receptor ligand-binding domain–peroxisome proliferator-activated γ coactivator 1-α complex with endogenous and synthetic glucocorticoids. *Molecular Pharmacology* 96: 408–417

Lockless SW & Ranganathan R (1999) Evolutionarily conserved pathways of energetic connectivity in protein families. *Science* 286: 295–299

Louw A (2019) GR dimerization and the impact of gr dimerization on gr protein stability and half-life. *Frontiers in Immunology* 10 doi:10.3389/fimmu.2019.01693

Luisi BF, Xu WX, Otwinowski Z, Freedman LP, Yamamoto KR & Sigler PB (1991) Crystallographic analysis of the interaction of the glucocorticoid receptor with DNA. *Nature* 352: 497–505

McNally JC, Müller WG, Walker D, Wolford R & Hager GL (2000) The glucocorticoid receptor: Rapid exchange with regulatory sites in living cells. *Science* 287: 1262–1265

Meijsing SH, Pufall MA, So AY, Bates DL, Chen L & Yamamoto KR (2009) DNA binding site sequence directs glucocorticoid receptor structure and activity. *Science (New York, NY)* 324: 407–10

Mikuni S, Tamura M & Kinjo M (2007) Analysis of intranuclear binding process of glucocorticoid receptor using fluorescence correlation spectroscopy. *FEBS Letters* 581: 389–393

Min J, Perera L, Krahn JM, Jewell CM, Moon AF, Cidlowski JA & Pedersen LC (2018) Probing Dominant Negative Behavior of Glucocorticoid Receptor β through a Hybrid Structural and Biochemical Approach. *Molecular and Cellular Biology* 38: e00453-17

Nadal M, Prekovic S, Gallastegui N, Helsen C, Abella M, Zielinska K, Gay M, Vilaseca M, Taulès M, Houtsmuller AB, *et al* (2017) Structure of the homodimeric androgen receptor ligand-binding domain. *Nature Communications* 8

Nicolaides NC & Charmandari E (2019) Glucocorticoid Resistance. *Experientia supplementum (2012)* 111: 85–102 doi:10.1007/978-3-030-25905-1_6

Noddings CM, Wang RYR & Agard DA (2020) GR chaperone cycle mechanism revealed by cryo-EM: Reactivation of GR by the GR:Hsp90:p23 client-maturation complex. *bioRxiv*: 2020.09.12.294975 doi:10.1101/2020.09.12.294975

Oh KS, Patel H, Gottschalk RA, Lee WS, Baek S, Fraser IDC, Hager GL & Sung MH (2017) Anti-Inflammatory Chromatinscape Suggests Alternative Mechanisms of Glucocorticoid Receptor Action. *Immunity* 47: 298-309.e5

Ortlund EA, Bridgham JT, Redinbo MR & Thornton JW (2007) Crystal structure of an ancient protein: evolution by conformational epistasis. *Science (New York, NY)* 317: 1544–8

Paakinaho V, Johnson TA, Presman DM & Hager GL (2019) Glucocorticoid receptor quaternary structure drives chromatin occupancy and transcriptional outcome. *Genome Research* 29: 1223–1234

Pazos F & Bang J-W (2008) Computational Prediction of Functionally Important Regions in Proteins. *Current Bioinformatics* 1: 15–23

Pfaff SJ & Fletterick RJ (2010) Hormone binding and co-regulator binding to the glucocorticoid receptor are allosterically coupled. *Journal of Biological Chemistry* 285: 15256–15267

Presman DM, Ball DA, Paakinaho V, Grimm JB, Lavis LD, Karpova TS & Hager GL (2017) Quantifying transcription factor binding dynamics at the single-molecule level in live cells. *Methods* 123: 76–88

Presman DM, Ganguly S, Schiltz RL, Johnson TA, Karpova TS & Hager GL (2016) DNA binding triggers tetramerization of the glucocorticoid receptor in live cells. *Proceedings of the National Academy of Sciences* 113: 8236–8241

Presman DM, Ogara MF, Stortz M, Alvarez LD, Pooley JR, Schiltz RL, Grøntved L, Johnson TA, Mittelstadt PR, Ashwell JD, *et al* (2014) Live Cell Imaging Unveils Multiple Domain Requirements for In Vivo Dimerization of the Glucocorticoid Receptor. *PLoS Biology* 12

Rivoire O, Reynolds KA & Ranganathan R (2016) Evolution-Based Functional Decomposition of Proteins. *PLoS Computational Biology* 12

Rogatsky I, Wang JC, Derynck MK, Nonaka DF, Khodabakhsh DB, Haqq CM, Darimont BD, Garabedian MJ & Yamamoto KR (2003) Target-specific utilization of transcriptional regulatory surfaces by the glucocorticoid receptor. *Proceedings of the National Academy of Sciences of the United States of America* 100: 13845–13850

Rojas AM, Fuentes G, Rausell A & Valencia A (2012) The Ras protein superfamily: Evolutionary tree and role of conserved amino acids. *Journal of Cell Biology* 196: 189–201 doi:10.1083/jcb.201103008

Schäcke H, Berger M, Rehwinkel H & Asadullah K (2007) Selective glucocorticoid receptor agonists (SEGRAs): Novel ligands with an improved therapeutic index. *Molecular and Cellular Endocrinology* 275: 109–117

Schoch GA, D'Arcy B, Stihle M, Burger D, Bär D, Benz J, Thoma R & Ruf A (2010) Molecular Switch in the Glucocorticoid Receptor: Active and Passive Antagonist Conformations. *Journal of Molecular Biology* 395: 568–577

Sevilla LM, Bayo P, Latorre V, Sanchis A & Pérez P (2010) Glucocorticoid receptor regulates overlapping and differential gene subsets in developing and adult skin. *Molecular Endocrinology* 24: 2166–2178

Stortz M, Pecci A, Presman DM & Levi V (2020) Unraveling the molecular interactions involved in phase separation of glucocorticoid receptor. *BMC Biology* 18: 1–20

Vandevyver S, Dejager L & Libert C (2012) On the Trail of the Glucocorticoid Receptor: Into the Nucleus and Back. *Traffic* 13: 364–374 doi:10.1111/j.1600-0854.2011.01288.x

Weikum ER, Knuesel MT, Ortlund EA & Yamamoto KR (2017a) Glucocorticoid receptor control of transcription: Precision and plasticity via allostery. *Nature Reviews Molecular Cell Biology* 18: 159–174 doi:10.1038/nrm.2016.152

Weikum ER, Okafor CD, D'Agostino EH, Colucci JK & Ortlund EA (2017b) Structural analysis of the glucocorticoid receptor ligand-binding domain in complex with triamcinolone acetonide and a fragment of the atypical coregulator, small heterodimer partner. *Molecular Pharmacology* 92: 12–21

Weikum ER, de Vera IMS, Nwachukwu JC, Hudson WH, Nettles KW, Kojetin DJ & Ortlund EA (2017c) Tethering not required: The glucocorticoid receptor binds directly to activator protein-1 recognition motifs to repress inflammatory genes. *Nucleic Acids Research* 45: 8596–8608

Acknowledgments

We thank Prof. Erick Ortlund (Emory University) for providing the plasmid for ancGR2-LBD expression, Arnold T. Hagler for his comments on the manuscript, and Ildefonso Cases (CABD) for his help and input with some code. We thank ALBA-Cells synchrotron Xaloc team for beamline support.

Funding

E.E.-P. greatly thanks the kind generosity and support of G.E. Carretero Fund for Science, and grants BFU-Retos2017-86906-R, SAF2017-71878-REDT and SAF2015-71878-REDT (Red Nacional de Receptores Nucleares (NurCaMeIn)) (MINECO, Gobierno de España). P.F.-P. thanks grant RTI2018-101500-B-I00 (MINECO). A.R.M. thanks RTI2018-096735-B-100 and JF-R acknowledges PID2019-110167RB-I00 (MINECO). AVF and CC acknowledge SAF2017-89510-R (MINECO). N&B experiments were supported by the Intramural Research Program of the NIH, National Cancer Institute, Center for Cancer Research. D.M.P was supported BY CONICET.

Author contributions

P.F.-P. and E.E.-P. conceived and designed the initial project and supervised its overall execution, provided financial support, and share overall responsibility for the presented results and final approval of the article. A.J.P., A.A.M., M.A.M. and R.A. expressed and purified recombinant proteins. M.A.M., A.A.M., and A.J.P. performed crystallization trials. A.A.M, J.F.D. and R.A. performed site-directed mutagenesis and protein analyses. I.N.B., A.R.M., and E.E.-P. performed and interpreted sequence and SCA analyses. J.F.R. and A.J.P. performed and interpreted docking, NIP and ODA calculations. T.T., R.L.S., and T.A.J. generated GR-FL mutants. G.F. and D.M.P. performed and analyzed N&B experiments. A.J.P., P.F.-P., and E.E.-P. performed SPR experiments and interpreted data. A.J.P., R.A., P.F.-P., and E.E.-P. performed MS experiments and interpreted results. A.J.P., P.F.-P., and E.E.-P. performed X-ray

crystallography experiments, interpreted diffraction data and solved and refined 3D structures. T.T., R.L.S., T.A.J., A.V.F., C.C., and P.P. contributed tools. D.M.P., and G.L.H. supervised cell experiments. A.J.P., P.F.-P., and E.E.-P. drafted the article. A.R.M, J.F.R., D.M.P., G.L.H., P.F.-P., and E.E.-P. critically reviewed the manuscript. All authors discussed the results and commented on the manuscript.

Competing interests

The authors have no competing interests.

Data and materials availability

The atomic coordinates and structure factors have been deposited in the Protein Data Bank (PDB; www.rcsb.org) and the accession codes assigned are xxxx (C2), wwww ($P3_1$), yyyy ($P6_1$), zzzz ($I4_122$), and vvvv ($I4_132$). The PDB accessibility has been designed “for immediate release on publication”. The mass spectrometry proteomics data have been deposited to the ProteomeXchange Consortium via the PRIDE partner repository with the dataset identifier PXD028039. Bioinformatics data and code for the clustering, and sector analyses are available at https://github.com/ibn90/GRPROJECT2021. The authors declare that all relevant data are available upon request.

Figure legends

Fig. 1 legend: The ligand-binding domain of GR self-associates in solution.

A, Schematic representation of domain organization in major GR isoforms. GRα and GRβ are identical up to residue 727 (H10/11), but the last 50 (in GRα) and 15 residues (in GRβ, green box) are fully unrelated. Other common isoforms are shown to the right. **B**, Overall structure of the GR-LBD monomer. The domain is shown in standard orientation in the middle of the panel (i.e., with H1 and H3 displayed in the forefront facing the viewer and the AF-2 pocket on the left hand-side of the domain). Four additional orientations are shown to highlight other domain areas. Models are depicted as cartoons with helices (blue), loops (pink) and beta-sheets (purple). The ligand DEX (salmon spheres) and the SHP peptide (yellow cartoon) are also shown. The BF-3 pocket is also labeled. **c**, Sequence alignment of LBDs between wild-type GR, two engineered variants of human GR used in several structure-function investigations (PDB codes 3CLD and 4CSJ), and the resurrected forms, ancGR1 and 2. Strictly conserved residues are white with black shading; other conservatively replaced residues are shaded gray. Residues mutated in the current study are marked with asterisks. **D, E**, SPR analysis of GR-LBD self-association according to (**D**) 1:1 or (**E**) multisite models. The results of experiments conducted in duplicate are shown along with the calculated affinity constants (k_D). The 1:1 fitting had a Chi^2 value of 4.52, whereas the multisite model had a Chi^2 value of 1.25.

Fig. 2 legend: New crystal structures of DEX-bound GR-LBD reveal a variety of quaternary assemblies.

For all structures, the overall crystal packing is shown in the central panels. Monomers are depicted as cartoons, DEX molecules are represented as salmon spheres, and SHP peptides as yellow ribbons. Details of intermonomer interfaces are given in the lateral panels, in which the side chains of interacting residues are shown as sticks with all their non-hydrogen atoms. **A**, Monoclinic (C2) crystals. Note that major contacts are centered on L1-3 with stacked Tyr545 phenol rings from two neighboring molecules. **B**, Trigonal ($P3_1$) and hexagonal ($P6_1$) crystals. The $P6_1$ structure generates from the lower symmetry group by conversion of a local (approximate) into a crystallographic (exact) two-fold axis. Residue Tyr545 engages in heterologous contacts with a neighboring molecule in these crystal forms (see the position of the Trp712' side chain). **C, D**, Common packing of tetragonal ($I4_122$) and cubic ($I4_132$) crystals. Note that the phenol rings of two Tyr545 residues stack as in the C2 crystals, although the two interacting monomers are fully differently oriented relative to each other. Note also that the largest interface in these crystal forms features abutting Asp641 side chains from three monomers, which are organized around a local ($I4_122$) or exact 3-fold axis ($I4_132$; right side panel in **D**).

Fig. 3 legend: **Experimental structures and bioinformatics analyses unveil four major homodimerization surfaces on GR-LBD.**

A, Relative frequencies of residue involvement in GR-LBD homodimer formation. Bar height indicates how often a given residue engages in crystal contacts in all available structures of GR-LBD, normalized to the residue most frequently found in homodimer interfaces, Leu741. Secondary structure elements given below the plot correspond to the crystal structure of human GR-LBD resolved at the highest resolution, 6NWL. **B**, Residues involved in GR-LBD homodimerization cluster in continuous patches on its front (colored purple), base (coral), back (blue) and top (pink) faces. The association of these four faces yields the catalog of GR-LBD dimers represented in Fig. 4. Models are shown in the same orientation and at the same magnification in panels **C**-**E** below. **C**, Predicted protein-protein interaction optimal docking areas (ODA). ODA "hotspots" (residues with favorable docking energy; ODA < -10.0 kcal/mol) are colored red, residues with ODA > 0 kcal/mol are shown in blue, and intermediate values are scaled accordingly. ODA hotspots form continuous surface patches that essentially overlap with the four protein-protein interaction interfaces shown in panel **B**. **D**, Hotspot interface residues predicted from docking experiments. Surface residues are colored according to their normalized interface propensities (NIP). Residues with NIP > 0.4 and < 0 are colored red and blue, respectively; intermediate values are scaled accordingly. **E**, Statistical coupling analysis (SCA) identifies two sectors of clustered, physically connected residues in GR-LBD. The front and back orientations of GR-LBD are depicted, and in both cases the module is represented as a solid surface and as a cartoon, with helices shown as rods and labeled. Residues belonging to sectors I and II are shown with their side chain atoms as spheres, colored cyan and dark blue, respectively. Other important residues are also shown for orientation and labeled. The AF-2-bound SHP peptide is colored yellow, and the DEX ligand is represented as salmon spheres.

Fig. 4 legend: An integrated catalog of GR-LBD homodimers.

The four distinct GR-LBD protein-protein interfaces associate to generate 20 topologically different homodimers. **A**, A dendrogram based on a hyerarchical analysis of protein-protein contacts using Jaccard's index groups the 20 unqiue GR-LBD asemblies into six different clusters. **B**, Relationsships between the different GR-LBD homodimers. For orientation, monomers highlighting the four interacting surfaces are placed at the cardinal points in this panel (top, nord; front, east; base, south; and back, west), colored-coded as in Fig. 3. Monomers in 10 representative homodimers are depicted as cartoons; each monomer is colored according to the face used to associate with its partner. Dimers are placed closest to the generating monomers.

Fig. 5 legend: Several GR-LBD homodimers are populated in solution.

A, SDS-PAGE analysis of GR-LBD samples after incubation with the zero-length crosslinker, EDC. Notice bands with relative molecular masses corresponding to GR-LBD dimers (D) and tetramers (T) in all the lanes except control lane 1 (no EDC added). Lanes 2 and 3, protein incubated at about 0.37 mg/ml; lanes 4 and 5, protein incubated at about 1.5 mg/ml. Samples in lanes 2 and 4 were treated at room temperature; those in lanes 3 and 5 at 30 ºC. **B**, Crosslink map of EDC-treated GR-LBD showing all crosslinked peptides captured. Regions corresponding to the top, front, base, and back surfaces are colored as in Figs. 3 and 4. A secondary structure plot is shown above the map. **C**, Closeup of the major homodimerization interface in C2 crystals (front-to-front homodimer #11), dominated by stacked phenol rings of Tyr545/Tyr545' residues. **D**, Non-reducing SDS-PAGE analysis of purified GR-LBD(Y545C) (lane 3) shows spontaneous dimerization in solution. Note that the WT protein does not form dimers when incubated at the same concentration (lane 2).

Fig. 6 legend: Mutation of LBD-LBD interface residues profoundly affects the multimerization behavior of full-length GR.

A, Schematic 3D model of the full-length protein. The intrinsically disordered NTD mediates liquid-liquid phase separation (LLPS) and is followed by the globular DBD (here, the structure of its DNA-bound dimer is shown), and by the actual LBD. Note that the length and flexibility of the DBD-LBD linker (hinge, H) allows for the formation of various different homodimers. The side chains of all residues mutated to assess the multimerization behavior of GR are shown as spheres. **B**, Subcellular localization of WT GFP-mGR and indicated mutants in 3617-GRKO cells, as assessed by fluorescence microscopy. Variant N525* lacks the entire LBD and remains monomeric (Presman *et al*, 2016). White arrowheads point to the MMTV arrays. Scale bar: 5 μm. Data for WT_GR, GR^{dim}, GR^{mon} and GR^{tetra} were taken from (Presman *et al*, 2016) and are shown for comparison purposes. Residue numbers correspond to the human protein to facilitate comparisons. **C**, GR quaternary structure in the nucleus, as determined in N&B assays. The fold increase in molecular brightness (ε) relative to the N525* monomeric control is shown. **D**, Quaternary structure of DNA-bound GR. The results of N&B assays at the MMTV arrays are represented as in panel C. Note that simultaneous disruption of intermonomer interactions mediated by the DBD (Ala458Thr) and the LBD (Tyr545Ala) in the $GR^{dim/Y545A}$ double mutant results in a variant that is monomeric in the nucleus, while at the array it formed mostly trimers. In panels **C** and **D**, centered lines show the medians and crosses represent sample means (average numbers below each box-plot). Box limits indicate the 25th and 75th percentiles; whiskers extend 1.5-fold the interquartile range from the 25th and 75th percentiles, with outliers represented by dots. Boxes with different superscript letters are significantly different from each other ($p<0.05$; one-way ANOVA followed by Tukey's multiple comparison test).

Fig. 7: Multimeric arrangements of GR-LBD compatible with current structural information.

A-D, Tetrameric arrangements found in the crystal structures of GR-LBD bound to the potent antagonist, RU-486 (PDB codes 1NHZ (**A**) and 5UC3 (**B**), respectively) compared to (**c**) the inactive RXR-LBD tetramer (1G1U). Two-fold axes generating the dimers-of-dimers run roughly perpendicular to the page plane. **D**, Model of GR-LBD tetramer generated by docking dimer #11 onto itself. The model is compatible with the results obtained with the Y545C mutant and EDC-crosslinking assays. **E**, Putative GR-LBD hexamer favored by the Asp641Val mutation. The central trimer corresponds to an arrangement observed in tetragonal and cubic crystal forms (#14; Figs. 2c, d and 4), while the external monomers dock according to conformation #4. Asp641 residues from the central trimer are encircled. **F-G**, Models of human GR-LBD homodimers based on the observed assemblies #10 (**F**), #6 (**G**), #9 (**H**), and #11 (**J**). The critical homodimerization residues, Tyr545 and Ile628, are shown as color-coded spheres in all cases.

Methods

Peptides and proteins. A peptide corresponding to residues Gln18-Lys27 of SHP/NR0B2 (box 1 motif; NH2-Q_{18}GAASRPAILYALLSSSLK$_{27}$-OH) was custom-synthesized at Pepmic. Recombinant ancGR2-LBD (corresponding to residues 529 to 777 of the human receptor) cloned into a pMALCH10T vector was expressed as fusion protein with an N-terminal maltose-binding protein (MBP) and a hexahistidine tag and purified to homogeneity using standard chromatographic procedures (Weikum *et al*, 2017b).

Crystallization and structure determination. Purified, concentrated DEX-bound ancGR2-LBD was combined with a 3-fold molar excess of SHP peptide and incubated for one hour at RT. Drops of the ancGR2-LBD-SHP mixture were equilibrated against 0.1 M Tris-HCl, pH 8.0, 0.2 M sodium chloride, 2.0 M ammonium sulfate ($P3_1$, $I4_122$ and $I4_132$ crystals); 0.1 M PIPES, pH 7.0, 0.1 M ammonium acetate, 2.5 M sodium formate ($P6_1$ crystals); or 85 mM sodium cacodylate trihydrate, pH 6.5, 0.17 M sodium acetate trihydrate, 25.5% (w/v) PEG8000, 15% (v/v) glycerol (C2 crystals) using the sitting drop vapor-diffusion method. Diffraction data were collected at 100 K at the ALBA-CELLS synchrotron and processed using MOSFLM (http://www.mrc-lmb.cam.ac.uk/harry/mosflm/) and CCP4 (http://www.ccp4.ac.uk/). The crystal structures were solved and refined using MOLREP, REFMAC5 and COOT from the CCP4 package. Crystal packing was analyzed using PISA (http://www.ebi.ac.uk/), model quality was assessed with MolProbity (http://molprobity.biochem.duke.edu/), and figures were prepared with PyMOL (http://www.pymol.org).

Surface plasmon resonance (SPR) analyses. SPR analyses were performed at 25 ºC in a BIAcore T200 instrument (GE Healthcare). Highly purified, DEX-bound recombinant WT ancGR2-LBD and its Y545C and Y545A mutants were diluted in 10 mM sodium acetate, pH 5.0 and directly immobilized on CM5 chips (GE Healthcare) by amine coupling at densities between 300 and 400 resonance units (RU). As a

reference, one of the channels was also amine-activated and blocked in the absence of protein. The running buffer was 50 mM HEPES, pH 7.2, 50 mM Li_2SO4, 5% glycerol, 1 mM dithiothreitol (DTT), 50 µM DEX. Sensorgrams were analyzed with the BIAcore T200 Evaluation software 3.0 and fitted according to the Langmuir 1:1 and multisite models.

Crosslinking experiments. Purified recombinant ancGR2-LBD (33 µM) was incubated with 100-fold molar excess of crosslinkers 1-ethyl-3-(3-dimethylaminopropyl)carbodiimide hydrochloride (EDC, Pierce) or disuccinimidyl dibutyric acid (DSBU) for 1-2 hours at 37 ºC following the manufacturer's instructions. In some experiments the Y545C variant was incubated after affinity purification for 30 min at room temperature without further treatment. Samples of the reaction mixtures were boiled in the presence of Laemmli sample buffer, either reducing (EDC- and DSBU-crosslinked proteins) or non-reducing (in the case of the Y545C variant) and resolved by SDS-PAGE.

Nano-LC-MS/MS mass spectrometry. CBB-stained bands corresponding to monomeric, dimeric and tetrameric GR-LBD after crosslinking with EDC or DSBU were excised from the gels and subjected to in-gel digestion following standard protocols. Briefly, excised bands were reduced (10 mM DTT) in 50 mM bicarbonate buffer, pH 8.0, for 45 min at 56 ºC, alkylated (50 mM iodoacetamide in 50 mM ammonium bicarbonate buffer for 30 min at 25 ºC) and digested with either trypsin alone or followed by GluC treatment, or with chymotrypsin overnight at 37 ºC in 100 mM ammonium acetate buffer, pH 8.0. (Sequencing-grade endoproteases were from Promega). In the case of the Y545C mutant, proteins in the excised bands were directly alkylated without previous DTT treatment to prevent reduction of the Cys545-Cys545' disulfide bridge.

Tryptic peptides were diluted in 1% formic acid and loaded onto a 180 µm x 20 mm C18 Symmetry trap column (Waters) at a flow rate of 15 µl/min using a

nanoAcquity Ultra Performance LCTM chromatographic system (Waters). Peptides were separated using a C18 analytical column (BEH130 C18, 75 mm x 25 cm, 1.7 µm; Waters) with a 120-min run, comprising three consecutive linear gradients: from 1 to 35% B in 100 min, from 35 to 50% B in 10 min and from 50 to 85% B in 10 min (A= 0.1% formic acid in water, B= 0.1% formic acid in CH_3CN). The column outlet was directly connected to an Advion TriVersa NanoMate (Advion) fitted on an LTQ-FT Ultra mass spectrometer (Thermo), which was operated in positive mode using the data-dependent acquisition mode. Survey MS scans were acquired in the FT-ICR cell with the resolution (defined at 400 m/z) set to 100,000. Up to six of the most intense ions per scan were fragmented and detected in the linear ion trap. The ion count target value was 1,000,000 for the survey scan and 50,000 for the MS/MS scan. Target ions already selected for MS/MS were dynamically excluded for 30 s. Spray voltage in the NanoMate source was set to 1.70 kV. Capillary voltage and tube lens on the LTQ-FT were tuned to 40 and 120 V, respectively. The minimum signal required to trigger MS to MS/MS switch was set to 1,000 and activation Q value was set at 0.25. Singly charged precursors were rejected for fragmentation.

Differential scanning fluorometry. Thermofluor experiments were performed in an iQ5 Multicolor Real Time PCR Detection System (BIO-RAD) using 96-well plates (Hard-Shell® High-Profile Semi-Skirted PCR Plate, BIO-RAD) and a 25-µL total volume for each reaction. Melting curves were acquired from eight replicates to determine the average melting temperature (Tm). GR-LBD samples (0.5 mg/mL) were prepared in 20 mM HEPES, pH 8.0, 200 mM NaCl, 10% glycerol, 50 mM imidazole, 1 mM DTT, 50 µM DEX, and centrifuged 5 min at 14,000 rpm immediately before measurements. SYPRO Orange dye (Sigma-Aldrich) was firstly prepared at 80× in the same buffer, starting from a 5,000× commercial dilution. The final concentration of the dye in each well was 5×. The plates were sealed with optical-quality sealing film (Microseal® B Seals, BIO-RAD) and centrifuged at 2,000×g for 30 s. Samples were equilibrated for 60 s and

analyzed using a linear gradient from 16 to 95 ºC with increments of 1 ºC/min, recording the SYPRO orange fluorescence throughout the gradient using the iQ5 Optical System Software 2.0. Values were fitted using the online tool JTSA with the four-parameter logistic equation, and the calculated fluorescence midpoints were compared with an unpaired t-test for equal variances using GraphPad Prism 8.

Subcellular localization and number and brightness (N&B) analysis. pROSA-GFPmGR expresses GFP-tagged mouse GR under the CMV promoter. The plasmid also contains homologous recombination arms for potential integration into the GT(Rosa)26Sor locus (Paakinaho *et al*, 2019). All mutations were generated with the QuikChange II XL Site-Directed Mutagenesis Kit (Stratagene) according to the manufacturer's instructions.

Mammary adenocarcinoma 3617-derived GR^{null} cells (Paakinaho *et al*, 2019) were grown in Dulbecco's modified Eagle's medium (DMEM, Invitrogen) supplemented with 5 µg/ml tetracycline (Sigma-Aldrich), 10% fetal bovine serum (Gemini), sodium pyruvate, non-essential amino acids, and 2 mM L-glutamine maintained in a humidifier at 37 °C and 5% CO_2. This cell line contains a tandem array (~200 copies) of a mouse mammary tumor virus long terminal repeat, Harvey viral ras (MMTV-v-Ha-ras) reporter integrated into chromosome 4, which can be directly visualized in living cells as a localized domain if bound to a fluorescently labelled protein63. Prior to DEX treatment, cells were seeded to 2-well Lab-Tek chamber slides (Thermo Fisher, Waltham, MA, USA) and incubated for at least 18 h in DMEM medium containing 10% charcoal-stripped FBS (Life Technologies) and 2 mM L-glutamine. Cells were transiently transfected with the indicated pROSA-GFPmGR mutants using jetOPTIMUS™ reagent (PolyPlus) according to the manufacturer's instructions.

Images were taken at the CCR, LRBGE Optical Microscopy Core facility in a LSM 780 laser scanning microscope (Carl Zeiss, Inc.) equipped with an environmental chamber. Cells were imaged from 20 min up to a maximum of 2 hours after DEX

addition. We used a 63× oil immersion objective (NA = 1.4). The excitation source was a multi-line Ar laser tuned at 488 nm. Fluorescence was detected with a GaAsP detector in photon-counting mode.

N&B measurements were done as previously described (Presman *et al*, 2016). For each studied cell, a single-plane stack of 150 images (256 x 256 pixels) were taken in the conditions mentioned above, setting the pixel size to 80-nm and the pixel dwell time to 6.3 µs. In all cases, we discarded the first 10 images of the sequence to reduce overall bleaching. The frame time under these conditions is 0.97 s, which guarantees independent sampling of molecules according to previously reported FCS measurements (Mikuni *et al*, 2007). Each stack was further analyzed using the N&B routine of the SIMFCS 2.0 software developed at the Laboratory for Fluorescence Dynamics (UCI). In this routine, the average fluorescence intensity (<I>) and its variance (σ2) at each pixel of an image are determined from the intensity values obtained at the given pixel along the image stack. The apparent brightness (B) is then calculated as the ratio of σ2 to <I> while the apparent number of moving particles (N) corresponds to the ratio of <I> to B (Digman *et al*, 2008). Classification of pixels according to their intensity values allows to easily split nucleus and array for further analysis. Selection of cells for analysis followed these criteria. (1) In the case of stimulated cells, an accumulation of signal at the array must be visible. (2) The average apparent number of molecules (N) in the nuclear compartment must have a range of 3-18 in all cases, (3) no saturation of the detector at any pixel (N < 60), and (4) bleaching cannot exceed 5-10%. In a previous work it has been demonstrated that B is equal to the real brightness ε of the particles plus one (Digman *et al*, 2008). Therefore, ε at every pixel of images can be easily extracted from B measurements. Importantly, this analysis only provides information regarding the moving or fluctuating fluorescent molecules since fixed molecules (relative to our frame time) will give B values equal to 1. The experiments were independently repeated two times for each treatment/condition.

Bioinformatics analysis of the impact of GR point mutations. We estimated the impact of the generated mutations on the overall protein stability with the FoldX empirical force (http://foldxsuite.crg.eu/), which has an estimated error of ~0.7 kcal/mol. Ten iterations were conducted for each mutation, and later averaged. Free energy differences between mutant and WT proteins ($\Delta\Delta G$) < 1 kcal/mol were considered not significant, those between 1 and 2, 2 and 4, and > 4 kcal/mol as slightly, mildly, and strongly destabilizing, respectively.

Sequence analyses. The sequence of human GR-LBD was used as query against the whole NR database, from which we selected ~880 sequences and included the ancestral GR(Weikum *et al*, 2017b). We also downloaded the sequences corresponding to the LBD regions from a representative fraction of proteomes at PFAM rp55 (PF00104_rp55). (Note that the sequences included in the PFAM alignment are truncated, as they lack for instance the non-conserved F-domain). We followed three different approaches to ensure sequence and alignment diversity and thus stability of the analyses. First, we aligned the ~880 sequences to a structure-based profile from entries 5UFS (GR-LBD) and 5JJM (AR-LBD). The resulting alignment, 880_aln, was used to run pySCA in addition to the original SCA5 method. Secondly, we aligned our ~880 sequences to a profile generated from the PF00104_rp55 removing fragments to generate the 840_aln. Finally, we used the PFAM alignment as retrieved from the PFAM database, which contains ~13,000 sequences (PF00104_rp55).

Multiple correspondence analysis (MCA): identifying specificity-determining positions

Positions differentially conserved within protein subfamilies (termed “specificity determining positions”, SDPs) are related to functional specificity (e.g., binding of different cofactors; for a review see Pazos & Bang, 2008). Recent methods based on multiple correspondence analysis (MCA) have allowed identification of their subtle patterns of conservation within large protein families (Rojas *et al*, 2012). We have performed both supervised and unsupervised runs of the S3DET method

(http://csbg.cnb.csic.es/JDet/) on 840_aln using default parameters to maintain a large sequence diversity.

Statistical coupling analysis (SCA)

We have used the SCA5 8/2011 version(Halabi *et al*, 2009) with the three different alignment versions given above, and the updated version pySCA67 with 880_aln. Each alignment produced unique sets of residues termed Sca5_880, Sca5_840, and Sca5_onPFAMrp55, respectively. Next, we labeled residues in the three different sectors that emerged as outputs of the program with letters A, B, and C, following their order of appearance. The stability of the identified sectors was assessed with a statistical test based on hypergeometric calculations of the groups of residues belonging to given sectors between pairs of alignments. P-values were adjusted using false discovery rate (FDR). Next, specific residues from the significant sectors were extracted and selected according to their rank. For instance, if a particular residue appears only in one sector on a low-ranking pair of alignments (e.g., rank 19, with a borderline p-value) this residue will not be selected as part of a sector. On the contrary, if a residue appears in high-ranking pairs, it will be retained. Residues termed as “A” and “B” appeared to be equivalent in different pairs of alignments, so they were assigned to the class sector 2, while residues belonging to the “C” group were stable, and therefore assigned to class sector 1.

Clustering of interaction surfaces in GR-LBD dimers. We grouped the interaction surfaces observed in the 20 GR-LBD homodimers by a hierarchical clustering analysis, using *ad-hoc* R scripts. For each dimer, the interaction surface was defined as the set of solvent-exposed residues in the monomers (i.e., residues with > 25% relative accessible surface area, ASA) that became buried (< 25% relative ASA) in the corresponding dimer. Relative ASA were calculated using ICM (Molsoft LLC). Then, we computed the center of coordinates of the residues forming each interaction interface. To compare two pairs of homodimers, we computed the Euclidean distances between

the centers of their interaction surfaces after superimposition on a common monomer. The 40×40 distance matrix representing the distances between all pairs of interaction surfaces was used to perform hierarchical clustering with Ward's method. Finally, the dendrogram generated from this analysis was sorted in order of increasing distance.

Docking experiments and analysis. Homodimeric models of GR-LBD were built using pyDock docking and scoring method68. First, protein models were prepared by removing all cofactors and heteroatoms, and missing side chains were modeled with SCWRL 3.0 (Canutescu et al, 2003). Then, the Fast Fourier Transform (FFT)-based docking programs FTDock70 (with electrostatics and 0.7-Å grid resolution) and ZDOCK 2.1 (Chen *et al*, 2003) were used to generate 10,000 and 2,000 rigid-body docking poses, respectively. These were merged in a single pool for subsequent pyDock scoring68, based on energy terms previously optimized for rigid-body docking. The pyDock binding energy is basically composed of accessible surface area (ASA)-based desolvation, Coulombic electrostatics and VdW energy terms. Electrostatics and VdW contributions were limited to -1.0/+1.0 and 1.0 kcal/mol for each inter-atomic energy value, respectively, to avoid excessive penalization from possible clashes derived from the rigid-body approach.

Predicted dimer interfaces

Optimal docking areas (ODA) per surface-exposed protein residues were obtained by computing surface patches with optimal desolvation energy based on the selection of low-energy docking regions generated from each surface residue (Fernandez-Recio *et al*, 2005). ODA hot spots (residues with low ODA values, usually less than -10.0 kcal/mol) indicate regions with favorable desolvation energy upon interaction with a partner protein.

From the resulting docking poses, normalized interface propensity (NIP) values were obtained for each residue with the built-in patch module of pyDock, implementing the pyDockNIP algorithm (Grosdidier & Fernández-Recio, 2008). A NIP value of 1

indicates that the corresponding residue is involved in all predicted interfaces of the 100 lowest energy docking solutions, while a value of 0 means that it appears as expected by random chance. Finally, a negative NIP value implies that the residue appears at the low-energy docking interfaces less often than expected by random chance. Usually, residues with NIP ≥ 0.2 are considered as hot-spot residues when using FTDock.

Energetic characterization of GR dimers

The binding energy of the different crystal dimers was computed with the pyDock bindEy module, using the same scoring function as in docking (Cheng *et al*, 2007).

Supplementary figure legends and Tables

Fig. S1 legend. Partial sequence alignment of GR-LBD from selected species.

GR homologs were identified and aligned using PSI-BLAST (https://blast.ncbi.nlm.nih.gov/Blast.cgi?PAGE_TYPE=BlastSearch&PROGRAM=blastp&BLAST_PROGRAMS=psiBlast). To provide a representative view of LBD conservation across vertebrates, sequences of mammalian (human, chimpanzee, squirrel monkey, pig, rat, and mouse), avian (chicken, quail, becard, and pigeon), reptile (turtle), amphibian (frog) and fish GR (tarpon, zebrafish, and dogfish) were included in the alignment. Residues conserved in hGR and other homologs are shaded purple, and conservative replacements are shaded light violet.

Fig. S2 legend. SPR analysis of protein-protein interactions between wild-type GR-LBD and its Tyr545 mutants.

SPR experiments were performed by running increasing concentrations (0.2, 0.4, 0.8, 1.6, 3.12, 6.25, 12.5 and 25 µM) of DEX-bound WT GR-LBD (**A**), GR-LBD Y545C mutant (**C**), or GR-LBD Y545A mutant (**E**) over the same immobilized protein. SPR sensorgrams corresponding to experiments conducted in duplicate are shown in all cases. A schematic representation of the interactions between soluble analyte and chip-immobilized molecules are depicted in panels **B**, **D** and **F**, respectively. Tables below panels **A, C** and **E** summarize major parameters (maximum response (R_{max}), dissociation constant (k_D), and fitting error (Chi^2)) derived from the fitting of self-association sensorgrams according to either 1:1 or multisite models.

Fig. S3 legend. Mass spectrometric verification of cross-links between GR-LBD molecules in solution.

A, Representative MS/MS spectra identifying EDC-crosslinked peptides between Glu688 and Lys699, corresponding to the top-to-top conformation (#20). **B,** Summary of all EDC-crosslinks identified between Lys-Asp and Lys-Glu residue pairs, mapped on the 3D structure of GR-LBD. The central panels show the surface-exposed lysines, while aspartate and glutamate residues are highlighted in the left and right panels, respectively. Note that the uneven distribution of charged residues across the domain surface, in particular of lysines, only allows demonstration of a subset of possible homodimeric conformations populated in solution. **C**, Representative MS/MS spectra identifying crosslinked peptides formed by disulfide bridges between Cys545-Cys545' residues in the Y545C variant of GR-LBD.

Fig. S4 legend. Distribution and clustering of homodimerization interfaces in GR-LBD.

The centers of coordinates of the interaction surfaces in the 20 topologically distinct GR-LBD homodimers are schematically represented as dots (**A**) or as vectors drawn from the center of coordinates of a common monomer to the given interface (**B**). **C**, Dendrogram generated from the hierarchical clustering of all GR-LBD homodimers, based on the Euclidean distances between the centers of coordinates of the interaction surfaces. Each interaction surface is named according to the dimer number (#1-#20) and the chain ID of the monomer. Note that the clustering analysis clearly separates the interaction surfaces in six clusters. **D**, Binding energy of the GR-LBD homodimers, as calculated with pyDock. **E**, A sinusoidal equal-area projection of the interaction surfaces in the 20 GR-LBD dimers, represented as spherical coordinates from the vectors defined in panel B. Clusters obtained as described above are shaded blue. **F**, Representation in spherical coordinates of the interaction surfaces in the top 1,000 docking solutions of monomeric GR-LBD on itself (blue dots, results obtained using coordinates form PDB entry 5UFS). For comparison, the interaction surfaces for the 20 topologically distinct crystal homodimers are shown as red dots.

Fig. S5 legend. **Possible conformations of multimeric GR-LBD.**

A, Three-dimensional structure of dimeric AR-LBD (PDB 5JJM), a non-canonical prototype of NR dimerization. The two monomers are shown as cartoons, colored gray and light cyan, respectively. The interacting helices H5 from both monomers are labeled. **B**, Three-dimensional structure of ERα-LBD dimer (PDB 1ERE), representing the canonical conformation observed in NR homo- and heterodimers. The two monomers are shown as cartoons, colored slate blue and gray, respectively. The interacting helices H10/11 from both monomers are labeled. **C**, GR-LBD trimer generated by docking dimers #6 and #10. **D**, GR-LBD tetramer generated by combining dimers #11 and #14. **E-J**, Putative alternative conformations of tetrameric GR-LBD generated by docking dimer #11 onto itself. The major interface residues Tyr545 and Ile628 are given as spheres in panels **C** - **J**. Note that there are no “free valences” (exposed Tyr545 / Ile628 side chains) in these multimeric arrangements.

Table S1 legend. Summary of X-ray diffraction data, refinement statistics and model quality.

Table S2 legend. Summary of GR-LBD structures reported to date.

PDB entries are ordered from lowest (monoclinic, C2) to highest (cubic, $I4_132$) space group symmetry. Major crystal parameters are given, along with the identity of LBP-bound compounds, peptides occupying the AF2 site, and other co-crystallized small-molecule compounds. ancGR, ancient GR; the sequences of ancGR1 and 2 are given in Fig. 1C. Other engineered variants of human GR (hGR; UniProt entry P04150) are named according to the first deposited structure. The mutations introduced in these variants are: hGR_1M2Z: F602S; hGR_3CLD: F602Y, C638G; hGR_1NHZ: F602S, C638D; hGR_3H52: F602S, C638D, E684A, E688A, W712S; hGR_4CSJ: V571M, F602S, C638D; hGR_5NFT: V571M, F602S, C638D, E684A, W712S; hGR_4P6X: F602A, C622Y, T668V, S674T, V675I, E684A, E688A; and hGR_4P6W: F602A, C622Y, T668V, S674T, V675I, K699A, K703A. PDB entry 5UC3 features a dominant negative hGR variant, (L733K, N734P). The reported structures of mouse GR-LBD contain either the F602S mutation (3MNE), the double mutant (F602S, A605V) in 3MNO, or the triplet (A605V, V702A, E705G) in 3MNP. HetgaGRb refers to the GRb variant from the naked mole-rat, *Heterocephalus glaber*, with residues topologically equivalent to Phe602 and Val728 replaced by Ser and Asn, respectively.

Other abbreviations: 1CA / 1TA, triamcinolone acetonide; 29M, non-steroidal GR antagonist; 8W5, budesonide; 8W8, indazole ether-based GR modulator AZD5423; ACE, acetyl group; B9Q, B9T, and B9W, oral GR modulators; BOG, b-octyl glucopyranoside; CL, chloride ion; CHAPS, 3-[(3-cholamidopropyl)dimethylammonio]-1-propanesulfonate; CV7, desisobuytyryl ciclesonide; DAY, deacylcortivazol; DEX, dexamethasone; DMS, dimethyl sulfoxide; DOC, desoxycorticosterone; E7T, GR agonist; EDO, 1,2-ethylenediol; FMT, formic acid; GOL, glycerol; GSK866, non-steroidal GR agonist; GW6, fluticasone furoate; HCY, cortisol; HEPES, 4-(2-hydroxyethyl)-1-piperazine ethanesulfonic acid; HEX, hexane 1,6-diol; HYC, hydrocortisone; JZN, D-prolinamide 11; JZS, alanine amide derivative; JZR, hexyl b-D-glucopyranoside; LSJ, dibenzoxepane sulfonamide; MOF, mometasone furoate; MPD,

(4*S*)-2-methyl-2,4-pentanediol; NN7, non-steroidal GR modulator, suitable for inhalation; R8C, indazole ether-based non-steroidal GR modulator; RU-468, mifepristone; SCN, thiocyanate ion; TLA, tartaric acid.

Table S3 legend. Heatmap representation of the 20 topologically distinct GR-LBD homodimers. Interface residues in all pairs of GR-LBD monomers identified by PISA are marked (X).

Table S4 legend. Summary of EDC-crosslinked peptides of ancGR2-LBD identified by mass spectrometry.

Table S5 legend. MS/MS verification of EDC-mediated crosslink between residues Glu688 and Lys699

The masses of generated a, b and y ions are indicated.

Table S6 legend. Summary of DSBU-crosslinked peptides of ancGR2-LBD identified by mass spectrometry.

Table S7 legend. MS/MS verification of disulfide bridge formation between Cys545 residues from two GR-LBD(Y545C) monomers.

The masses of generated a, b and y ions are given.

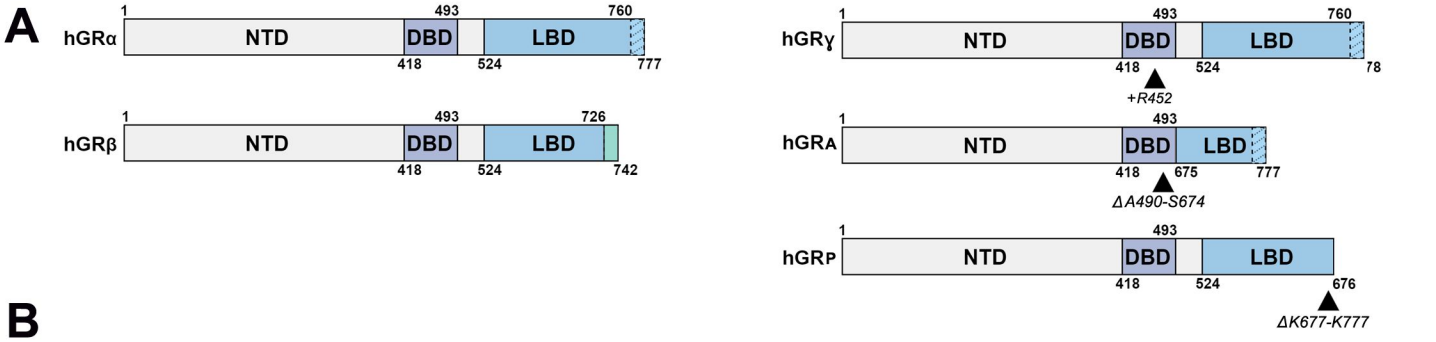
A
hGRα
1
493
760
NTD
DBD
LBD
418
524
777
hGRβ
726
742
hGRγ
78
+R452
hGRA
675
ΔA490-S674
hGRP
676
ΔK677-K777

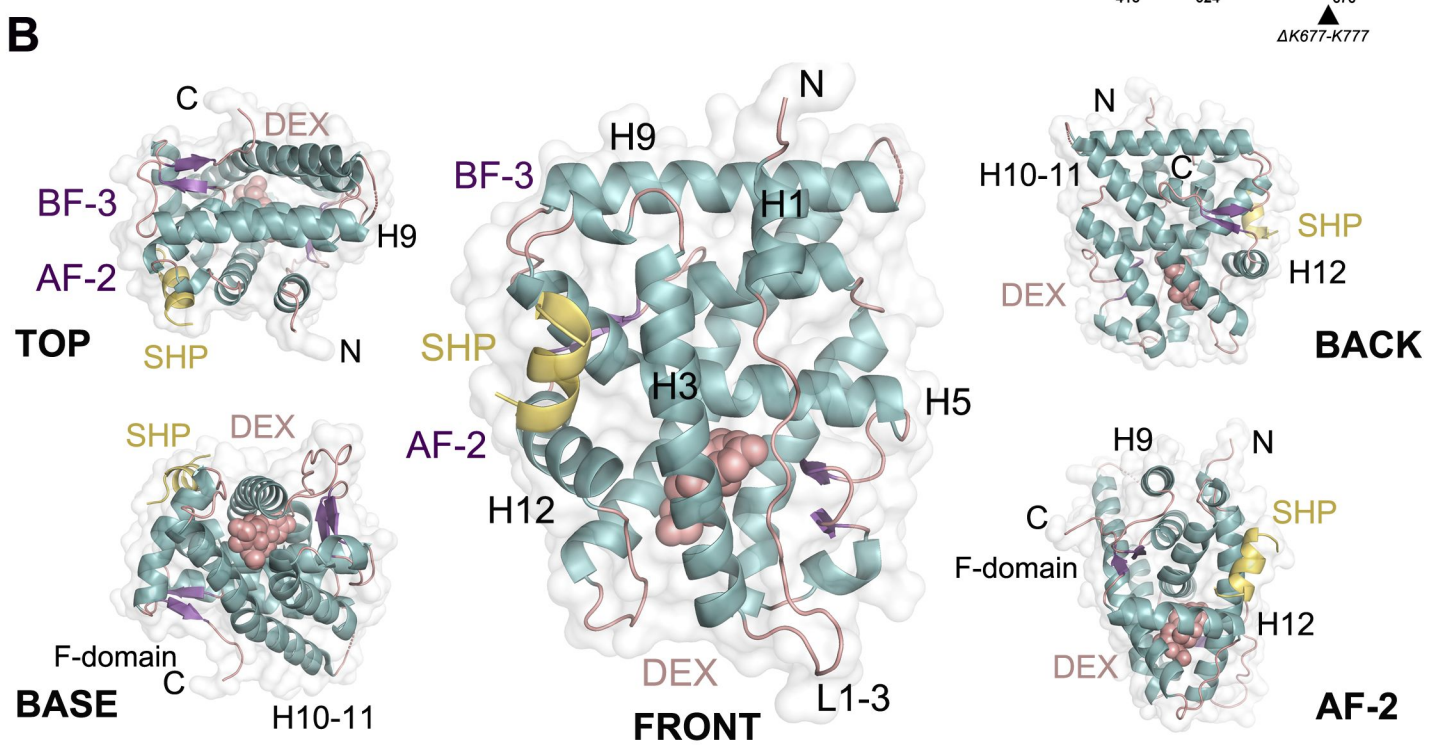
B
C
DEX
BF-3
H9
AF-2
TOP
SHP
N
H9
BF-3
H1
SHP
H3
H5
AF-2
H12
DEX
L1-3
FRONT
N
H10-11
C
SHP
H12
DEX
BACK
SHP
DEX
F-domain
C
BASE
H10-11
H9
N
C
SHP
F-domain
H12
DEX
AF-2

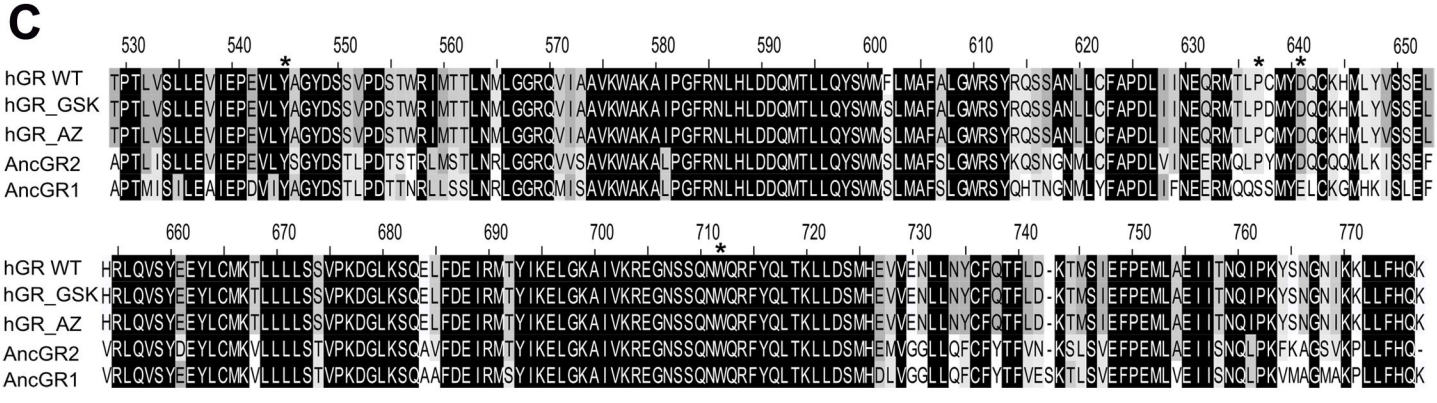
C
530
540
550
560
570
580
590
600
610
620
630
640
650
hGR WT TPTLVSLLEVIEPEVLYAGYDSSVPDSTWRIMTTLNMLGGRQVIAAVKWAKAIPGFRNLHLDDQMTLLQYSWMFLMAFALGWRSYRQSSANLLCFAPDLIINEQRMTLPCMYDQCKHVLYVSSEL
hGR_GSK TPTLVSLLEVIEPEVLYAGYDSSVPDSTWRIMTTLNMLGGRQVIAAVKWAKAIPGFRNLHLDDQMTLLQYSWMSLMAFALGWRSYRQSSANLLCFAPDLIINEQRMTLPDMYDQCKHVLYVSSEL
hGR_AZ TPTLVSLLEVIEPEVLYAGYDSSVPDSTWRIMTTLNMLGGRQVIAAVKWAKAIPGFRNLHLDDQMTLLQYSWMSLMAFALGWRSYRQSSANLLCFAPDLIINEQRMTLPCMYDQCKHVLYVSSEL
AncGR2 APTLISLLEVIEPEVLYSGYDSTLPDTSTRLMSTLNRLGGRQVVSAVKWAKALPGFRNLHLDDQMTLLQYSWMSLMAFSLGWRSYKQSNGNMLCFAPDLVINEERMQLPYMYDQCQQVLKISSEF
AncGR1 APTMISTLEAIEPDVTYAGYDSTLPDTTNRLLSSLNRLGGRQMISAVKWAKALPGFRNLHLDDQMTLLQYSWMSLMAFSLGWRSYQHTNGNMLYFAPDLIFNEERMQQSSMYELCKGMHKISLEF
660
670
680
690
700
710
720
730
740
750
760
770
hGR WT HRLQVSYEEYLCMKTLLLLSSVPKDGLKSQELFDEIRMTYIKELGKAIVKREGNSSQNWQRFYQLTKLLDSMHEVVENLLNYCFQTFLD-KTMSIEFPEMLAEIITNQIPKYSNGNIKKLLFHQK
hGR_GSK HRLQVSYEEYLCMKTLLLLSSVPKDGLKSQELFDEIRMTYIKELGKAIVKREGNSSQNWQRFYQLTKLLDSMHEVVENLLNYCFQTFLD-KTMSIEFPEMLAEIITNQIPKYSNGNIKKLLFHQK
hGR_AZ HRLQVSYEEYLCMKTLLLLSSVPKDGLKSQELFDEIRMTYIKELGKAIVKREGNSSQNWQRFYQLTKLLDSMHEVVENLLNYCFQTFLD-KTMSIEFPEMLAEIITNQIPKYSNGNIKKLLFHQK
AncGR2 VRLQVSYDEYLCMKVLLLLSTVPKDGLKSQAVFDEIRMTYIKELGKAIVKREGNSSQNWQRFYQLTKLLDSMHEMVGGLLQFCFYTFVN-KSLSVEFPEMLAEIISNQLPKFKAGSVKPLLFHQ-
AncGR1 VRLQVSYEEYLCMKVLLLLSTVPKDGLKSQAAFDEIRMSYIKELGKAIVKREGNSSQNWQRFYQLTKLLDSMHDLVGGLLQFCFYTFVESKTLSVEFPEMLVEIISNQLPKVMAGMAKPLLFHQK

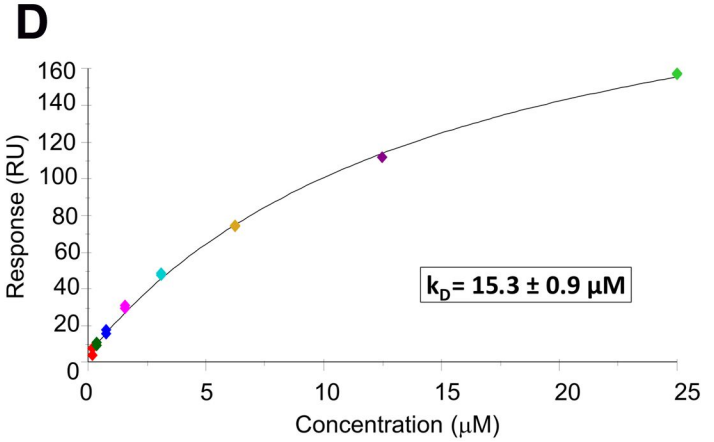
D
Response (RU)
Concentration (μM)
k_D= 15.3 ± 0.9 μM

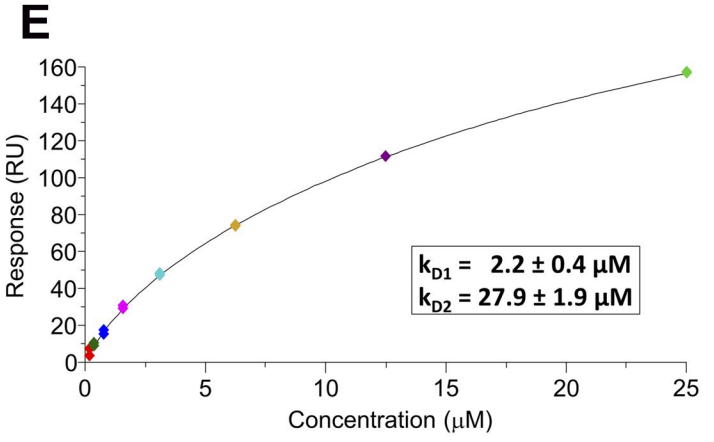
E
Response (RU)
Concentration (μM)
k_{D1} = 2.2 ± 0.4 μM
k_{D2} = 27.9 ± 1.9 μM

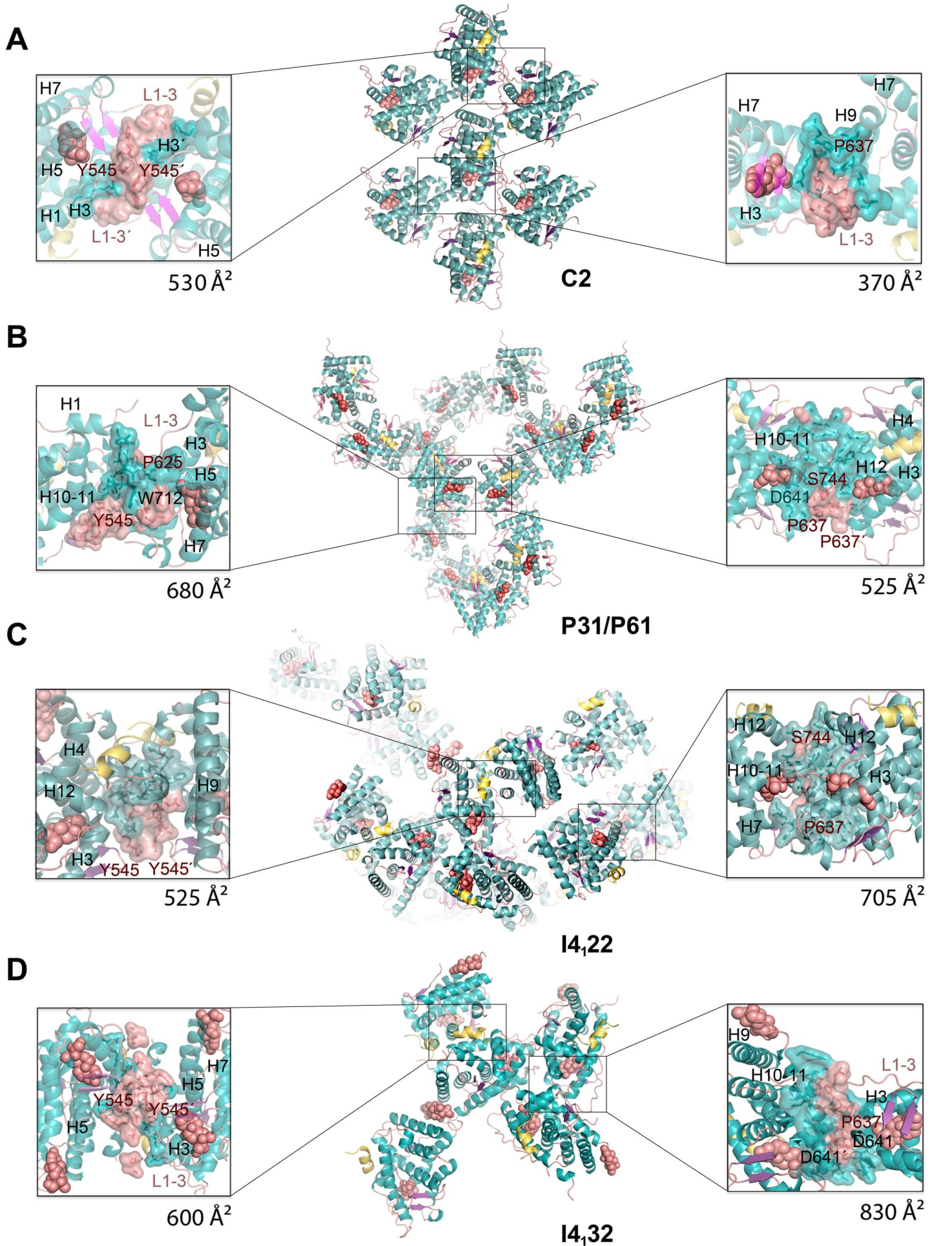
A
H7
L1-3
H3´
H5
Y545
Y545´
H1
H3
L1-3´
H5
530 Å²
C2
H7
H7
H9
P637
H3
L1-3
370 Å²
B
H1
L1-3
H3
P625
H5
H10-11
W712
Y545
H7
680 Å²
P31/P61
H4
H10-11
H12
H3
S744
D641
P637
P637´
525 Å²
C
H4
H12
H9
H3
Y545
Y545´
525 Å²
I4122
H12
S744
H12
H10-11
H3
H7
P637
705 Å²
D
H7
H5
Y545
Y545´
H5
H3
L1-3
600 Å²
I4132
H9
L1-3
H10-11
H3
P637
D641
D641´
830 Å²

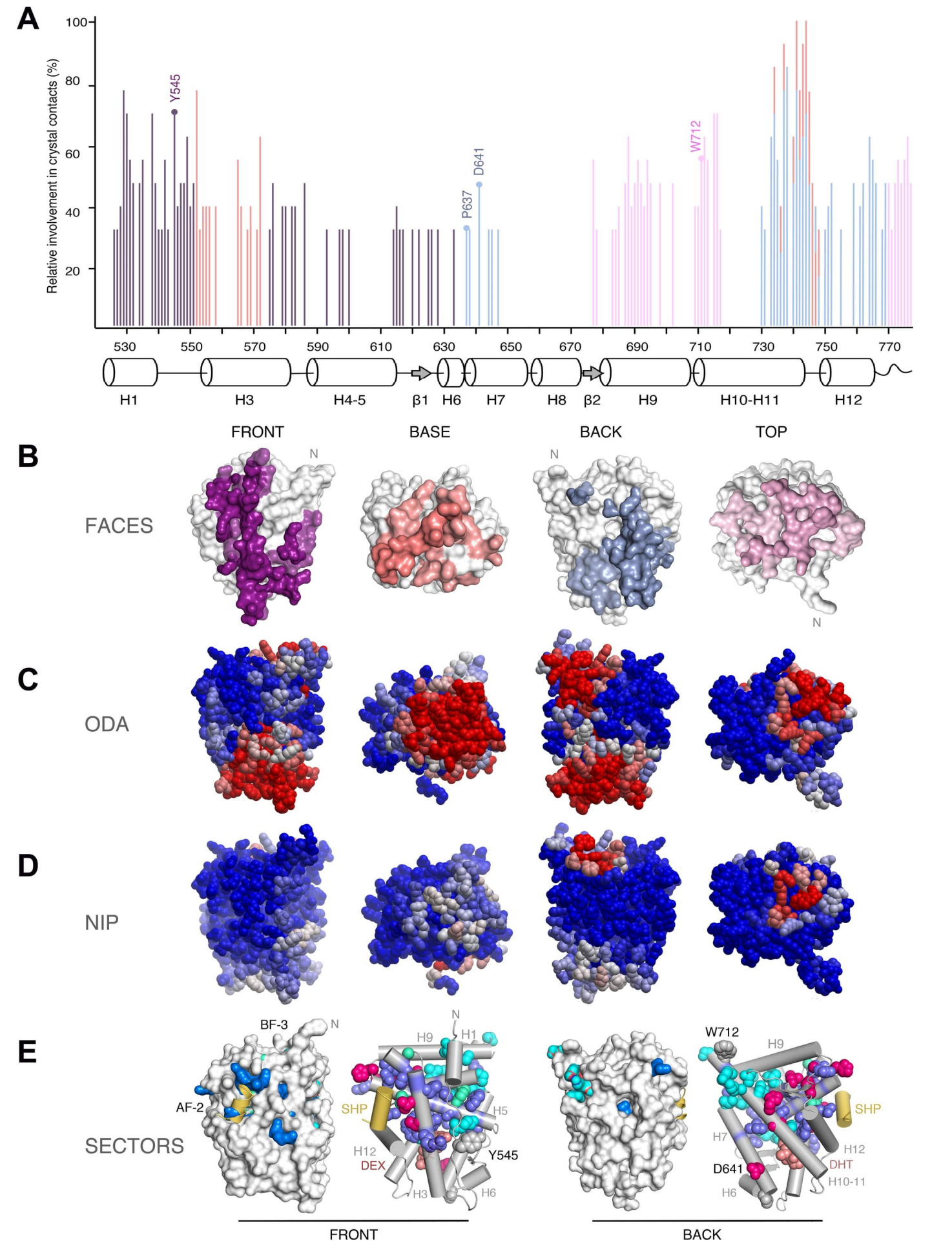
A
Relative involvement in crystal contacts (%)
100
80
60
40
20
Y545
P637
D641
W712
530
550
570
590
610
630
650
670
690
710
730
750
770
H1
H3
H4-5
β1
H6
H7
H8
β2
H9
H10-H11
H12
FRONT
BASE
BACK
TOP
B
FACES
N
N
N
C
ODA
D
NIP
E
SECTORS
BF-3
N
AF-2
N
H9
H1
SHP
H5
H12
DEX
Y545
H3
H6
W712
H9
SHP
H7
H12
D641
DHT
H10-11
H6
FRONT
BACK

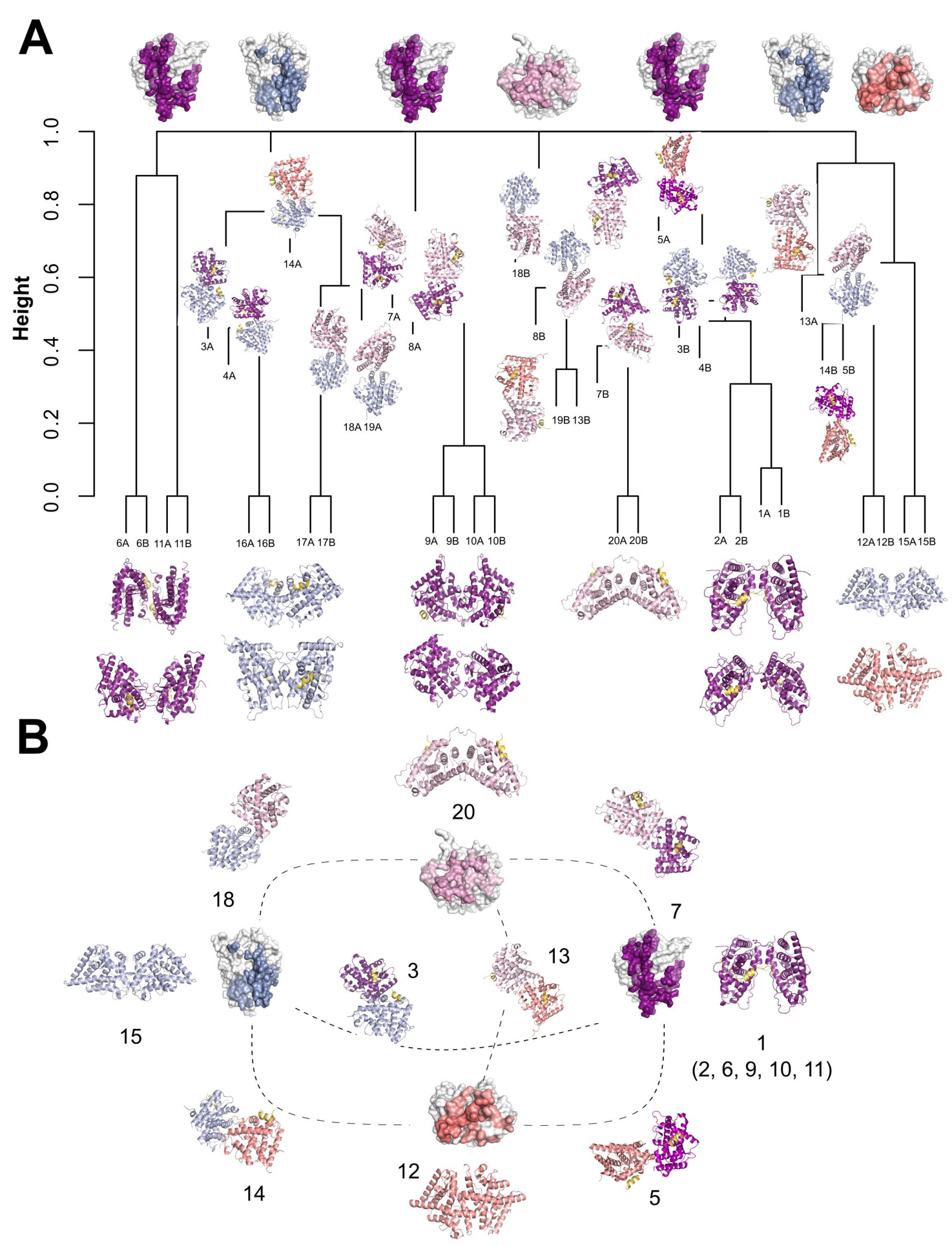
A
Height
1.0
0.8
0.6
0.4
0.2
0.0
6A 6B 11A 11B
16A 16B
17A 17B
9A 9B 10A 10B
20A 20B
2A 2B
1A 1B
12A 12B 15A 15B
3A
4A
14A
18A 19A
7A
8A
18B
19B 13B
8B
7B
5A
3B
4B
13A
14B 5B
B
20
18
7
15
3
13
1
(2, 6, 9, 10, 11)
14
12
5

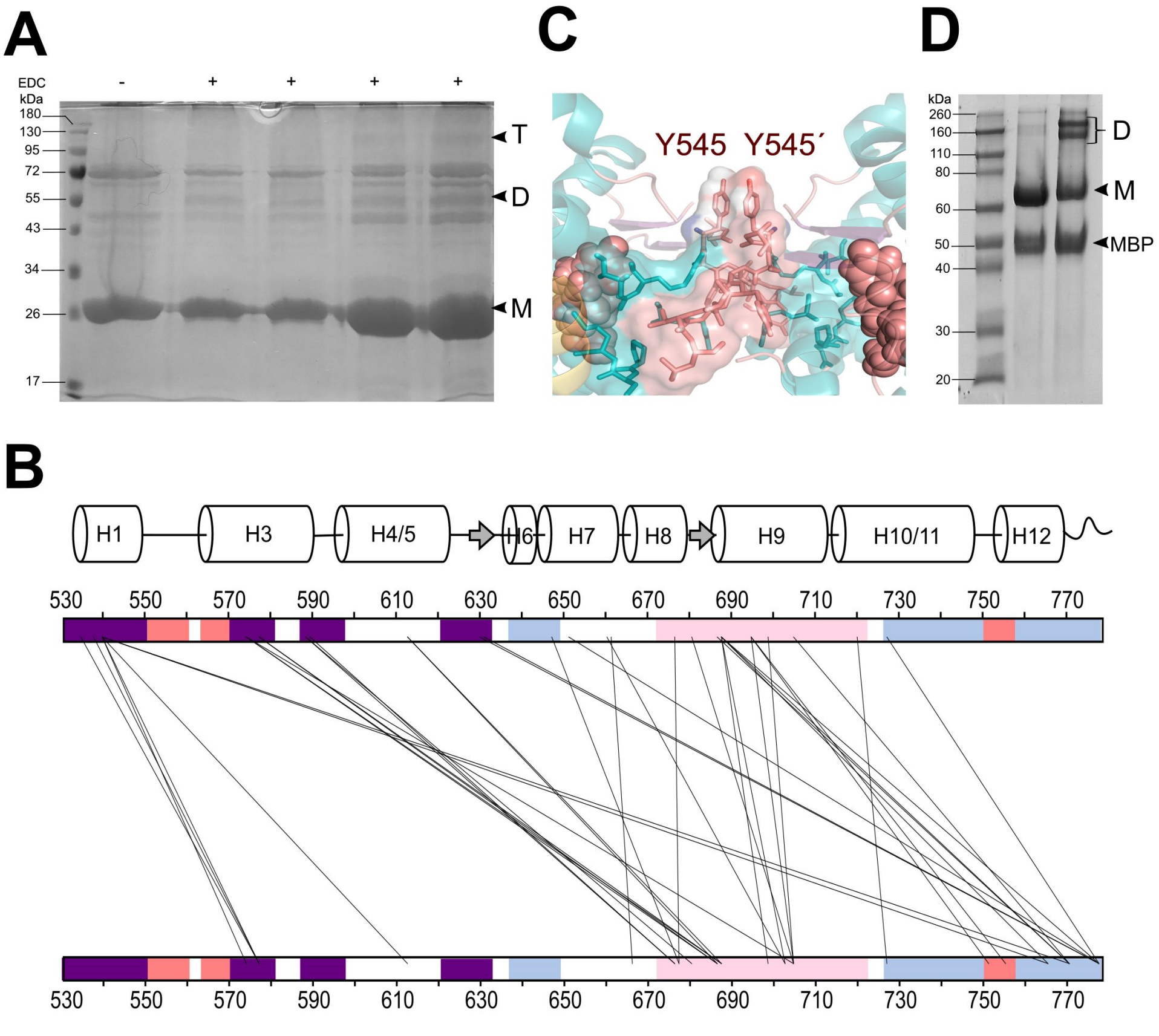
A
EDC
kDa
-
+
+
+
+
180
130
95
72
55
43
34
26
17
T
D
M
C
Y545 Y545´
D
kDa
260
160
110
80
60
50
40
30
20
D
M
MBP
B
H1
H3
H4/5
H6
H7
H8
H9
H10/11
H12
530
550
570
590
610
630
650
670
690
710
730
750
770

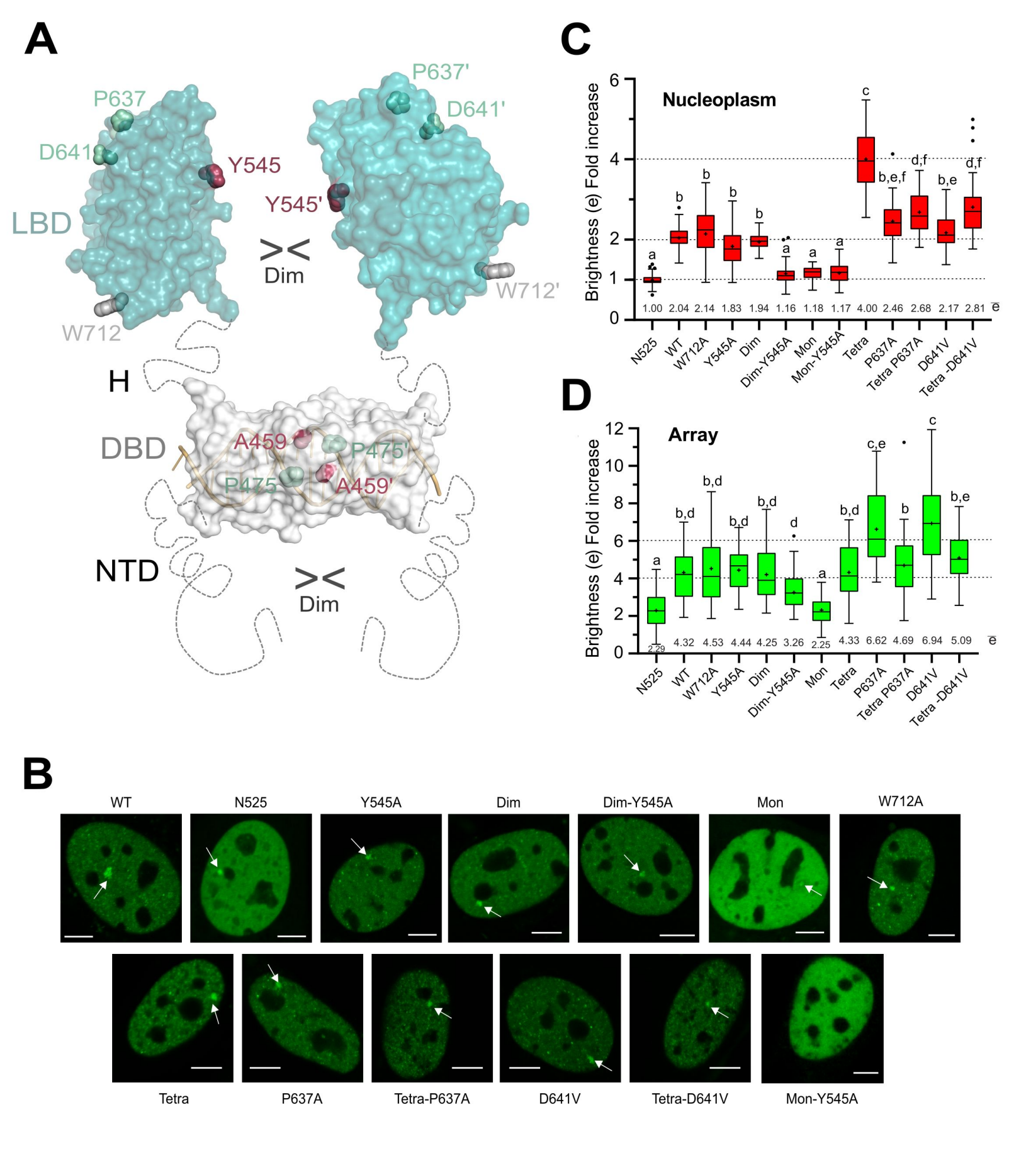
A
P637
D641
Y545
LBD
P637'
D641'
Y545'
W712'
W712
Dim
H
DBD
A459
P475'
P475
A459'
NTD
Dim
C
Nucleoplasm
Brightness (e) Fold increase
1.00 2.04 2.14 1.83 1.94 1.16 1.18 1.17 4.00 2.46 2.68 2.17 2.81
N525
WT
W712A
Y545A
Dim
Dim-Y545A
Mon
Mon-Y545A
Tetra
P637A
Tetra P637A
D641V
Tetra -D641V
D
Array
Brightness (e) Fold increase
2.29 4.32 4.53 4.44 4.25 3.26 2.25 4.33 6.62 4.69 6.94 5.09
B
WT
N525
Y545A
Dim
Dim-Y545A
Mon
W712A
Tetra
P637A
Tetra-P637A
D641V
Tetra-D641V
Mon-Y545A

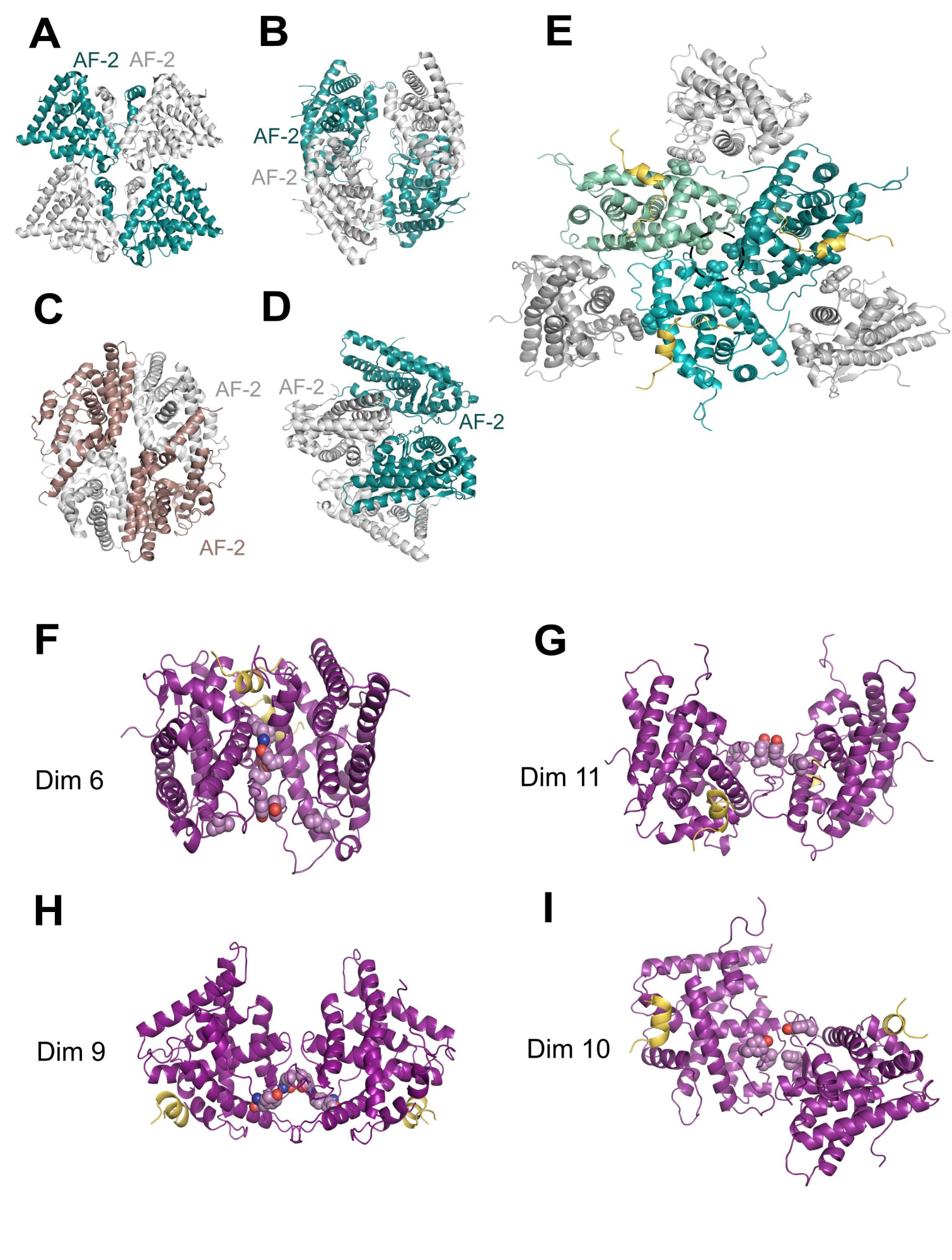
A
AF-2
AF-2
B
AF-2
AF-2
E
C
AF-2
AF-2
D
AF-2
AF-2
F
Dim 6
G
Dim 11
H
Dim 9
I
Dim 10

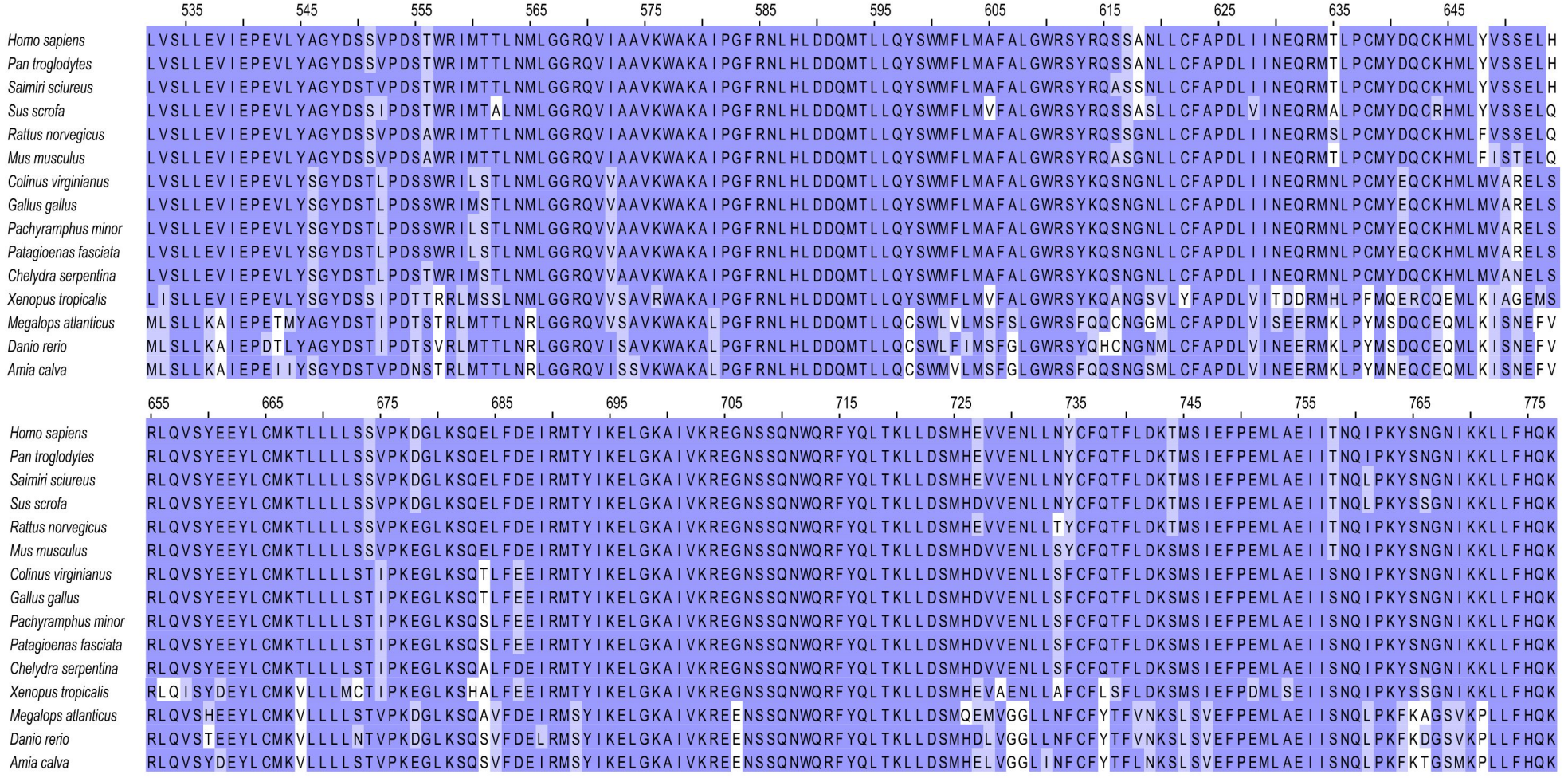
535 545 555 565 575 585 595 605 615 625 635 645
Homo sapiens LVSLLEVIEPEVLYAGYDSSVPDSTWRIMTTLNMLGGRQVIAAVKWAKAIPGFRNLHLDDQMTLLQYSWMFLMAFALGWRSYRQSSANLLCFAPDLIINEQRMTLPCMYDQCKHMLYVSSELH
Pan troglodytes LVSLLEVIEPEVLYAGYDSSVPDSTWRIMTTLNMLGGRQVIAAVKWAKAIPGFRNLHLDDQMTLLQYSWMFLMAFALGWRSYRQSSANLLCFAPDLIINEQRMTLPCMYDQCKHMLYVSSELH
Saimiri sciureus LVSLLEVIEPEVLYAGYDSTVPDSTWRIMTTLNMLGGRQVIAAVKWAKAIPGFRNLHLDDQMTLLQYSWMFLMAFALGWRSYRQASSNLLCFAPDLIINEQRMTLPCMYDQCKHMLYVSSELH
Sus scrofa LVSLLEVIEPEVLYAGYDSSIPDSTWRIMTALNMLGGRQVIAAVKWAKAIPGFRNLHLDDQMTLLQYSWMFLMVFALGWRSYRQSSASLLCFAPDLVINEQRMALPCMYDQCRHMLYVSSELQ
Rattus norvegicus LVSLLEVIEPEVLYAGYDSSVPDSAWRIMTTLNMLGGRQVIAAVKWAKAIPGFRNLHLDDQMTLLQYSWMFLMAFALGWRSYRQSSGNLLCFAPDLIINEQRMSLPCMYDQCKHMLFVSSELQ
Mus musculus LVSLLEVIEPEVLYAGYDSSVPDSAWRIMTTLNMLGGRQVIAAVKWAKAIPGFRNLHLDDQMTLLQYSWMFLMAFALGWRSYRQASGNLLCFAPDLIINEQRMTLPCMYDQCKHMLFISTELQ
Colinus virginianus LVSLLEVIEPEVLYSGYDSTLPDSSWRILSTLNMLGGRQVVAAVKWAKAIPGFRNLHLDDQMTLLQYSWMFLMAFALGWRSYKQSNGNLLCFAPDLIINEQRMNLPCMYEQCKHMLMVARELS
Gallus gallus LVSLLEVIEPEVLYSGYDSTLPDSSWRIMSTLNMLGGRQVVAAVKWAKAIPGFRNLHLDDQMTLLQYSWMFLMAFALGWRSYKQSNGNLLCFAPDLIINEQRMNLPCMYEQCKHMLMVARELS
Pachyramphus minor LVSLLEVIEPEVLYSGYDSTLPDSSWRILSTLNMLGGRQVVAAVKWAKAIPGFRNLHLDDQMTLLQYSWMFLMAFALGWRSYKQSNGNLLCFAPDLIINEQRMNLPCMYEQCKHMLMVARELS
Patagioenas fasciata LVSLLEVIEPEVLYSGYDSTLPDSSWRILSTLNMLGGRQVVAAVKWAKAIPGFRNLHLDDQMTLLQYSWMFLMAFALGWRSYKQSNGNLLCFAPDLIINEQRMNLPCMYEQCKHMLMVARELS
Chelydra serpentina LVSLLEVIEPEVLYSGYDSTLPDSTWRIMSTLNMLGGRQVVAAVKWAKAIPGFRNLHLDDQMTLLQYSWMFLMAFALGWRSYKQSNGNLLCFAPDLIINEQRMNLPCMYDQCKHMLMVANELS
Xenopus tropicalis LISLLEVIEPEVLYSGYDSSIPDTTRRLMSSLNMLGGRQVVSAVRWAKAIPGFRNLHLDDQMTLLQYSWMFLMVFALGWRSYKQANGSVLYFAPDLVITDDRMHLPFMQERCQEMLKIAGEMS
Megalops atlanticus MLSLLKAIEPETMYAGYDSTIPDTSTRLMTTLNRLGGRQVVSAVKWAKALPGFRNLHLDDQMTLLQCSWLVLMSFSLGWRSFQQCNGGMLCFAPDLVISEERMKLPYMSDQCEQMLKISNEFV
Danio rerio MLSLLKAIEPDTLYAGYDSTIPDTSVRLMTTLNRLGGRQVISAVKWAKALPGFRNLHLDDQMTLLQCSWLFIMSFGLGWRSYQHCNGNMLCFAPDLVINEERMKLPYMSDQCEQMLKISNEFV
Amia calva MLSLLKAIEPEIIYSGYDSTVPDNSTRLMTTLNRLGGRQVISSVKWAKALPGFRNLHLDDQMTLLQCSWMVLMSFGLGWRSFQQSNGSMLCFAPDLVINEERMKLPYMNEQCEQMLKISNEFV
655 665 675 685 695 705 715 725 735 745 755 765 775
Homo sapiens RLQVSYEEYLCMKTLLLLSSVPKDGLKSQELFDEIRMTYIKELGKAIVKREGNSSQNWQRFYQLTKLLDSMHEVVENLLNYCFQTFLDKTMSIEFPEMLAEIITNQIPKYSNGNIKKLLFHQK
Pan troglodytes RLQVSYEEYLCMKTLLLLSSVPKDGLKSQELFDEIRMTYIKELGKAIVKREGNSSQNWQRFYQLTKLLDSMHEVVENLLNYCFQTFLDKTMSIEFPEMLAEIITNQIPKYSNGNIKKLLFHQK
Saimiri sciureus RLQVSYEEYLCMKTLLLLSSVPKDGLKSQELFDEIRMTYIKELGKAIVKREGNSSQNWQRFYQLTKLLDSMHEVVENLLNYCFQTFLDKTMSIEFPEMLAEIITNQLPKYSNGNIKKLLFHQK
Sus scrofa RLQVSYEEYLCMKTLLLLSSVPKDGLKSQELFDEIRMTYIKELGKAIVKREGNSSQNWQRFYQLTKLLDSMHDVVENLLNYCFQTFLDKTMSIEFPEMLAEIITNQLPKYSSGNIKKLLFHQK
Rattus norvegicus RLQVSYEEYLCMKTLLLLSSVPKEGLKSQELFDEIRMTYIKELGKAIVKREGNSSQNWQRFYQLTKLLDSMHEVVENLLTYCFQTFLDKTMSIEFPEMLAEIITNQIPKYSNGNIKKLLFHQK
Mus musculus RLQVSYEEYLCMKTLLLLSSVPKEGLKSQELFDEIRMTYIKELGKAIVKREGNSSQNWQRFYQLTKLLDSMHDVVENLLSYCFQTFLDKSMSIEFPEMLAEIITNQIPKYSNGNIKKLLFHQK
Colinus virginianus RLQVSYEEYLCMKTLLLLSTIPKEGLKSQTLFEEIRMTYIKELGKAIVKREGNSSQNWQRFYQLTKLLDSMHDVVENLLSFCFQTFLDKSMSIEFPEMLAEIISNQIPKYSNGNIKKLLFHQK
Gallus gallus RLQVSYEEYLCMKTLLLLSTIPKEGLKSQTLFEEIRMTYIKELGKAIVKREGNSSQNWQRFYQLTKLLDSMHDVVENLLSFCFQTFLDKSMSIEFPEMLAEIISNQIPKYSNGNIKKLLFHQK
Pachyramphus minor RLQVSYEEYLCMKTLLLLSTIPKEGLKSQSLFEEIRMTYIKELGKAIVKREGNSSQNWQRFYQLTKLLDSMHDVVENLLSFCFQTFLDKSMSIEFPEMLAEIISNQIPKYSNGNIKKLLFHQK
Patagioenas fasciata RLQVSYEEYLCMKTLLLLSTIPKEGLKSQSLFEEIRMTYIKELGKAIVKREGNSSQNWQRFYQLTKLLDSMHDVVENLLSFCFQTFLDKSMSIEFPEMLAEIISNQIPKYSNGNIKKLLFHQK
Chelydra serpentina RLQVSYEEYLCMKTLLLLSTIPKEGLKSQALFDEIRMTYIKELGKAIVKREGNSSQNWQRFYQLTKLLDSMHDVVENLLSFCFQTFLDKSMSIEFPEMLAEIISNQIPKYSNGNIKKLLFHQK
Xenopus tropicalis RLQISYDEYLCMKVLLLMCTIPKEGLKSHALFEEIRMTYIKELGKAIVKREGNSSQNWQRFYQLTKLLDSMHEVAENLLAFCFLSFLDKSMSIEFPDMLSEIISNQIPKYSSGNIKKLLFHQK
Megalops atlanticus RLQVSHEEYLCMKVLLLLSTVPKDGLKSQAVFDEIRMSYIKELGKAIVKREENSSQNWQRFYQLTKLLDSMQEMVGGLLNFCFYTFVNKSLSVEFPEMLAEIISNQLPKFKAGSVKPLLFHQK
Danio rerio RLQVSTEEYLCMKVLLLLNTVPKDGLKSQSVFDELRMSYIKELGKAIVKREENSSQNWQRFYQLTKLLDSMHDLVGGLLNFCFYTFVNKSLSVEFPEMLAEIISNQLPKFKDGSVKPLLFHQK
Amia calva RLQVSYDEYLCMKVLLLLSTVPKEGLKSQSVFDEIRMSYIKELGKAIVKREENSSQNWQRFYQLTKLLDSMHELVGGLINFCFYTFLNKSLSVEFPEMLAEIISNQLPKFKTGSMKPLLFHQK

A GR WT vs GR WT

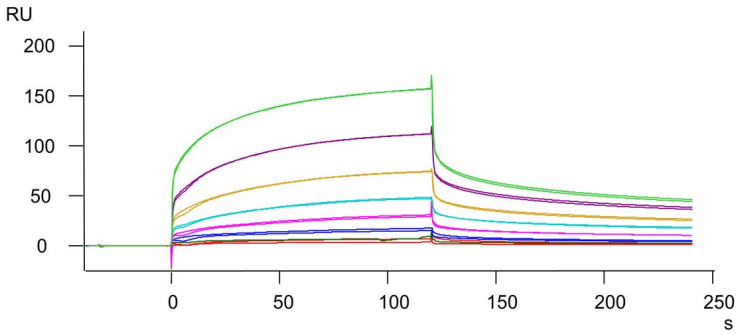

1:1	Multisite	
kD = 15.3 µM ± 0.9 µM	kD_1 = 2.2 µM ± 0.4 µM	kD_2 = 27.8 µM ± 1,9 µM
Rmax = 243. 8 RU	$Rmax_1$ = 35 RU	$Rmax_2$ = 262.5 RU
Chi^2 = 4.52	Chi^2 = 1.25	

B

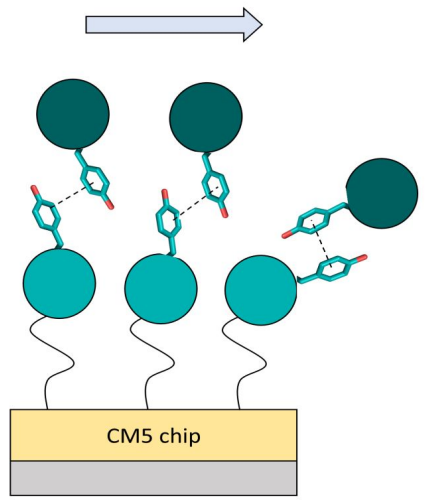

C GR Y545C vs GR Y545C

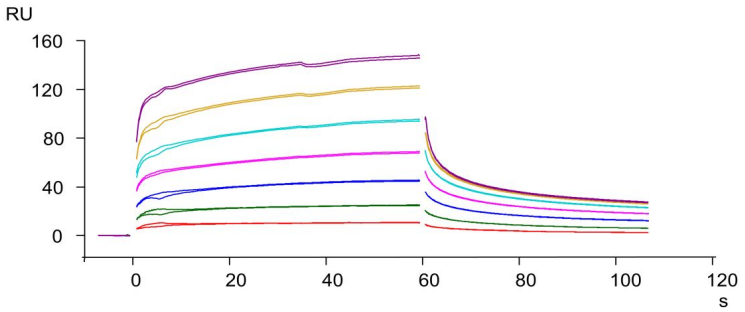

1:1	Multisite	
kD = 7.9 µM ± 0.6 µM	kD_1 = 0.8 µM ± 0.8 µM	kD_2 = 8.9 µM ± 0.7 µM
Rmax = 162.5 RU	$Rmax_1$ = 12 RU	$Rmax_2$ = 157.9 RU
Chi^2 = 3.1	Chi^2 = 2.5	

D

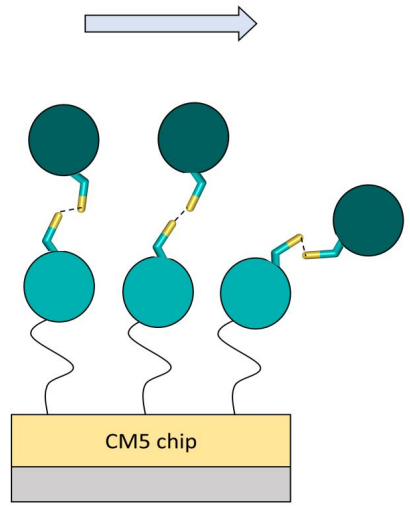

E GR Y545A vs GR Y545A

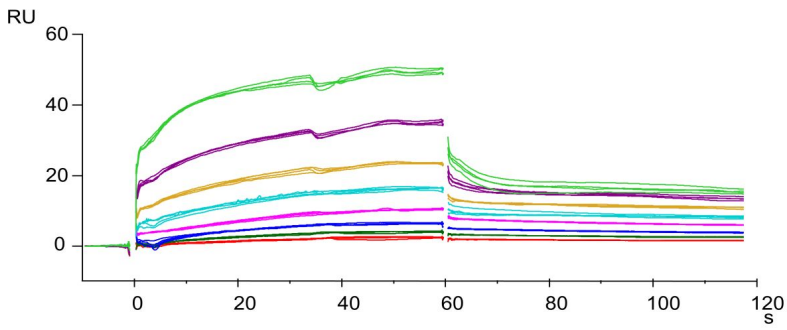

1:1	Multisite	
kD = 31.1 µM ± 2.1 µM	kD_1 = 2.2 µM ± 0.4 µM	kD_2 = 60.7 µM ± 2.8 µM
Rmax = 75.1 RU	$Rmax_1$ = 10 RU	$Rmax_2$ = 87.43 RU
Chi^2 = 0.9	Chi^2 = 0.17	

F

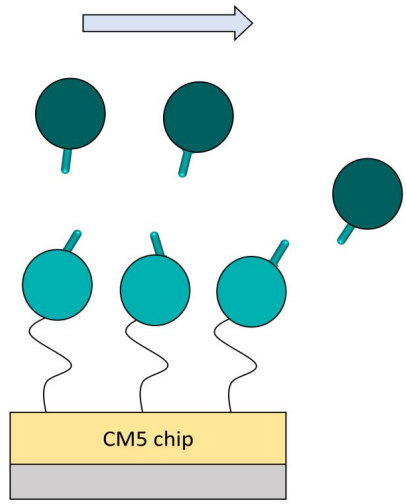

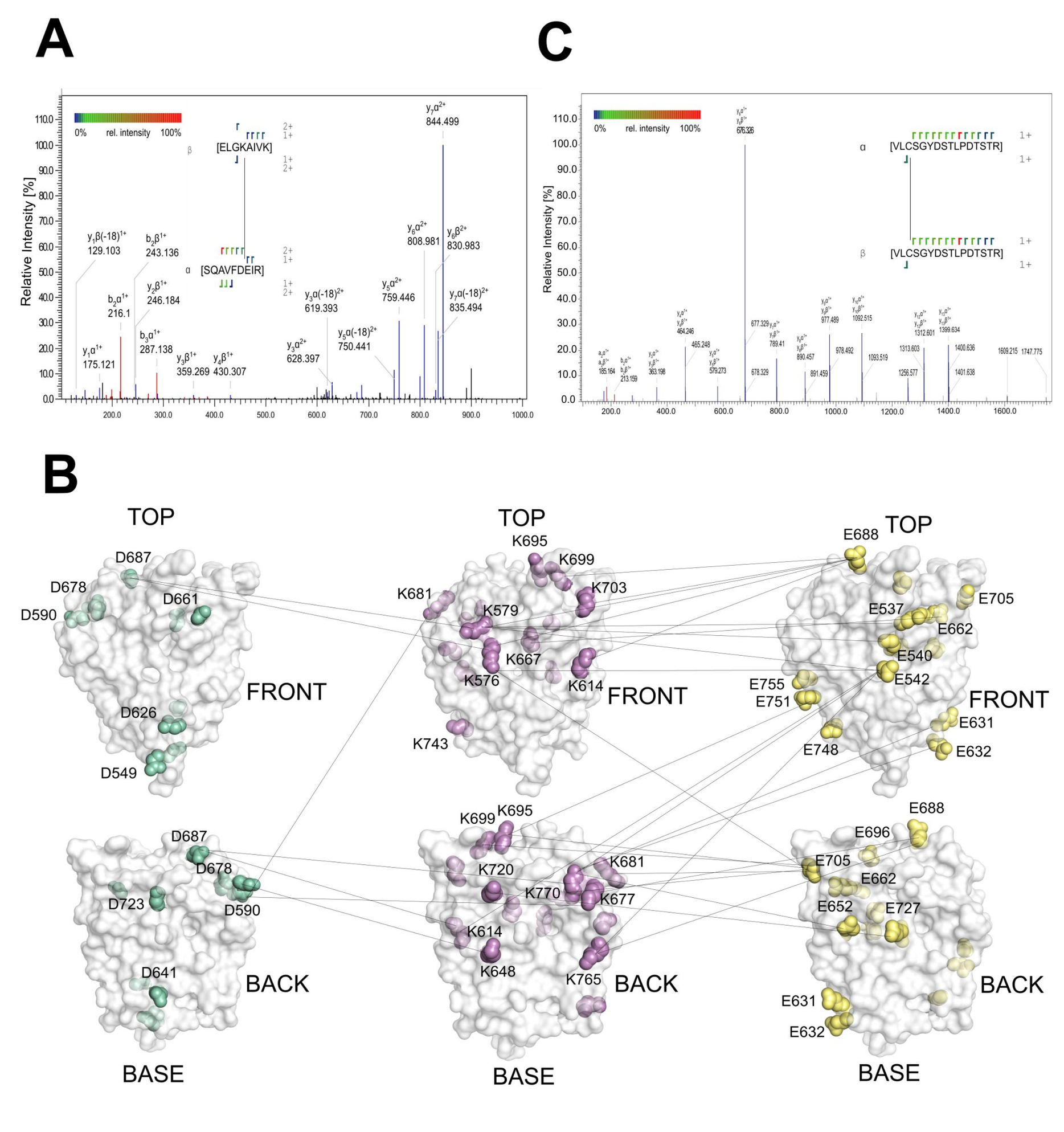
A
C
B
Relative Intensity [%]
0% rel. intensity 100%
[ELGKAIVK]
[SQAVFDEIR]
[VLCSGYDSTLPDTSTR]
TOP
FRONT
BACK
BASE
D687
D678
D590
D661
D626
D549
D723
D641
K695
K699
K703
K681
K579
K667
K576
K614
K743
K720
K770
K677
K648
K765
E688
E705
E537
E662
E540
E542
E755
E751
E748
E631
E632
E696
E652
E727

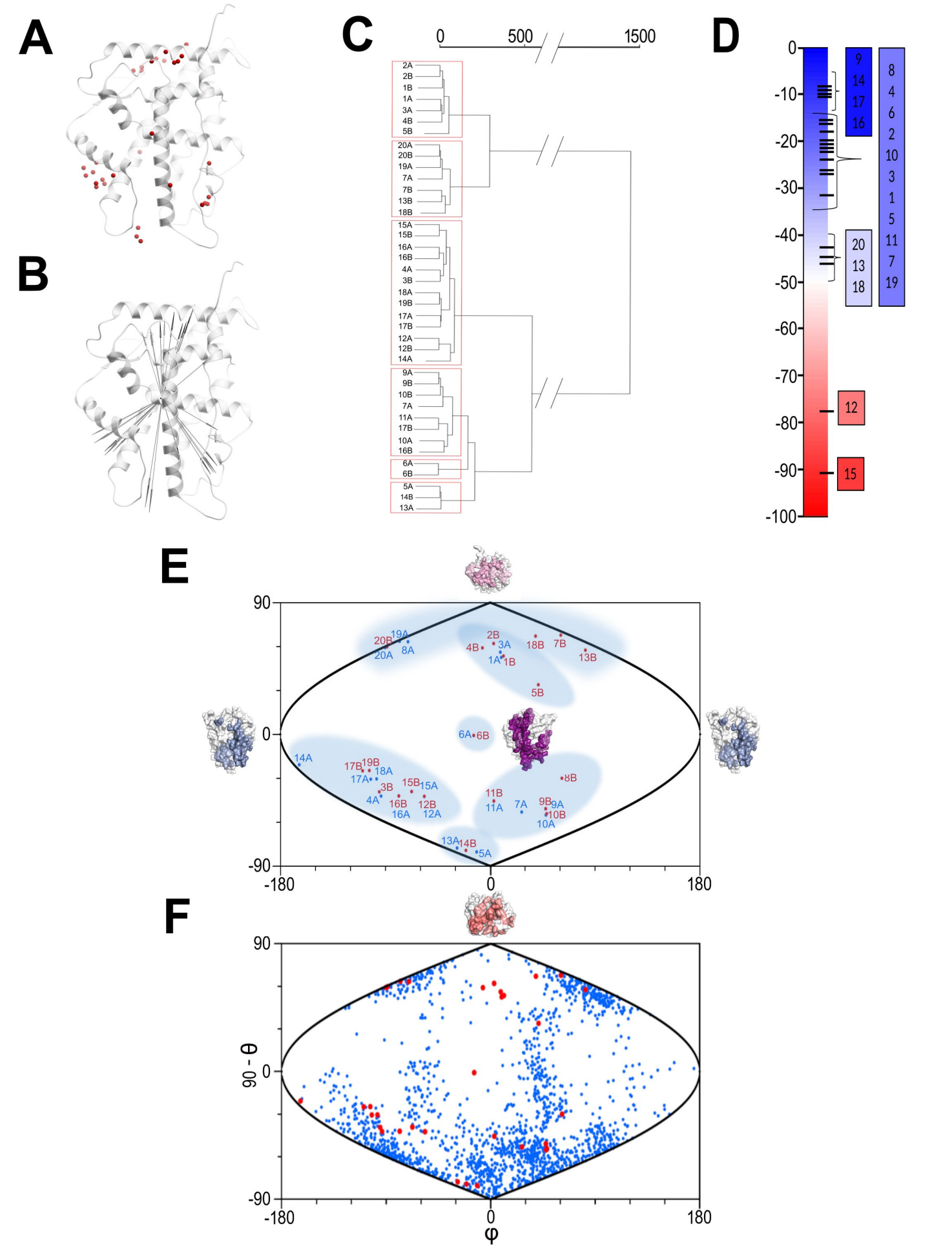
A
B
C
0
500
1500
2A
2B
1B
1A
3A
4B
5B
20A
20B
19A
7A
7B
13B
18B
15A
15B
16A
16B
4A
3B
18A
19B
17A
17B
12A
12B
14A
9A
9B
10B
7A
11A
17B
10A
16B
6A
6B
5A
14B
13A
D
0
-10
-20
-30
-40
-50
-60
-70
-80
-90
-100
9
14
17
16
8
4
6
2
10
3
1
5
11
7
19
20
13
18
12
15
E
90
0
-90
-180
0
180
20B
19A
20A
8A
2B
4B
3A
1A
1B
18B
7B
13B
5B
6A
6B
14A
17B
19B
18A
17A
3B
15B
15A
4A
16B
12B
16A
12A
8B
11B
11A
7A
9B
9A
10B
10A
13A
14B
5A
F
90
0
-90
-180
0
180
90 - θ
φ

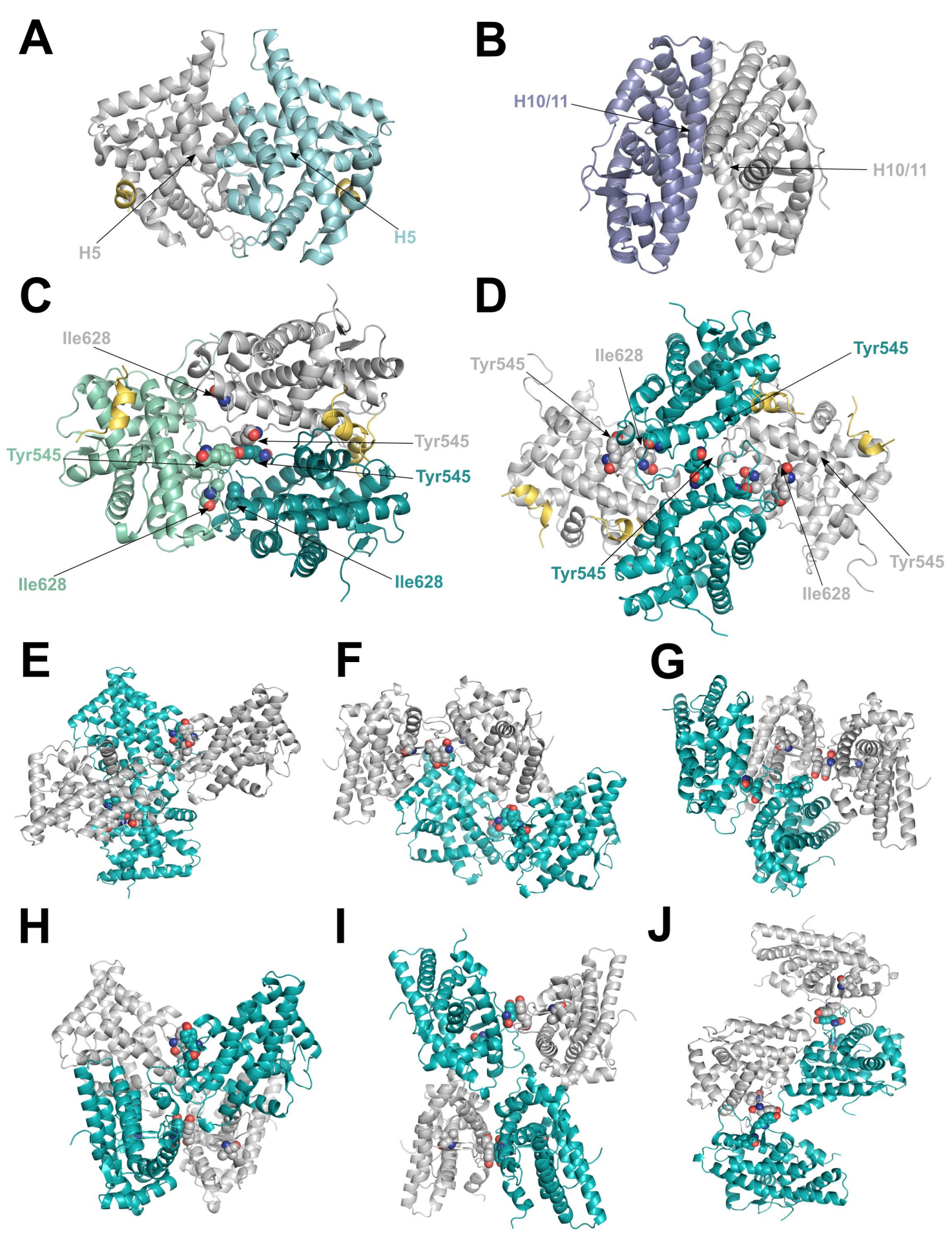
A
H5
H5
B
H10/11
H10/11
C
Ile628
Tyr545
Tyr545
Tyr545
Ile628
Ile628
D
Tyr545
Ile628
Tyr545
Tyr545
Tyr545
Ile628
E
F
G
H
I
J

	GR WT 1	GR WT 2	GR WT 3	GR WT 4	GR WT 5
PDB code	XXX	YYY	ZZZ	VVV	WWW
Wavelength (Å)	0.9	0.9	0.9	0.9	0.9
Resolution range	43.42-2.25 (2.32-2.25)	76.81-2.30 (2.42-2.30)	94.81-2.46 (2.56-2.46)	90.10-2.99 (3.18-2.99)	72.80-3.36 (3.63-3.36)
Space group	C121	P31	P61	$I4_122$	$I4_132$
Cell dimensions a, b, c (Å) α, β, γ (˚)	86.61, 52.44, 69.60 90.0, 116.62, 90.0	107.60, 107.60, 135.64 90.0, 90.0, 120.0	109.36,109.36, 137.77 90.0, 90.0, 120.0	180.20, 180.20, 169.18, 90.0, 90.0, 90.0	178.05, 178.05, 178.05 90.00, 90.00, 90.00
Total reflections	34,022 (1,954)	156,013 (22,547)	94,861 (11,087)	223,344 (40,285)	82,328 (16,909)
Unique reflections	12,530 (907)	73,686 (10,882)	33,009 (3,799)	23,704 (4,229)	7,178 (1,431)
Multiplicity	2.7 (2.2)	2.1 (2.1)	2.9 (2.9)	9.4 (9.5)	11.5 (11.8)
Completeness (%)	93.8 (75.5)	94.4 (95.6)	96.8 (98.5)	100.0 (100.0)	100.0 (100.0)
Mean I/sigma(I)	11.1 (1.8)	5.9 (1.4)	7.4 (0.7)	6.6 (2.2)	10.8 (1.7)
Wilson B-factor	44.7	45.0	57.5	73.5	141.0
R-meas	0.069 (0.697)	0.125 (0.987)	0.074 (1.050)	0.307 (1.701)	0.108 (1.762)
R-pim	0.039 (0.439)	0.079 (0.641)	0.051 (0.725)	0.149 (0.815)	0.031 (0.505)
CC1/2	0.997 (0.654)	0.986 (0.314)	0.994 (0.317)	0.982 (0.386)	1.000 (0.561)
Reflections used in refinement	12,018	69,901	31,272	22,492	6,809
Reflections used for R-free	510 (4.1%)	3,765 (5.1%)	1,692 (5.1%)	1,194 (5.0%)	344 (4.8%)
R-work	0.192	0.177	0.216	0.242	0.199
R-free	0.245	0.220	0.247	0.280	0.288
Total number of atoms	2,146	8280	4,190	6,109	2,111
RMS (bonds)	0.007	0.010	0.007	0.006	0.006
RMS (angles)	1.565	2.016	1.655	1.555	1.727
Ramachandran favored (%)	96.00	95.93	93.16	89.38%	84.55
Ramachandran allowed (%)	100.0	99.3	99.0	98.9%	95.9
Clashscore	12.86	13.16	9.36	27.61	29.6
Average B-factor	54.0	50.0	68.0	67.0	142.0

PDB code	Space group	Res. (Å)	Cell constants	Protein
5UFS	C2	2.12	a = 87.0, b = 52.8, c = 126.0 Å, b = 101.8°	ancGR2
3K23	C2	3	a = 184.9, b = 66.0, c = 71.5 Å, b = 103.6°	hGR_3CLD
3RY9	C2	1.95	a = 139.4, b = 49.1, c = 100.4 Å, b = 105.8°	ancGR1[1]
5UC3	C2	2	a = 136.7, b = 88.3, c = 64.7 Å, b = 110.8°	hGR_5UC3
This work	C2	2.15	a = 91.1, b = 90.8, c = 157.2 Å, b = 116.6º	ancGR2
1NHZ	P21212	2.3	a = 74.9, b = 109.8, c = 39.3 Å	hGR_1NHZ
4LSJ	P21212	2.35	a = 39.0, b = 139.4, c = 48.1 Å	hGR_3CLD
6NWK	C2221	1.65	a = 71.7, b = 96.4, c = 107.9 Å	ancGR2
6NWL	C2221	1.59	a = 71.7, b = 96.4, c = 108.2 Å	ancGR2
1P93[3]	P31	2.7	a = b = 127.4, c = 91.8 Å, g = 120°	hGR_1NHZ
This work	P31	2.7	a = b = 107.75, c = 135.8 Å, g = 120°	ancGR2
3GN8	P61	2.5	a = b = 104.2, c = 144.2 Å, g = 120°	ancGR2
4E2J	P61	2.5	a = b = 104.4, c = 143.9 Å, g = 120°	ancGR2
1M2Z	P61	2.5	a = b = 125.8, c = 86.0 Å, g = 120°	hGR_1M2Z
3CLD	P61	2.84	a = b = 127.3, c = 77.8 Å, g = 120°	hGR_3CLD
3E7C	P61	2.15	a = b = 126.6, c = 79.0 Å, g = 120°	hGR_3CLD
3K22	P61	2.1	a = b = 127,6, c = 78.2 Å, g = 120°	hGR_3CLD
4P6X	P61	2.5	a = b = 220.8, c = 74.2 Å, g = 120°	hGR_4P6X
5UC1	P61	2.35	a = b = 48.4, c = 385.8 Å, g = 120°	HetgaGRβ
This work	P61	2.7	a = b = 190.6, c = 137.9 Å, g = 120°	ancGR2
3BQD	P62	2.5	a = b = 93.8, c = 130.0 Å, g = 120°	hGR_1M2Z
3MNE	P65	1.96	a = b = 71.8, c = 128.6 Å, g = 120°	mGR
3MNP	P65	1.5	a = b = 72.1, c = 128.8 Å, g = 120°	mGR
3MNO	P65	1.55	a = b = 71.4, c = 127.9 Å, g = 120°	mGR
3H52	P3221	2.8	a = b = 99.5, c = 252.4 Å, g = 120°	hGR_3H52
4MDD	P3221	2.4	a = b = 72.5, c = 229.5 Å, g = 120°	hGR_3H52
4CSJ	P3221	2.3	a = b = 84.4, c = 105.7 Å, g = 120°	hGR_4CSJ
4UDC	P3221	2.5	a = b = 84.7, c = 105.9 Å, g = 120°	hGR_1NHZ
4UDD	P3221	1.8	a = b = 87.2, c = 102.9 Å, g = 120°	hGR_4CSJ
5G3J	P3221	2.4	a = b = 84.3, c = 106.7 Å, g = 120°	hGR_4CSJ
5G5W	P3221	2.2	a = b = 83.9, c = 105.7 Å, g = 120°	hGR_4CSJ
5NFP	P3221	2.1	a = b = 84.0, c = 106.1 Å, g = 120°	hGR_4CSJ
5NFT	P3221	2.3	a = b = 84.4, c = 106.1 Å, g = 120°	hGR_5NFT
6EL6	P3221	2.4	a = b = 85.0, c = 106.4 Å, g = 120°	hGR_4CSJ
6EL7	P3221	2.18	a = b = 83.8, c = 106.0 Å, g = 120°	hGR_5NFT
6EL9	P3221	2.19	a = b = 84.5, c = 105.7 Å	hGR_5NFT
This work	I4122	3.18	a = b = 180.3, c = 169.2 Å	ancGR2
4P6W	P23	1.95	a = b = c = 130.2 Å	hGR_4P6W
This work	I4132	3.36	a = b = c = 178.05 Å	ancGR2

[1] Sequence not identical to ancGR1 – rather an intermediate between ancGR1 and ancGR2.

[2] His-Ser-Ser-Arg-Leu-Trp-Glu-Leu-Leu-Met-Glu-Ala-Thr. (Leucines of the LXXLL motif are underlined).

[3] Structure not refined. (R 34.5%, Rfree 36.3%, and worrisome MolProbity statistics).

[4] Only residues Asn742-Asp752 defined by electron density.

Ligands		
LBP	AF-2	Dimer interfaces (DIs) and other pockets
1TA	SHP (17-27), R17A	–
JZN	SRC2 (740-751)	–
DOC	–	GOL (DI)
RU-486	–	EDO (DI), HEPES, MPD
DEX	SHP (12-30)	–
RU-486	–	HEX (3 molecules, two at two different DIs)
LSJ	Synthetic peptide[2]	LSJ (DI)
DEX	PGC1a (141-152)	ACE, FMT (DI #1), DMS (one at DI #2), GOL
HYC	PGC1a (141-152)	GOL (one at DI #1), HEPES, SCN (one at DI #2), TLA
DEX	SRC2 (939-950)	–
DEX	SHP (12-30)	–
DEX	SRC2 (734-754)[4]	–
MOF	SRC2 (741-752), GOL	FMT, GOL (DI)
DEX	SRC2 (734-754)	BOG (3 molecules at the DI)
GW6	SRC2 (740-751)	–
GSK866	SRC2 (741-751)	GOL (3 molecules, one at DI)
JZS	SRC2 (740-751)	JZR (fully embedded in DI)
HCY	SRC2 (740-753)	–
RU-486	–	RU-486 (two molecules fully embedded in DI #1), CHAPS (two molecu
DEX	SHP (12-30)	–
DAY	SRC1 (739-751)	–
DEX	SRC2 (740-752)	GOL (2 molecules, one at the DI)
DEX	SRC2 (740-752)	GOL (2 molecules, one at DI #1), SCN (2 molecules, one at DI #2)
DEX	SRC2 (740-752)	SCN (2 molecules at DIs #1 and #2), GOL (at a 3rd DI)
RU-486	NCOR1 (2260-2274)	GOL
29M	NCOR1 (1-14)	–
NN7	SRC2 (741-753)	EDO
DEX	SRC2 (741-753)	CHAPS (at DI)
CV7	SRC2 (741-753)	CHAPS (at DI)
E7T	SRC2 (741-753)	CHAPS (at DI), EDO
R8C	SRC2 (741-753)	EDO
8W5	SRC2 (741-753)	CHAPS (at DI), EDO, GOL
8W8	SRC2 (741-753)	EDO
B9Q	SRC2 (740-753)	EDO
B9T	SRC2 (740-753)	EDO
B9W	SRC2 (740-753)	EDO
DEX	SHP (12-30)	DEX (embedded in DI)
MOF	SRC2 (741-752)	–
DEX	SHP (12-30)	DEX (embedded in DI)

les in DI #1, 3rd molecule in DI #2), CL (DI #2), EDO, MPD

				Oligomer
Peptide 1	**A site**	**Peptide 2**	**B site**	**MH+ (theo)**
E^{537}VIEPEVLY^{545}	Glu537 / H1	A^{578}**K**ALPGF^{584}	Lys579 / H3	1774.96
E^{537}VIEPEVLY^{545}	Glu537 / H1	A^{578}**K**ALPGFRNL	Lys579 / H3	2158.19
E^{537}VI**E**PEVL^{544}	Glu540 / L1-3	A^{578}**K**ALPGF^{584}	Lys579 / H3	1611.9
E^{537}VI**E**PEVLY^{545}	Glu540 / L1-3	A^{578}**K**ALPGF^{584}	Lys579 / H3	1774.96
E^{537}VI**E**PEVLY^{545}	Glu540 / L1-3	A^{578}**K**ALPGFRNL	Lys579 / H3	2158.19
E^{537}VIEP**E**VL^{544}	Glu542 / L1-3	G^{567}GRQVVSAV	Lys576 / H3	2095.15
E^{537}VIEP**E**VLY^{545}	Glu542 / L1-3	G^{567}GRQVVSAV	Lys576 / H3	2258.22
E^{537}VIEP**E**VLY^{545}	Glu542 / L1-3	N^{564}RLGGRQVV	Lys576 / H3	2641.45
P^{530}TLISLLEVIEP GYDSTLPDTSTR	Glu542 / L1-3	Q^{570}VVSAV**K**WA	Lys576 / H3	4305.29
E^{537}VIEP**E**VL^{544}	Glu542 / L1-3	A^{578}**K**ALPGF^{584}	Lys579 / H3	1611.9
E^{537}VIEP**E**VL^{544}	Glu542 / L1-3	A^{578}**K**ALPGFRNL	Lys579 / H3	1995.13
E^{537}VIEP**E**VLY^{545}	Glu542 / L1-3	A^{578}**K**ALPGF^{584}	Lys579 / H3	1774.96
E^{537}VIEP**E**VLY^{545}	Glu542 / L1-3	A^{578}**K**ALPGFRNL	Lys579 / H3	2158.19
E^{537}VIEP**E**VLY^{545}	Glu542 / L1-3	**K**^{614}QSNGNML^{6}	Lys614 / H5	1978.98
E^{537}VIEP**E**VLY^{545}	Glu542 / L1-3	**K**^{765}AGSVKPL^{772}	Lys765 / H12	1871.05
E^{537}VIEP**E**VL^{544}	Glu542 / L1-3	K^{765}AGSV**K**PL^{772}	Lys770 / S4	1707.99
E^{537}VIEP**E**VLY^{545}	Glu542 / L1-3	K^{765}AGSV**K**PL^{772}	Lys770 / S4	1871.05
H^{588}L**D**DQMTL^{5}	Asp590 / H4-5	S^{672}TVPKDGL**K**S	Lys681 / L8-9	2446.23
H^{588}L**D**DQMTLL	Asp590 / H4-5	S^{672}TVPKDGL**K**S	Lys681 / L8-9	2559.31
H^{588}LD**D**QMTLL	Asp590 / H4-5	L^{671}STVP**K**DGLK	Lys677 / L8-9	2672.4
Q^{615}SNGNMLCF	Glu631 / H6	A^{766}GSVKPLLFH	Lys777 / C-t	3512.78
Q^{615}SNGNMLCF	Glu631 / H6	A^{766}GSVKPLLFH	Lys777 / C-t	3528.77
Q^{615}SNGNMLCF	Glu632 / H6	A^{766}GSVKPLLFH	Lys777 / C-t	3512.78
Q^{615}SNGNMLCF	Glu632 / H6	A^{766}GSVKPLLFH	Lys777 / C-t	3528.77
K^{648}ISS**E**F^{653}	Glu652 / H7	L^{773}FHQ**K**^{777}	Lys777 / C-t	1363.74
V^{654}RLQVSYD**E**Y	Glu662 / H8	C^{665}M**K**VLL^{670}	Lys667 / H8	2032.02
S^{673}TVPK**D**GL^{680}	Asp678 / L8-9	**K**^{648}ISSEF^{653}	Lys648 / H7	1507.8
S^{682}QAVF**D**EIR^{69}	Asp687 / H9	Q^{570}VVSAV**K**WA	Lys576 / H3	2161.18
S^{682}QAVF**D**EIR^{69}	Asp687 / H9	W^{577}A**K**ALPGFR	Lys579 / H3	2091.11
D^{687}EIRMTY^{693}	Asp687 / H9	**K**^{614}QSNGNML^{6}	Lys614 / H5	1831.83
S^{682}QAVF**D**EIR^{69}	Asp687 / H9	S^{612}Y**K**QSNGNM FAPDLVINEER^{63}	Lys614 / H5	3630.73
S^{682}QAVF**D**EIR^{69}	Asp687 / H9	S^{612}Y**K**QSNGNM FAPDLVINEER^{63}	Lys614 / H5	3646.73
S^{682}QAVF**D**EIR^{69}	Asp687 / H9	A^{766}GSV**K**PLLFH	Lys770 / S4	2370.29
S^{682}QAVFD**E**IR^{69}	Glu688 / H9	Q^{570}VVSAV**K**WA	Lys576 / H3	2161.18
S^{682}QAVFD**E**IR^{69}	Glu688 / H9	W^{577}A**K**ALPGFR	Lys579 / H3	2091.11
D^{687}**E**IRMTY^{693}	Glu688 / H9	**K**^{614}QSNGNML^{6}	Lys614 / H5	1831.83
S^{682}QAVFD**E**IR^{69}	Glu688 / H9	S^{612}Y**K**QSNGNM	Lys614 / H5	3630.73
S^{682}QAVFD**E**IR^{69}	Glu688 / H9	S^{612}Y**K**QSNGNM	Lys614 / H5	3646.73
S^{682}QAVFD**E**IR^{69}	Glu688 / H9	E^{696}LG**K**AIVK^{703}	Lys699 / H9	1903.06
S^{682}QAVFD**E**IR^{69}	Glu688 / H9	A^{700}IV**K**R^{704}	Lys703 / L9-10	1631.92
D^{687}**E**IRMTY^{693}	Glu688 / H9	**K**^{765}AGSVKPL^{772}	Lys765 / H12	1723.9
D^{687}**E**IRMTY^{693}	Glu688 / H9	**K**^{765}AGSVKPL^{772}	Lys770 / S4	1723.9
S^{682}QAVFD**E**IR^{69}	Glu688 / H9	A^{766}GSV**K**PLLFH	Lys770 / S4	2370.29

S[682]QAVFD**E**IR[69	Glu688 / H9	A[766]GSVKPLLFH	Lys777 / C-t	2370.29
E[705]GNSSQNW(	Glu705 / H9	Q[570]VVSAV**K**WA	Lys576 / H3	2302.17
E[705]GNSSQNW(	Glu705 / H9	D[678]GL**K**SQAVF	Lys681 / L8-9	2664.28
E[705]GNSSQNW(	Glu705 / H9	M[691]TYI**K**ELGK[69	Lys695 / H9	2269.1
E[705]GNSSQNW(	Glu705 / H9	M[691]TYI**K**ELGK[69	Lys695 / H9	2285.1
E[705]GNSSQNW(	Glu705 / H9	E[696]LG**K**AIVK[703]	Lys699 / H9	2044.06
E[705]GNSSQNW(	Glu705 / H9	A[766]GSV**K**PLLFH	Lys770 / S4	2511.29
L[722]DSMH**E**MV(	Glu727 / H10-1	Q[717]LT**K**LL[722]	Lys720 / H10-11	1916.98
L[722]DSMH**E**MV(	Glu727 / H10-1	Q[717]LT**K**LL[722]	Lys720 / H10-11	2030.07
Q[717]LTKLLDSMH	Glu727 / H10-1	T[719]**K**LL[722]	Lys720 / H10-11	1901.02
Q[717]LTKLLDSMH	Glu727 / H10-1	T[719]**K**LL[722]	Lys720 / H10-11	1917.02
Q[717]LTKLLDSMH	Glu727 / H10-1	T[719]**K**LL[722]	Lys720 / H10-11	1933.01
Y[716]QLTKLLDSM	Glu727 / H10-1	T[719]**K**LL[722]	Lys720 / H10-11	2080.08
Y[716]QLTKLLDSM	Glu727 / H10-1	Y[716]QLT**K**L[721]	Lys720 / H10-11	2355.21
D[723]SMH**E**MVG	Glu727 / H10-1	H[775]Q**K**[777]	Lys777 / C-t	1613.74
S[744]LSVEFP**E**ML	Glu751 / H12	M[691]TYI**K**ELGK[69	Lys695 / H9	3340.74
S[744]LSVEFPEML	Glu755 / H12	M[691]TYI**K**ELGK[69	Lys695 / H9	3340.74

Count		Average MH+ (exp)
Dim	Tetra	Dimer
1		1774.96228
1		2158.18928
1		1611.89828
1		1774.96228
1		2158.18828
2		2095.15378
2		2258.21778
1		2641.45228
2		4305.27978
1		1611.90028
1		1995.12728
	1	
2		2158.18993
1		1978.97828
1		1871.05128
1		1707.98828
2		1871.05178
3		2446.23094
2		2559.31028
1		2672.39628
5		3512.73379
1		3528.76428
2		3512.73745
1		3528.75828
1		1363.73516
1		2032.02228
1		1507.80235
2		2161.16389
1		2091.11328
1		1831.83028
2		3630.73453
2		3646.73477
	1	
6	1	2161.17542
1		2091.11428
2		1831.82678
3		3630.72128
3		3646.70528
11	2	1903.06413
4		1631.9221
1		1723.90264
	1	
	2	

1		2370.29628
2		2302.16954
	1	
9		2269.1015
9	2	2285.09668
1		2044.05828
16		2511.28502
1		1916.98128
1		2030.06528
5		1900.98772
5	2	1916.98137
5		1932.976
1		2080.04398
5		2355.17114
1		1613.74016
2		3340.74336
1		3340.74185

	Average δm	
Tetramer	Dimer	Tetramer
	0	
	-0.46335139	
	-0.62038654	
	0	
	-0.92670321	
	-0.23864602	
	-0.22141359	
	2.27147772	
	-2.43886623	
	0.62038577	
	0	
1774.96228		0
	-0.22277314	
	-0.50531126	
	-0.5344589	
	-0.58548411	
	-0.26722945	
	1.09011135	
	-0.7814607	
	0	
	-12.5019153	
	-2.26708257	
	-11.4588416	
	-3.96740125	
	-1.24503646	
	-0.98424118	
	1.38418009	
	-5.77495063	
	0	
	-0.5459021	
	0.82367906	
	2.2803852	
2370.29328		0
2161.17571	-0.44174584	-0.32651209
	0.47821394	
	-2.45656781	
	-2.75427374	
	-5.75862276	
1903.06472	-0.28240761	-0.00789802
	-0.40437143	
	-1.21469737	
1723.90728		1.74023281
2370.28728		-2.53133945

	1.26566456	
	0.45512975	
2664.27733		0.43307053
	-0.71892555	
2285.09782	-0.57981458	-0.03817383
	0.48922284	
	-0.04776769	
	-0.5216535	
	-0.492595	
	-18.802073	
1916.98124	-19.3066265	-19.3727039
	-19.2923812	
	-18.1369146	
	-15.9482651	
	-0.54110322	
	0.36453942	
	-0.00793237	

Peptide: α	**SQAVFDEIR**					
Charge: +1						
b	**b-H2O**	**b-NH3**	**AA**	**y**	**y-H2O**	**y-NH3**
88.039	70.029	71.013	S			
216.098	198.087	199.071	Q	1816.033	1798.022	1799.006
287.135	269.124	270.108	A	1687.974	1669.964	1670.948
386.203	368.193	369.177	V	1616.937	1598.926	1599.91
533.272	515.26	516.245	F	1517.869	1499.858	1500.842
648.299	630.288	631.272	D	1370.8	1352.79	1353.774
1615.869	1597.858	1598.842	E	1255.773	1237.763	1238.747
1728.953	1710.942	1711.927	I	**288.203**	270.192	271.176
			R	**175.119**	157.108	158.092
Charge: +2						
b	**b-H2O**	**b-NH3**	**AA**	**y**	**y-H2O**	**y-NH3**
44.523	35.518	36.01	S			
108.553	99.547	100.039	Q	908.52	899.515	900.007
144.071	135.066	135.558	A	**844.491**	835.485	835.977
193.605	184.6	185.092	V	**808.972**	799.967	800.459
267.14	258.134	258.625	F	**759.438**	750.433	750.925
324.653	315.648	316.14	D	**685.904**	676.898	677.39
808.438	799.433	799.925	E	**628.39**	619.385	619.877
864.98	855.975	856.467	I	144.605	135.6	136.092
			R	88.063	79.058	79.55
Charge: +3						
b	**b-H2O**	**b-NH3**	**AA**	**y**	**y-H2O**	**y-NH3**
30.018	24.014	24.342	S			
72.704	66.701	67.029	Q	606.016	600.012	600.34
96.383	90.38	90.708	A	563.33	557.326	557.654
129.406	123.402	123.73	V	539.651	533.647	533.975
178.429	172.425	172.753	F	506.628	500.624	500.952
216.771	210.768	211.096	D	457.605	451.601	451.929
539.295	533.291	533.619	E	419.263	413.259	413.587
576.989	570.986	571.314	I	96.739	90.736	91.064
			R	59.045	53.041	53.369
Peptide: β	**ELGKAIVK**					
Charge: +1						
b	**b-H2O**	**b-NH3**	**AA**	**y**	**y-H2O**	**y-NH3**
130.05	112.039	113.023	E			
243.134	225.123	226.107	L	1774.022	1756.012	1756.996
300.155	282.145	283.129	G	1660.938	1642.928	1643.912
1473.77	1455.759	1456.743	K	1603.917	1585.906	1586.89
1544.807	1526.796	1527.78	A	**430.302**	412.292	413.276
1657.891	1639.88	1640.864	I	**359.265**	341.255	342.239
1756.959	1738.949	1739.933	V	**246.181**	228.171	229.155
			K	**147.113**	129.102	130.086
Charge: +2						
b	**b-H2O**	**b-NH3**	**AA**	**y**	**y-H2O**	**y-NH3**
65.529	56.523	57.015	E			
122.071	113.065	113.557	L	887.515	878.509	879.001

150.581	141.576	142.068	G	**830.973**	821.967	822.459
737.388	728.383	728.875	K	802.462	793.457	793.949
772.907	763.902	764.394	A	215.655	206.65	207.142
829.449	820.444	820.936	I	180.136	171.131	171.623
878.983	869.978	870.47	V	123.594	114.589	115.081
			K	74.06	65.055	65.547
Charge: +3						
b	**b-H2O**	**b-NH3**	**AA**	**y**	**y-H2O**	**y-NH3**
44.021	38.018	38.346	E			
81.716	75.713	76.041	L	592.012	586.009	586.337
100.723	94.72	95.048	G	554.318	548.314	548.642
491.928	485.925	486.253	K	535.31	529.307	529.635
515.607	509.604	509.932	A	144.106	138.102	138.43
553.302	547.298	547.626	I	120.427	114.423	114.751
586.325	580.321	580.649	V	82.732	76.728	77.056

Peptide: α	**SQAVFDEIR**		
Charge: +1			
a	**a-H2O**	**a-NH3**	**AA**
60.044	42.034	43.018	S
188.103	170.092	171.076	Q
259.14	241.13	242.114	A
358.208	340.198	341.182	V
505.277	487.266	488.25	F
620.304	602.293	603.277	D
1587.874	1569.864	1570.848	E
1700.958	1682.948	1683.932	I
			R
Charge: +2			
a	**a-H2O**	**a-NH3**	**AA**
30.526	21.521	22.013	S
94.555	85.55	86.042	Q
130.074	121.068	121.56	A
179.608	170.603	171.095	V
253.142	244.137	244.629	F
310.656	301.65	302.142	D
794.441	785.435	785.927	E
850.983	841.977	842.469	I
			R
Charge: +3			
a	**a-H2O**	**a-NH3**	**AA**
20.686	14.683	15.011	S
63.373	57.369	57.697	Q
87.052	81.048	81.376	A
120.074	114.071	114.399	V
169.097	163.094	163.422	F
207.439	201.436	201.764	D
529.963	523.958	524.287	E
567.658	561.654	561.982	I
			R
Peptide: β	**ELGKAIVK**		
Charge: +1			
a	**a-H2O**	**a-NH3**	**AA**
102.055	84.044	85.028	E
215.139	197.128	198.112	L
272.16	254.15	255.134	G
1445.775	1427.764	1428.748	K
1516.812	1498.801	1499.785	A
1629.896	1611.885	1612.869	I
1728.964	1710.954	1711.938	V
			K
Charge: +2			
a	**a-H2O**	**a-NH3**	**AA**
51.531	42.526	43.018	E
108.073	99.068	99.56	L

136.584	127.579	128.071	G
723.391	714.386	714.878	K
758.91	749.904	750.396	A
815.452	806.446	806.938	I
864.986	855.981	856.473	V
			K
Charge: +3			
a	**a-H2O**	**a-NH3**	**AA**
34.69	28.686	29.014	E
72.385	66.381	66.709	L
91.392	85.388	85.716	G
482.596	476.593	476.921	K
506.275	500.272	500.6	A
543.97	537.967	538.295	I
576.993	570.989	571.317	V
			K

Site A	Site B	Seq A	Start A	Stop A	Seq B	Start B
Y-545	K-579	PEVLYSGYDST	541	558	LGGRQVVSAV	566
	Y-738	PEVLYSGYDST	541	558	MVGGLLQFCF	728
S-546	K-579	PEVLYSGYDST	541	558	LGGRQVVSAV	566
K-576	K-579	QVVSAVKWAI	570	579	WAKALPGFR	577
	K-695	QVVSAVKWAI	570	579	MTYIKELGK	691
K-579	K-614	WAKALPGFR	577	585	SYKQSNGNMI	612
	K-677	WAKALPGFR	577	585	VLLLLSTVPKD(	668
	K-681	WAKALPGFR	577	585	DGLKSQAVFD	678
	K-695	WAKALPGFR	577	585	MTYIKELGK	691
	K-703	WAKALPGFR	577	585	AIVKR	700
	K-770	WAKALPGFR	577	585	AGSVKPLLFH(	766
	K-777	WAKALPGFR	577	585	PLLFHQK	771
K-614	K-703	SYKQSNGNMI	612	633	AIVKR	700
S-659	K-667	LQVSYDEYLCN	656	677	LQVSYDEYLCN	656
K-677	K-695	VLLLLSTVPKD(	668	681	MTYIKELGK	691
	K-765	VLLLLSTVPKD(	668	681	FKAGSVK	764
					FKAGSVKPLLF	764
	K-770	VLLLLSTVPKD	668	678	AGSVKPLLFH(	766
		VLLLLSTVPKD(	668	681	AGSVKPLLFH(	766
	K-777	VLLLLSTVPKD	668	678	PLLFHQK	771
		VLLLLSTVPKD(	668	681	AGSVKPLLFH(	766
					PLLFHQK	771
K-681	K-763	DGLKSQAVFD	678	690	SLSVEFPEMLA	744
K-695	K-695	MTYIKELGK	691	699	MTYIKELGK	691
	K-699	MTYIKELGK	691	699	ELGKAIVK	696
	S-708	MTYIKELGK	691	699	EGNSSQNWQ	705
	S-709	MTYIKELGK	691	699	EGNSSQNWQ	705
	T-719	MTYIKELGK	691	699	FYQLTK	715
	K-765	MTYIKELGK	691	699	FKAGSVK	764
					FKAGSVKPLLF	764
	K-770	MTYIKELGK	691	699	AGSVKPLLFH(	766
	K-777	MTYIKELGK	691	699	AGSVKPLLFH(	766
					PLLFHQK	771
K-699	K-765	ELGKAIVK	696	703	FKAGSVK	764
	K-770	ELGKAIVK	696	703	AGSVKPLLFH(	766
	K-777	ELGKAIVK	696	703	PLLFHQK	771
K-703	K-765	AIVKR	700	704	FKAGSVK	764
	K-770	AIVKR	700	704	AGSVKPLLFH(	766
	K-777	AIVKR	700	704	AGSVKPLLFH(	766
					PLLFHQK	771
S-709	K-777	EGNSSQNWQ	705	714	PLLFHQK	771
T-719	K-777	FYQLTK	715	720	PLLFHQK	771
K-720	K-777	FYQLTKLLD	715	723	PLLFHQK	771
S-744	K-770	SLSVEFPEMLA	744	763	AGSVKPLLFH(	766
K-765	K-765	FKAGSVK	764	770	FKAGSVK	764
	K-770	FKAGSVK	764	770	AGSVKPLLFH(	766
K-777	K-777	PLLFHQK	771	777	PLLFHQK	771

*Intramolecular distances were calculated by mapping the residues in PDB=5UFS.

Stop B	Intramolecular Distance*
585	26,6 Å
748	33,9 Å
585	25,1 Å
585	11,5 Å
699	30,3 Å
633	30,9 Å
681	30,8 Å
690	18,9 Å
699	26,3 Å
704	29,2 Å
777	27,2 Å
777	36,6 Å
704	10,5 Å
677	13,0 Å
699	31,1 Å
770	18,4 Å
777	18,4 Å
777	8,9 Å
777	8,9 Å
777	12,4 Å
777	12,4 Å
777	12,4 Å
765	10,7 Å
699	0 Å
703	5,4 Å
714	17,9 Å
714	18,6 Å
720	15,8 Å
770	39,3 Å
777	39,3 Å
777	22,9 Å
777	25,2 Å
777	25,2 Å
770	40,7 Å
777	26,4 Å
777	29,8 Å
770	37,9 Å
777	29,8 Å
777	29,4 Å
777	29,4 Å
777	28,4 Å
777	15,8 Å
777	11,0 Å
777	40,6 Å
770	0 Å
777	20,8 Å
777	0 Å

Peptide: β	**VLCSGYDSTLPDTSTR**					
Peptide: α	**VLCSGYDSTLPDTSTR**					
Charge: +1						
b	**b-H2O**	**b-NH3**	**AA**	**y**	**y-H2O**	**y-NH3**
100.076	82.065	83.049	V			
213.16	195.149	196.133	L	3327.499	3309.489	3310.473
2027.941	2009.931	2010.915	C	3214.415	3196.405	3197.389
2114.973	2096.963	2097.947	S	**1399.634**	1381.623	1382.607
2171.995	2153.984	2154.968	G	**1312.602**	1294.591	1295.575
2335.058	2317.048	2318.032	Y	**1255.58**	1237.57	1238.554
2450.085	2432.074	2433.058	D	**1092.517**	1074.506	1075.49
2537.117	2519.106	2520.09	S	**977.49**	959.479	960.463
2638.165	2620.154	2621.138	T	**890.458**	872.447	873.431
2751.249	2733.238	2734.222	L	**789.41**	771.4	772.384
2848.302	2830.291	2831.275	P	**676.326**	658.315	659.299
2963.328	2945.318	2946.302	D	**579.273**	561.263	562.247
3064.376	3046.366	3047.35	T	**464.246**	446.236	447.22
3151.408	3133.398	3134.382	S	**363.199**	345.188	346.172
3252.456	3234.445	3235.429	T	**276.167**	258.156	259.14
			R	**175.119**	157.108	158.092
Charge: +2						
b	**b-H2O**	**b-NH3**	**AA**	**y**	**y-H2O**	**y-NH3**
50.541	41.536	42.028	V			
107.084	98.078	98.57	L	1664.253	1655.248	1655.74
1014.474	1005.469	1005.961	C	1607.711	1598.706	1599.198
1057.99	1048.985	1049.477	S	700.32	691.315	691.807
1086.501	1077.496	1077.988	G	656.804	647.799	648.291
1168.033	1159.027	1159.519	Y	628.294	619.288	619.78
1225.546	1216.541	1217.033	D	546.762	537.757	538.249
1269.062	1260.057	1260.549	S	489.249	480.243	480.735
1319.586	1310.581	1311.073	T	445.733	436.727	437.219
1376.128	1367.123	1367.615	L	395.209	386.203	386.695
1424.654	1415.649	1416.141	P	338.667	329.661	330.153
1482.168	1473.163	1473.655	D	290.14	281.135	281.627
1532.692	1523.686	1524.178	T	232.627	223.622	224.114
1576.208	1567.202	1567.694	S	182.103	173.098	173.59
1626.732	1617.726	1618.218	T	138.587	129.582	130.074
			R	88.063	79.058	79.55
Charge: +3						
b	**b-H2O**	**b-NH3**	**AA**	**y**	**y-H2O**	**y-NH3**
34.03	28.027	28.355	V			
71.725	65.721	66.049	L	1109.838	1103.834	1104.162
676.652	670.648	670.976	C	1072.143	1066.14	1066.468
705.663	699.659	699.987	S	467.216	461.213	461.541
724.67	718.666	718.994	G	438.205	432.202	432.53

779.024	773.021	773.349	Y	419.198	413.195	413.523
817.367	811.363	811.691	D	364.844	358.84	359.168
846.377	840.374	840.702	S	326.501	320.498	320.826
880.06	874.056	874.384	T	297.491	291.487	291.815
917.754	911.751	912.079	L	263.808	257.805	258.133
950.105	944.102	944.43	P	226.114	220.11	220.438
988.448	982.444	982.772	D	193.763	187.759	188.087
1022.13	1016.127	1016.455	T	155.42	149.417	149.745
1051.141	1045.137	1045.465	S	121.738	115.734	116.062
1084.823	1078.82	1079.148	T	92.727	86.724	87.052

Peptide: β	**VLCSGYDSTLPDTSTR**		
Peptide: α	**VLCSGYDSTLPDTSTR**		
Charge: +1			
a	**a-H2O**	**a-NH3**	**AA**
72.081	54.07	55.054	V
185.165	167.154	168.138	L
1999.946	1981.936	1982.92	C
2086.978	2068.968	2069.952	S
2144	2125.989	2126.973	G
2307.063	2289.053	2290.037	Y
2422.09	2404.08	2405.064	D
2509.122	2491.112	2492.096	S
2610.17	2592.159	2593.143	T
2723.254	2705.243	2706.227	L
2820.307	2802.296	2803.28	P
2935.334	2917.323	2918.307	D
3036.381	3018.371	3019.355	T
3123.413	3105.403	3106.387	S
3224.461	3206.45	3207.434	T
			R
Charge: +2			
a	**a-H2O**	**a-NH3**	**AA**
36.544	27.539	28.031	V
93.086	84.081	84.573	L
1000.477	991.472	991.964	C
1043.993	1034.988	1035.48	S
1072.504	1063.498	1063.99	
1154.035	1145.03	1145.522	
1211.549	1202.543	1203.035	
1255.065	1246.059	1246.551	
1305.589	1296.583	1297.075	
1362.131	1353.125	1353.617	
1410.657	1401.652	1402.144	
1468.17	1459.165	1459.657	
1518.694	1509.689	1510.181	
1562.21	1553.205	1553.697	
1612.734	1603.729	1604.221	
Charge: +3			
a	**a-H2O**	**a-NH3**	
24.698	18.695	19.023	
62.393	56.39	56.718	
667.32	661.317	661.645	
696.331	690.327	690.655	
715.338	709.335	709.663	

769.693	763.689	764.017	
808.035	802.031	802.359	
837.046	831.042	831.37	
870.728	864.725	865.053	
908.423	902.419	902.747	
940.774	934.77	935.098	
979.116	973.113	973.441	
1012.799	1006.795	1007.123	
1041.809	1035.806	1036.134	
1075.492	1069.488	1069.816	